DESIGN OF A PERMANENT MAGNET BRUSHLESS DC MOTOR FOR THE ELECTRIC THREE-WHEELER IN BANGLADESH

by

Md. Junaed-Al-Hossain
(0419062108)

Submitted in partial fulfillment of the requirements of the degree of
Master of Science in Electrical and Electronic Engineering

Under the supervision of

Dr. Md. Ziaur Rahman Khan
Professor
Department of Electrical and Electronic Engineering
Bangladesh University of Engineering and Technology (BUET)

BANGLADESH UNIVERSITY OF ENGINEERING AND TECHNOLOGY
DHAKA-1000, BANGLADESH
July 2023

Certification of Thesis

The thesis titled "DESIGN OF A PERMANENT MAGNET BRUSHLESS DC MOTOR FOR THE ELECTRIC THREE-WHEELER IN BANGLADESH" submitted by Md. Junaed-Al-Hossain, Roll No.: 0419062108, Session: April-2019, has been accepted as satisfactory in partial fulfillment of the requirement for the degree of Master of Science (M.Sc.) in Electrical and Electronic Engineering on 11 July 2023.

BOARD OF EXAMINERS

Dr. Md. Ziaur Rahman Khan Professor EEE, BUET, Dhaka	Chairman (Supervisor)
Dr. Md. Aynal Haque Professor & Head EEE, BUET, Dhaka	Member (Ex-Officio)
Dr. Mohammad Jahangir Alam Professor EEE, BUET, Dhaka	Member
Dr. Muhammad Abdullah Arafat Assistant Professor EEE, BUET, Dhaka	Member
Dr. Enamul Basher Professor Department of EEE, University of Asia Pacific, Dhaka	Member (External)

Candidate's Declaration

I, Md. Junaed-Al-Hossain, declare that this thesis titled, "DESIGN OF A PERMANENT MAGNET BRUSHLESS DC MOTOR FOR THE ELECTRIC THREE-WHEELER IN BANGLADESH" and the work presented in it are fully my own in partial fulfillment of the requirement for the degree of Master of Science (M.Sc.) in Electrical and Electronic Engineering. I confirm that this research work has not been submitted elsewhere for the award of any degree or diploma excepting for publication. Others' works that have been quoted are clearly attributed with source.

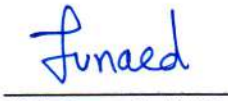

Md. Junaed-Al-Hossain

Acknowledgement

I am grateful to Almighty ALLAH for enabling me to complete this work.

I would like to express my deepest gratitude to my supervisor, Dr. Ziaur Rahman Khan, Professor, Department of Electrical and Electronic Engineering, Bangladesh University of Engineering and Technology (BUET), Dhaka, for his kind supervision and valuable advice. His guidance, patience, and assistance were essential to the completion of this work.

I would like to express my utmost gratitude to my parents for their love and support throughout my academic journey. Their faith in my capability to withstand the challenges gave me immense strength to undertake the arduous research work. I would like to thank the technical personnel from different laboratories of BUET for their contribution to the software model and hardware development. I would also like to thank all my well-wishers for their support throughout my journey to complete this work.

Abstract

The design of a 1 KW PM BLDC motor for compact-sized electric three-wheelers (C-E3Ws) has been presented here. The C-E3Ws primarily operate in the cities, especially Dhaka, and they are more suitable for congested city roads than other E3W variants. Few works have been reported on the design of PM-BLDC motors for E3Ws. However, none of them addressed the BLDC motor's performance in C-E3Ws. This work addresses this research gap. Three real-time driving profiles of C-E3Ws have been recorded from three different areas of Dhaka City. These driving profiles have been analyzed to determine the prospective motor peak torque, rated speed, and continuous torque region for the motor design. The primary motor design goals have been set based on motor efficiency, speed, and torque. A mathematical equation-based analytical sizing model has been developed for the motor design. Practically measurable parameters are chosen from a commercial C-E3W motor, and others are selected for effective design consideration. A 2-D finite element (FE) based electromagnetic model of the PM-BLDC motor has been developed in Ansys Maxwell with the values obtained from the analytical sizing model, which is optimized to achieve the design goals. The magnet dimensions and motor stack length are considered as the optimized design variables. From FE analysis, motor torque and different types of losses are determined. The results show that the designed motor has achieved the design targets. A lumped parameter-based thermal model has been developed in Ansys Motor-CAD to evaluate the motor's thermal performance over the recorded driving profiles and the motor's continuous operation region. The necessary parameters are appropriately calibrated for the thermal analysis. The performance of a commercial C-E3W motor is evaluated with experimental set-up and compared with the designed BLDC motor. The designed PM-BLDC motor displays better performance in terms of efficiency and power factor than its commercial counterpart.

Table of Contents

List of Figures

List of Tables

List of Abbreviations

2-D	Two Dimensional
3-D	Three Dimensional
BLDC	Brushless Direct Current
C-E3W	Compact Electric Three Wheeler
CFD	Computational Fluid Dynamics
DC	Direct Current
E3W	Electric Three Wheeler
EMF	Electro-motive Force
EV	Electric Vehicle
FEA	Finite Element Analysis
FEM	Finite Element Method
FFT	Fast Fourier Transform
GDF	Global Degrees of Freedom
HEV	Hybrid Electric Vehicle
LP	Lumped Parameter
MMF	Magneto-motive Force
RPM	Revolution Per Minute
PM	Permanent Magnet
PM-BLDC	Permanent Magnet Brushless Direct Current
PMSM	Permanent Magnet Synchronous Motor
TEFC	Totally Enclosed Fan Cooled

List of Symbols

Variable	Parameter
ω_m	Motor speed
G_r	C-E3W gear ratio
V	C-E3W velocity
r	C-E3W tire radius
T_{rated}	Motor rated torque
P_{rated}	Motor rated power
ω_{rated}	Motor rated speed
F_{rr}	Rolling resistance force
F_{Ad}	Aerodynamic drag force
F_G	Gradient force
F_{Ac}	Acceleration force
m	Total vehicle mass including payload
g	Gravitational acceleration
θ	Gradient angle of the driving path
μ_r	Rolling resistance coefficient
C_D	Drag co-efficient
A_f	Frontal are
ρ	Air density
V_A	Air velocity
l	Vehicle length

Variable	Parameter
w	Vehicle width
h	Vehicle height
g_c	Ground clearance
a	Vehicle acceleration
F_{trac}	Total traction force
T_{trac}	Total traction torque
T_{motor}	Motor Torque
N_s	Number of slots
N_p	Number of poles
N_{tc}	Number of turns per coil
D_r	Rotor diameter
D_{sh}	Shaft diameter
V_{dc}	DC Voltage
P_{in_system}	Input power of motor-inverter system
P_{out_motor}	Motor output power
η_{motor}	Motor efficiency
$\eta_{inverter}$	Inverter efficiency
I_{dc}	DC link current
I_{ph}	Phase current peak value
I_{ph_rms}	Phase current rms value
ar	Aspect ratio
L_{stack}	Motor stack length

Variable	Parameter
V_{rotor}	Rotor Volume
TRV	Torque per rotor volume
B	Magnetic loading
A	Electrical loading
k_{w1}	Fundamental winding factor
N_{tph}	Number of turns per phase
N_{spph}	Number of slots per phase
N_{tc}	Number of turns per coil
N_p	Number of parallel paths
$\emptyset_t$	Total flux
$\emptyset_s$	Flux flowing through each tooth
$\emptyset_p$	Flux under one pole
B_1	Fundamental flux density
$\emptyset_1$	Fundamental pole flux
J_{rms}	RMS current density
$N_{strands}$	Number of strands
$cAsc$	Copper area of a single coil
$cAss$	Copper area of a single strand
k_f	Bare slot fill factor
A_{slot}	Approximate slot area
B_{st}	Maximum stator tooth flux density
B_{sy}	Stator yoke flux density

Variable	Parameter
W_{st}	Stator tooth width
W_{sy}	Stator yoke width
k_{st}	Stacking factor
b_{s0}	Slot opening width
h_{s0}	Slot opening height
h_{s1}	Height of tooth shoe
bs_1	Slot width at the bottom
bs_2	Slot width at the top
hs_1	Slot height tip to bottom
hs_2	Slot height bottom to tip
D	Stator inner diameter
a_g	Air gap
OSD	Stator outside diameter
SR	Motor split ratio
dm	Magnet thickness
P_c	Permeance coefficient
$C_{\emptyset}$	Flux concentration factor
K_l	Leakage factor
K_r	Reluctance factor
B_r	Remanence flux density
r_{ph}	Phase resistance
L_{end}	End inductance

Variable	Parameter
L_{xn}	Winding extension
τ_{cp}	Coil pitch
L_{mt}	Total length of a single turn
r_c	Resistance of a single coil
r_{ph}	Phase resistance
ρ	Resistivity of the conductor
N_{spph}	Number of slots per phase
k_{ar}	AC resistance factor
μ_o	Air permeability
P_{cu}	Copper loss
P_{core}	Core loss
P_{mag}	Magnet loss
P_{mec}	Mechanical loss
$\emptyset_{g_{FE}}$	Air gap flux
$\emptyset_{pm_{FE}}$	Permanent magnet flux
$MMF_{g_{FE}}$	Air gap MMF
$MMF_{pm_{FE}}$	Permanent magnet MMF
$CPRM$	Cycles per mechanical revolution
LCM	Least Common Multiplier
N_p	Number of poles
N_s	Number of slots
P_{em}	Electromagnetic power

Variable	Parameter
ω_m	Motor speed in rad/sec
T_{em}	Electromagnetic Torque
P_{out}	Motor output power
P_{core}	Core loss
P_{mag}	Magnet loss
P_{mech}	Mechanical loss
P_{cu}	Copper Loss
I_a	Phase A current
I_b	Phase B current
I_c	Phase C current
P_{in}	Motor input power
PF	Power Factor
V_{rms}	Phase voltage rms value
I_{rms}	Phase current rms value
L_s	Self-inductance
L_m	Mutual-inductance
L_d	d-axis inductance
L_q	q-axis inductance
T_{motor}	Commercial Motor Torque
m_l	Recorded load mass
l_a	Arm length
r	Load motor radius

Chapter 1: Introduction

1.1 Background

Presently, electric three-wheelers are the only mode of electric mobility in Bangladesh. Besides Bangladesh, the E3Ws are also seen in many countries, including India, Nepal, Thailand, China, Indonesia, Tanzania, Philippines, etc.[1-4]. Bangladesh is estimated to have over one million E3Ws[5]. There are two types of electric three-wheelers. One is a comparatively larger sized E3W, known as Easy bike, which can carry 6-8 people. The easy bikes are primarily seen in sub-urban and village areas. Another type of E3W is the compact-sized electric three-wheeler (C-E3W) known as Mishuk. The C-E3W can carry 3-4 people at a time. Due to its compact size and frequency of mobility, the C-E3W is the most suitable for city areas; therefore, they are primarily available in city areas. Figure 1.1 shows the two types of E3Ws seen in Bangladesh[5].

(a) (b)

Figure 1.1: Electric three-wheelers: (a) Easy Bike (b) Mishuk

The traction motor is the source of propulsion for the E3Ws. Motors of different types are used in electric vehicles, such as induction motors, permanent magnet synchronous motors, permanent magnet brushless DC motors (PM-BLDC), switched reluctance motors, etc.[6, 7]. Among them, the PM-BLDC motor is the most used traction motor for the E3Ws. The BLDC motor has higher availability, reasonable cost, high power density, efficiency, and ease of control[2, 6]. Such characteristics provide BLDC motors an edge over other types of motors. The application of BLDC motors covers different types of vehicles, such as electric cars, scooters, bikes, and E3Ws [8-12].

The vehicle's real-time driving profile or drive cycle (DC) is a valuable tool to assess a vehicle's performance and requirements of its drive train components [13, 14]. The driving profile can differ depending on the vehicle configuration, type, and driving region. For designing a traction motor, the vehicle drive cycles should be considered so that the motor can operate in maximum torque and efficiency regions while being within thermal limits. By doing so, energy waste can be reduced, and the driving range or fuel economy can be increased [15]. Therefore, the characteristics of a driving profile can aid in the optimal design of a traction motor [15, 16]. Although there are some established drive cycles, both standard and tailored to assess electric vehicle performance [13, 14, 17], there have not been any such drive cycles that adequately address or resemble the driving profiles of the E3Ws that operate in Bangladesh.

The BLDC motor works on the principle of electromagnetism, where the rotor's and stator's magnetic fields interact with each other to create torque. The windings of the stator are energized in a specific sequence, creating a rotating magnetic field. It interacts with the permanent magnet rotor, and as a result, motion is produced [18]. Overall, the electromagnetic characteristics of a BLDC motor play a significant role in determining its performance and efficiency. By carefully selecting the appropriate motor design, it is possible to achieve the desired performance for an E3W. Moreover, the motor must produce the required power and torque for C-E3W propulsion while operating within its thermal limits. Overheating of the motor can cause winding insulation failure [19] and demagnetization of the permanent magnets [20].

1.2 Motivation

The electric three-wheelers provide a pollution-free and noiseless operation, contributing to its growing popularity nationwide. The compact-sized electric three-wheelers can contribute significantly in this regard in congested city roads. Since the most used PM-BLDC motor is the only source of propulsion of the C-E3Ws, the vehicle's performance can be significantly enhanced with the highly efficient performance of the BLDC motor. The traction motor’s performance should be examined throughout the vehicle’s driving profiles to better characterize its requirements. Therefore, the characteristics of the driving profiles can aid in the optimal design of a traction motor. Electromagnetic modeling of the BLDC motor can

provide significant insight into the motor performance and enable effective design for an efficient motor. Since the motor's performance depends greatly on its thermal characteristics, it is imperative to ensure it can operate without exceeding its thermal limit. Over thermal limits, the motor can incur significant damage, which can further contribute to motor failure during vehicle propulsion. Since the PM-BLDC motors are not produced locally but imported from abroad, the requirement of the motors from Bangladeshi prospects may not be appropriately addressed. An in-depth design methodology should be adopted to facilitate C-E3W integration into city public transportation, considering the C-E3W typical driving profiles, electromagnetic, and thermal performance. There has yet to be any research considering all these aspects for designing a traction motor for the C-E3Ws in Bangladesh prospects. The thesis aims to close the research gap and provide insight into the PM-BLDC motor performance from electromagnetic and thermal perspectives for the C-E3Ws in Bangladesh.

1.3 Objectives

The specific objectives of this work are as follows:

i. To analyze driving profiles of a C-E3W vehicle.
ii. To develop an analytical motor sizing model with appropriate design parameters.
iii. To design a finite element-based electromagnetic model of a PM-BLDC motor for C-E3Ws in Bangladesh.
iv. To perform thermal analysis of the motor to determine motor component temperature over the continuous motor operation.
v. To compare the designed motor performances with the existing commercial motor for C-E3W vehicles.

1.4 Thesis Organization

This thesis consists of five chapters. The structure of the thesis is as follows.

- In Chapter 1, the brief background of the thesis work is presented with a particular focus on the electric three-wheelers and the traction permanent magnet BLDC motor. Then, the motivation for the current work and the objectives are presented.
- In Chapter 2, a thorough review of the works relevant to the thesis is presented. Later on, the research gaps are identified.
- In Chapter 3, three recorded driving profiles of C-E3Ws are presented. The driving profiles have been analyzed to calculate motor torque and speed over the driving profiles. Standard C-E3W parameters, such as dimensions, weight, gear ratio, etc., are considered for calculating motor torque. The motor torque and speed values have been analyzed to determine the motor base speed, base torque, peak torque, and continuous torque.
- In Chapter 4, an analytical sizing model has been developed for the PM-BLDC motor of C-E3W with the motor sizing equations. Motor design goals have been set based on efficiency, torque, and speed. Some parameters have been selected based on the commercially available C-E3W BLDC motor, and other parameters are either selected based on published literature or design considerations.
- In Chapter 5, A two-dimensional finite element-based parametric model of the BLDC motor has been developed with the parameters calculated from analytical machine sizing equations. A circuit model has been developed to excite the motor windings with currents. Geometrical parameters have been optimized to meet torque, speed, and efficiency goals. From the 2D finite element simulation, motor torque-speed characteristics and efficiency map has been developed.
- In Chapter 6, a thermal lumped parameter model has been developed to determine the temperature of different motor components over the continuous operating torque range and the recorded driving profiles. The motor cooling system has been designed with appropriate motor housing dimensions.
- In Chapter 7, the experimental setup is presented to determine the base torque and speed of a commercial 1 KW C-E3W PM-BLDC motor, and its rated efficiency and power factor have been determined.
- Finally, in chapter 8, the summary of the key findings is presented, followed by the possibilities of future research work.

Chapter 2: Literature Review

In this chapter, various researches regarding PM-BLDC motor design for C-E3W have been reviewed. The review of the relevant research work provides insights on the research scope and lays foundation for the new research.

2.1 Electric Three Wheeler

The E3W is a form of electric vehicle generally used for public transportation for short trips. These vehicles have different acceleration characteristics compared to cars, as suggested in [21]. The E3Ws are battery-operated vehicles whose battery voltages are either 60 Volts or 48 Volts, depending on the variants of the E3Ws. The battery provides the necessary power for the traction motor to operate. Different issues regarding E3Ws and their corresponding solutions are presented in [5]. Authors in [6] have discussed the selection criterion for motors and batteries for E3Ws. The major components of an E3W drivetrain are a battery, traction motor, motor controllers, and differential, as shown in Figure 2.1.

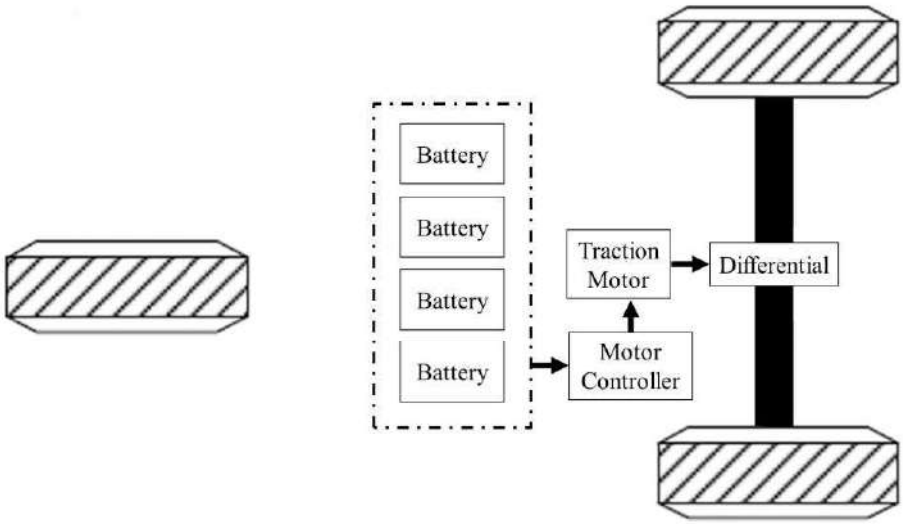

Figure 2.1: An E3W drivetrain components

The E3W batteries are generally charged with off-board chargers, and they consume a significant amount of power from the national grid, as presented in [22] in light of Bangladesh. Demand management can be employed to facilitate the grid to sustain the charging load, as discussed in [23]. Incorporating renewable energy to facilitate the

charging infrastructure has been discussed in [24]. Authors in [25] developed an advanced E3W model with a solar panel attached to its ceiling. Authors in [26] have presented an analysis of the traction motor in an E3W and a comparison with the engines of conventional three-wheelers. The E3W vehicle structural analysis has been performed in [27].

2.2 Electric Motor Design

The permanent magnet brushless DC motor is used for various applications including, automotive and machinery. Design and analysis of an axial flux PM BLDC motor for an electric scooter have been proposed in [8]. The motor sizing has been performed using a small number of variables, and justification for required motor power, torque, and speed has not been presented in this work. BLDC motor design study for an electric bicycle is presented in [28]. The motor power and speed requirement have been determined by EN 15194 European Standard. Different combinations slot-pole combinations and winding configurations are analyzed to design the electric motor. A prototype motor has been manufactured and compared with a commercial electric bicycle BLDC motor. Finite Element modeling and analysis of a 3-phase BLDC motor for an electric bicycle is proposed in [29], where the emphasis has been given to direct-drive applications with low speed and high torque capability. Three motor designs and their electromagnetic characteristics and performances have been considered, including cogging torque, back-EMF, torque output, torque ripples, inductances, iron saturation level, and magnet demagnetization. The research work in [30] presents the design and analysis of an in-Wheel Motor for an Electric Vehicle with four independent wheel drives. The motor performance requirement has been determined using traction load equations, followed by motor sizing equations to motor structural parameters. Later a 2-D FE model of the motor was developed. The design of a 3-phase double-layer coil BLDC motor for Hybrid (HEV) and Electric Vehicles (EV) has been presented in [31]. In this work, two 15 kW BLDC motor configurations have been developed with different slot and pole combinations and compared in terms of motor torque. Analytical design and finite element analysis based simulation and analysis of three-phase BLDC motor for automotive application are presented in [32]. The finite element method (FEM) is used to determine the performance characteristics

of a PM-BLDC motor for solar and hybrid electric vehicles and is presented in [33]. The work has concluded that increasing the lead angle in the control circuit increases the motor's rated speed, and higher efficiency is achieved at the cost of a decrease in rated torque and an increase in ripple in torque. Analysis and design of a PM-BLDC motor for three-wheelers have been proposed in [12]. The designed motor is rated at 1.5 kW, 3000 rpm, 120 V radial flux surface mounted permanent magnet rotor. Such higher voltage is not used in the E3Ws in Bangladesh. Moreover, this work has not assessed the detail loss analysis and thermal stability of the motor. The works in [34] have a FE modeling of a three-phase PMSM for E3Ws. Sizing with vehicle dynamics, analytical design, and virtual development of the motor is also included. However, in vehicle dynamics, any standard or tailored driving profile has yet to be considered, and during the calculation of E3W traction load, passenger weight has not been included. Moreover, the motor required power, voltage, and speed do not match with the E3W vehicles being used in Bangladesh. Detailed design procedures for a three-phase surface-mounted PM-BLDC motor have been presented in [35]. The designed motor has been compared with a three-phase induction motor of the same power rating. However, the motor application has not been specified in this work.

A comparative analysis of a surface-mounted permanent magnet (SPM) and an interior permanent magnet (IPM) PM-BLDC motor of an identical pole, power rating, and motor speed have been presented in [36]. The work has concluded that the IPM motor displays better than SPM in applications where torque ripple is a minimal concern. A thorough design procedure of a three-phase exterior rotor PM-BLDC motor for a ceiling fan is presented in [37]. This work presents a detailed analytical design procedure, including the initial sizing, stator, rotor design, and performance assessment.

2.3 Motor Design Parameter Study

The work in [38] presents the guidelines for designing concentrated winding fractional slot permanent magnet machines. The winding factor and slot-pole combinations are studied for different motors with identical frame sizes and air gaps. A simplified procedure for analytical machine sizing for a three-phase surface-mounted permanent magnet synchronous machine for system-level analysis and preliminary machine

design has been proposed in [39]. Besides being computationally efficient, analytical machine sizing can quickly generate numerous candidate designs, which can be refined further with computationally intensive methods like finite element analysis (FEA). An analysis of BLDC motors of four types of slots with identical slot areas has been presented in [40]. Performance parameters, including motor efficiency, electromagnetic torque, output power, and flux density, are analyzed for the motor models. A voltage equation-based procedure for electrical parameter measurement of permanent magnet synchronous motor (PMSM) is presented in [41]. The procedure considers all losses such as copper, iron, mechanical, and stray losses. An analysis of a PM-BLDC motor with a fixed outer diameter and active zone length is presented in [42]. This work analyzes the influence of the air gap, permanent magnet's material, and size on the machine's magnetic flux and flux density. However, the analysis has been performed based on the theory of synchronous machines, which may ignore the distinctive features of BLDC compared to PMSM. The development of a PM-BLDC motor for driving a high-speed embroidery machine is presented in [43]. In this work, finite-element analysis is performed to determine the key motor parameters like the air gap flux, back EMF, and inductance, and the motor's steady-state characteristics are computed with a phasor diagram. A 3-D finite element model is developed in [44] to analyze the vibration characteristics of a BLDC motor. Here the electromagnetic structural weak coupled analysis is performed for the electromagnetic force-induced transient phenomenon, and fast Fourier transformation is used to calculate the frequency response characteristics.

A power management strategy utilized for E3W has been presented in [45]. The power management strategy utilizes an ultra-Capacitor, an additional source that reduces the battery stress. The considered traction motor here is a 3KW PMSM. A procedure to determine the parameters of a BLDC motor electric vehicle is presented in [46]. The dynamic equation of EV and the voltage equation of the BLDC motor were coupled to determine the parameters. The relationship between the vehicle's dynamic parameters and the tractive force requirement is analyzed in [15]. Here an equation-based strategy is adopted to calculate the vehicle's net tractive power and resistive forces. The traction loads supplied by the large-sized E3Ws, known as Easy Bikes, in different drive cycles

in Bangladesh are determined and analyzed in [47]. The underload and the overload operation of the traction over the drive cycles are also presented in this work.

2.4 Motor Performance Improvement

Besides, different research works have presented the design, analysis, and optimization of PM-BLDC motors for various applications. A robust design optimization (RDO) algorithm is presented in [48] for the shape of an electric oil pump's BLDC motor. Here, the design variables were the stator and rotor dimensions. Efficiency improvement and torque performance of a single phase BLDC motor optimum commutation angle at each different speed is presented in [49]. With optimal shift angle, motor efficiency, noise, and vibration characteristics can be improved. The application of steel (M19) material and composite material in the hub BLDC motor is analyzed in [50]. Four different configurations of stator and rotor core materials have been considered in this work. The study concludes that the steel (M19) and soft composite materials (SMC) based stator, and rotor frames display good thermal capability, providing better features in electric vehicles.

Rotor design parameters, such as rotor geometry, magnet placement, and dimensions, have been investigated in [51] to design and optimize a PM-BLDC motor.

The starting torque of a single-phase PM-BLDC motor for both radial and parallel magnetization is investigated in [52]. The work has presented the effectivity of a tapered air gap for a smooth resultant torque waveform. The finite-element analysis of the electromechanical field of a BLDC motor is presented in [53], which has considered speed control and mechanical flexibility such as shaft, rotor, and bearing.

An optimal design of a slotted surface mounted PM-BLDC motor using the theory of inverse problem has been presented in [54]. The main objective was to achieve the optimal magnetic field density, and using the method has resulted in higher air gap magnetic flux density and motor efficiency.

Authors in [55] performed FEA to compute the torque waveforms of a BLDC motor under different current excitations. This work has explored the impact of skewing on torque wave shape. The research in [56] has demonstrated that the cogging torque amplitude and frequency are highly sensitive to magnet dimensions, locations, magnetization patterns, and slot/pole combinations. Studies on various reduction

methods of cogging torque when designing a BLDC motor have been presented in [57]. It is shown that the reduction of slot opening width is more effective in reducing cogging torque than other methods. A novel magnet step-skew approach to reduce the cogging torque and torque pulsations and increase the output torque quality for surface-mounted permanent magnet motors is proposed in [58]. The proposed approach considers variation between the length of the magnet and the angle between the magnet segments, which is different from conventional PM motors, which rely on constant stack length and step-skew angle.

2.5 Thermal Analysis

An accurate prediction of a motor's thermal performance at the design stage is necessary to manufacture motors with smaller sizes and higher efficiency [59]. The thermal design results in significant improvements in overall performance [60]. The temperature rise and heat transfer in an electric machine can be estimated with techniques like Finite Element Methods (FEM), Lumped Parameters (LP), and computational fluid dynamics (CFD)[61]. Among them, the LP circuit network has the advantage over other methods in computation speed [59]. A fast analysis is beneficial in the early design stages. It allows multiple design iterations in an acceptable time. A lumped parameter model-based thermal analysis on a set of five totally enclosed fan cooled motors of different power ratings is presented in [62]. Thermal analysis on a BLDC motor for a primary flight surface actuator has been performed in [63] to verify that the motor can sustain loads for specific times without exceeding insulation limit temperatures. A comprehensive set of convection heat transfer and flow resistance formulations suitable for thermal analysis of electric machines has been presented in [64], providing guidelines for choosing suitable thermal and flow network formulations. Thermal analysis of a totally enclosed fan-cooled (TEFC) squirrel cage three-phase induction motor on three different software platforms have been presented in [65]. In [66], FEA was used to investigate the losses of two identical surface-mounted permanent magnet machines operating as a motor and generator under various PWM duty ratios and supply voltages. The analytical lumped-circuit approach is used to investigate thermal fields. According to the analysis, the magnetomotive force (mmf) time harmonics caused by the non-sinusoidal phase current and PWM

carrier harmonics significantly increase eddy current losses in the motor's magnets and sleeve, leading to noticeable disparities in the temperature increases of the motor and generator. The design and thermal analysis of surface-mounted brushless motors for submersible pump applications have been presented in [67]. A thermal runaway problem is identified, which damages winding insulation. High temperatures across permanent magnets cause demagnetization. This work suggests a wet rotor cooling system for the rotor during steady-state analysis. A steady-state and transient thermal model for an induction machine is presented in [60]. Various manufacturing issues, including interface thermal resistance between stator lamination and housing, axial fin channel air leakage, end winding convection cooling, impregnation goodness, bearing heat transfer, etc., have been predicted by embedding empirical data into the simulation platform. Testing has been performed on a large range of machines to collect the empirical data. Authors in [68] have investigated inaccuracies and design influences of convective heat transfer in various machine components such as rotor-stator annulus, interfaces between components, and cooling jackets. The work illustrates that the stator lamination to the housing interface plays a significant role in the thermal modeling of electric drives. Authors in [69] have presented numerical simulations and evaluations of several axial fan designs and comparisons with typical centrifugal fans. The study has concluded that axial fans can increase the overall efficiency of unidirectional self-ventilated motors by lowering fan power while maintaining air velocity and useful volumetric airflow and not impacting motor operating temperature. A bidirectional electro-thermal modeling framework is presented in [70], which is iteratively coupled to accurately predict electromagnetic performance, i.e., efficiency, component-wise heat losses, and the corresponding temperature distribution of a jacket-cooled machine. A totally enclosed traction motor was developed in [71], where analysis has been presented for the radial fan of the motor. Here, an irregular pitch blade of the radial fan is developed to reduce acoustic noise. Heat transfer by conduction and convection through a finned housing of an electric motor for the drive unit of a vacuum pump has been investigated in [72]. In this work, the heat transfer has been numerically simulated using finite element approximation, and the housing surface’s temperature distribution has been determined. A 2-D conjugate heat transfer model has been presented in [73],

simplifying the simultaneous calculation of a fluid and heat flow problem. This method finds an optimized design for the cooling fins of a casted housing. An analytical calculation of the heat transfer coefficient of a complex housing shape of a TEFC industrial machine is presented in [74], which shows that for dominant motor passive cooling, most heat is extracted by combining natural convection and radiation phenomena. The motor considered in this work operates below its nominal speed or close to stalling. The proposed method can potentially predict convection coefficients in passive heat extraction conditions. A thermal model of an inverter-fed three-phase squirrel-cage induction motor is presented in [75]. The impact of the fundamental frequency voltage on steady-state temperatures and motor performance limitations can be analyzed with this model. The key parameters in slot liner selection and their effect on heat distribution in the stator of an electric motor are presented in [61]. Here, the thermal characteristic of the stator slot - interface air gap, insulation material, and impregnation have been analyzed. It is found that the thermal conductivity of the slot liner and impregnation material has the most significant influence on the winding temperature. A lumped parameter network-based thermal analysis of a three-phase induction motor during steady-state and transient regimes has been presented in [76]. Three continuous, short-time, and intermittent periodic duty cycles have been used for thermal analysis.

2.6 Research Gaps

The research gaps identified based on the previous discussion are as follows.

- There have not been any works that have developed driving profiles dedicated to the C-E3Ws available in Bangladesh, and no research has determined the traction load required for C-E3Ws over their respective driving profiles.
- The analytical sizing model in other research has limited parameter calculation for a PM-BLDC motor.
- There have not been any researches that propose FE based electromagnetic model for the PM-BLDC motor of C-E3Ws. In the existing literature, the FE-based model proposed for the BLDC motor lacks a thorough analysis of the geometric structure to loss analysis. Most of the works focus on one or more specific

sections. The overall design proposed in other works mainly focuses on performance on base speed-torque values only.

- The thermal analysis of a BLDC motor typically used for E3Ws has not been reported yet.

The research gap found is primarily due to the availability of C-E3Ws only in South Asian countries like Bangladesh. With the ever-increasing demand for E3Ws in Bangladesh, specifically C-E3Ws, research is required for its traction motor, the PM-BLDC motor. Driving profiles of C-E3Ws provide insights into motor torque and speed which enables determining motor design goals. Since the finite element model is a comparatively computationally expensive method, an analytical motor sizing model design with proper motor design parameters can reduce the number of variables to be studied and optimized in FEA. A 2D finite element analysis with additional parameter consideration for 3D structure can model the electromagnetic performance of the motor accurately. Moreover, a thermal analysis of the model is essential to determine its feasibility for the target application. With thermal analysis, it can be investigated whether the motor winding insulation is at risk of breakdown or whether the magnets can be demagnetized when the motor operates.

2.7 Summary

In this chapter, a comprehensive insight into various aspects of PM-BLDC motor design is presented. A literature review on motor design covering vehicles and machinery applications has been presented. Then an overview of research dedicated to the study of different motor parameters has been presented. Later, different areas of motor performance improvement have been explored, and methods to improve the performance have been reviewed. Next, an overview of the thermal analysis of different types of motors is presented to depict the necessity of thermal analysis to ensure the proper motor design. Besides, various parameters of thermal analysis have been explored. Afterward, drawbacks of the existing literature are outlined, and research gaps are depicted. This section concludes with prospective research outlines to cover the necessary research gaps for the design of PM-BLDC motor for C-E3Ws. In the above context, in the upcoming chapter, the driving profiles (velocity vs. time characteristics) of C-E3Ws are analyzed to determine the nominal motor speed and

nominal torque. Afterward, an analytical machine sizing is performed for the BLDC motor of C-E3W with the motor sizing equations. With parameter values received from analytical sizing and properly chosen design variables, a 2D finite element-based electromagnetic model of a PM-BLDC motor is designed to meet the design target goals, and various motor performances, including different motor losses, are determined. Later a thermal lumped parameter model is developed to determine the temperature of different motor components over the continuous motor operating torque range and previously recorded motor driving profiles. An experimental setup is used to measure the rated performance of a commercial C-E3W PM-BLDC motor and is compared with the designed PM-BLDC motor.

Chapter 3: Traction Load Analysis

In this chapter, an analysis is performed on the recorded three driving profiles of the C-E3W. Standard C-E3W parameters are considered for the analysis and prospective motor rated speed, torque, peak and continuous torques are determined which are used in analytical modelling, finite element analysis and thermal analysis.

3.1 Driving Profile Recording

The compact electric-3 wheelers (C-E3Ws) are primarily operated in different cluster areas of Dhaka City, contrary to large-sized E3Ws, widely available in the village and the suburban regions. In this work, Mohammadpur, kamrangichar, and Nakhalpara are the selected cluster areas for recording the driving profiles of the vehicle and, they are referred to as Area-1, Area-2, and Area-3, respectively. Non-invasive data logging system - GPS logger mobile application [77] has been employed here for ease of data collection[13], and the speed vs. time profiles of the C-E3Ws have been recorded while traveling in these areas. Round trips have been considered where in the first half of the duration, the C-E3Ws have traveled in one direction from start to destination, and in the final half duration, the vehicle returns to the starting point following the same route. The driving profiles of the three areas are shown in Figure 3.1.

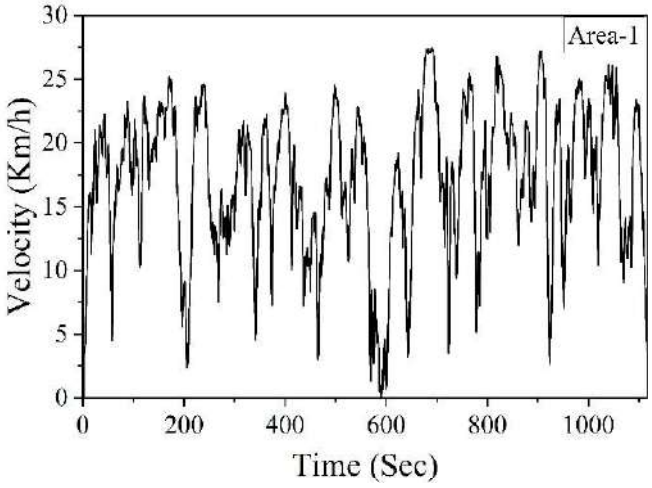

(a)

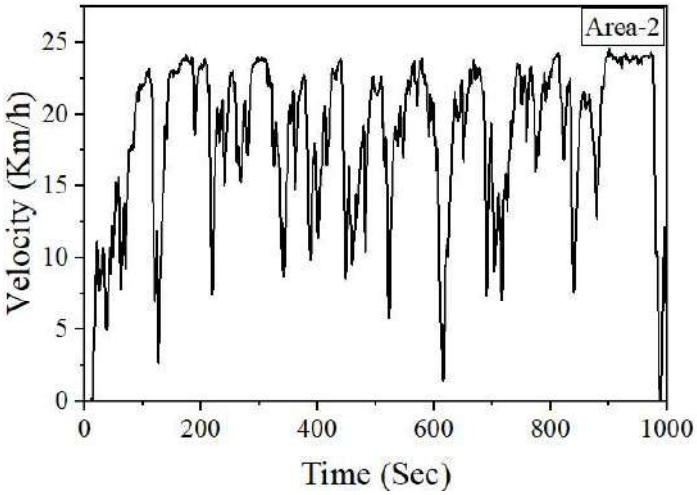

(b)

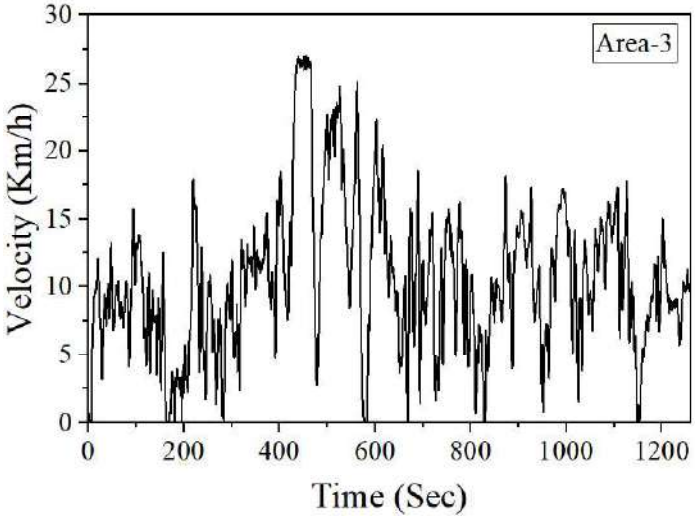

(c)

Figure 3.1: Driving profiles of (a) Area-1 (b) Area-2 and (c) Area-3

3.2 Motor Design's Rated Speed Determination

During the driving profile development, the number of passengers, including the drivers, their weight, travel time, and travel distance, have also been recorded, shown in Table 3.1.

Table 3.1: Additional information for the driving profiles

Parameters	Area-1	Area-2	Area-3
Total passengers (driver included)	3	4	4
Average Passenger weight (Kg)	65	70	62
Maximum Velocity (Km/h)	27.43	24.588	27
Distance Covered (Km)	5.414	5.07	4.15
Traffic Condition	Moderate	Moderate	Moderate
Approximate Travelling time (min)	19.216	18.252	21

The motor speed along the driving can be calculated using equation (1).

$$\omega_m = \frac{\pi}{30} \times G_r \times \frac{V}{r} \tag{1}$$

Where ω_m is the motor speed (rpm), G_r is the gear ratio, r is the tire radius, and V is the velocity at every point of the driving profile. The value of G_r for the C-E3W is 10. The motor speeds over the three velocity profiles are shown in Figure 3.2.

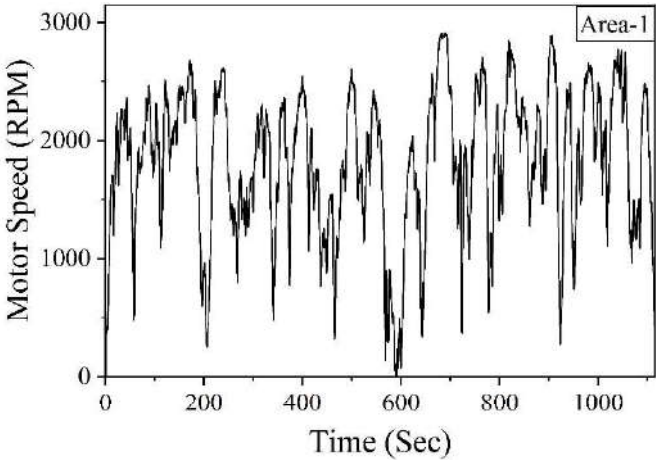

(a)

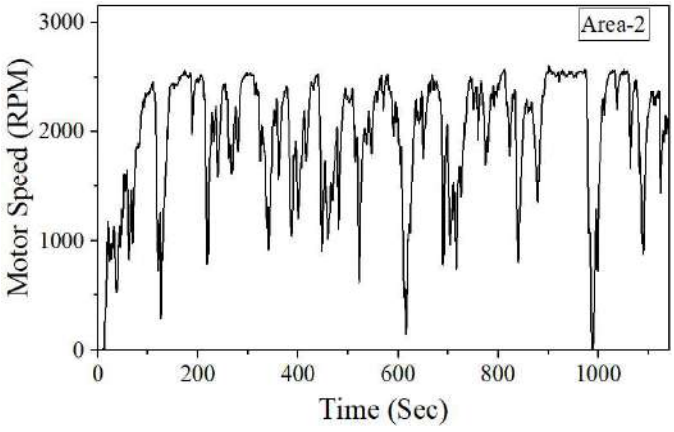

(b)

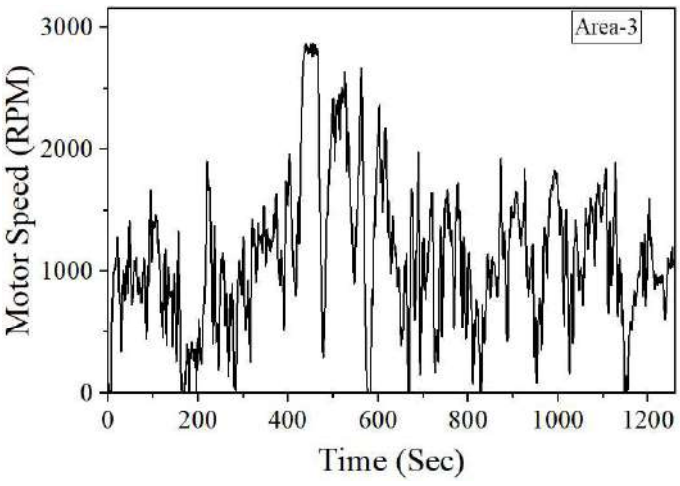

(c)

Figure 3.2: Traction motor speed over the driving profiles of (a) Area-1 (b) Area-2 and (c) Area-3

The calculated maximum motor speed is 2911 rpm, 2603 rpm, and 2865 rpm, respectively, for Area-1, Area-2, and Area-3 driving profiles. For the design purpose, the BLDC motor rated speed (ω_{rated}) is selected at 3000 rpm. The motor can run over its rated speed, but the BLDC motor inherently has a limited field weakening range.

3.3 Motor Design's Rated, Peak and Continuous Torque Determination

As the selected motor rated power (P_{rated}) is 1 KW, the rated torque (T_{rated}) can be calculated using equation (2).

$$T_{rated} = \frac{P_{rated}}{\omega_{rated(rad/s)}} \tag{2}$$

The value of the rated torque is 3.1831 Nm. A C-E3W must generate forces to counter opposing forces and provide the necessary acceleration to propel along the driving paths. These forces are rolling resistance force (F_{rr}), aerodynamic drag force (F_{Ad}), gradient force or hill climbing force (F_G), and acceleration force (F_{Ac}) [15, 45, 78]. An equation-based approach is adopted to calculate the required traction force and torque for propulsion over the considered driving profiles [79].

(1) Rolling Resistance Force

The opposing force caused by friction between the tire and the road is known as the rolling resistance force (F_{rr}) [45]. The total rolling resistance is the sum of all tire resistances and can be calculated using equation (3)[45].

$$F_{rr} = \mu_r mgcos\theta \tag{3}$$

Where m is the total mass (kg) of the vehicle, including the curb and payload, g is the gravitational acceleration (ms^{-2}) and θ is the gradient of the driving path and μ_r is the rolling resistance coefficient. The value of μ_r depends on different influences concerning tire, road, and vehicle dynamics making proper estimation of its value very complicated. Here, μ_r is considered as a linear function of vehicle velocity and can be calculated using equation (4)[80].

$$\mu_r = 0.01 \times (1 + \frac{3.6}{100}V) \tag{4}$$

(2) Aerodynamic Drag Force

A moving vehicle experiences a force exerted by the air known as aerodynamic drag force (F_{Ad}). The value of F_{Ad} can be calculated with a semi-empirical equation (5).

$$F_{Ad} = \frac{1}{2} C_D \rho A_f (V \pm V_A)^2 \quad (5)$$

Here, C_D is the drag coefficient, A_f is the frontal area (m^2), ρ is air density (Kg/m^3), V is vehicle speed, and V_A is the air velocity which can either increase or reduce F_{Ad} depending on its direction with respect to vehicle. The estimated frontal area A_f of a vehicle with dimensions of length (l), width (w), height (h) and ground clearance (g_c) can be calculated using equation (6).

$$A_f = w \times (h - g_c) \quad (6)$$

(3) Gradient Force

A downward weight component is produced when a vehicle goes up or down a slope. Depending on whether the vehicle is driving uphill or downhill, this component may oppose or assist the net tractive force. This force is called gradient force (F_G) [15, 81] and can be calculated using equation (7).

$$F_G = mgsin\theta \quad (7)$$

The value of θ is positive for the uphill slope and negative for the downhill slope.

(4) Acceleration Force

A vehicle changes its velocity along the driving path. The force required to increase the vehicle's velocity is known as acceleration force (F_{Ac}) which can be calculated using equation (8).

$$F_{Ac} = ma \quad (8)$$

Here, a is the vehicle acceleration (ms^{-2}) which can be negative if the vehicle's velocity decreases. The total traction force (F_{trac}) and torque (T_{trac}) required from the vehicle can be calculated using equations (9) and (10), respectively.

$$F_{trac} = F_{rr} + F_{Ad} + F_G + F_{Ac} \quad (9)$$

$$T_{trac} = F_{trac} \times r \quad (10)$$

The motor torque can be calculated using equation (11).

$$T_{motor} = \frac{T_{trac}}{G_r} \quad (11)$$

A standard C-E3W vehicle configuration has been taken into account for calculating the motor torque, and some standard vehicle dynamics parameters have been used. The considered drive cycle paths were decent flat asphalt roads with insignificant road gradients (both uphill and downhill). Determining the road gradient angle at all the points of the driving path is an extremely complicated task. As the drive cycles have been prepared for a round trip, the uphill gradient angle at a position in one direction is downhill from the opposite direction. Moreover, the gradient term cancels out over the entirety of a given trip, as suggested in [82]. Hence, for simplified calculation, the average gradient angle is considered zero. The structural specifications and dynamic parameters of the considered C-E3W are listed in Table 3.2.

Table 3.2: C-E3W parameters for traction load calculation

Parameter	Value
Total Vehicle Mass (Vehicle Curb Weight) (Kg)	350
Gravitational Acceleration (ms^{-2})	9.8
Road Angle (degree)	0
Aerodynamic Coefficient	0.45
Air Density (kgm^{-3})	1.225
Vehicle Dimensions (Length × Width × Height) (mm)	2150×910× 1790
Ground Clearance (mm)	250
Vehicle Frontal Area (m^2)	1.41
Air Velocity (ms^{-1})	0

The calculated motor traction torque over the driving profiles is shown in Figure 3.3.

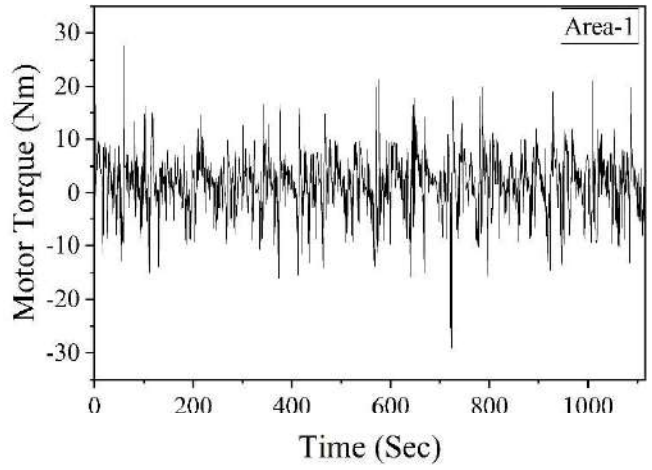

(a)

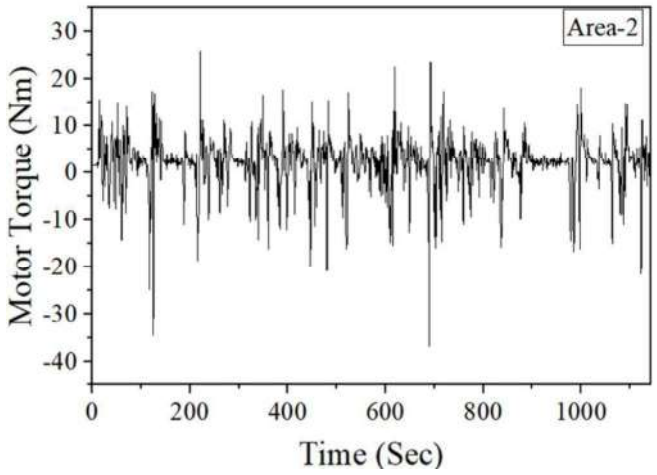

(b)

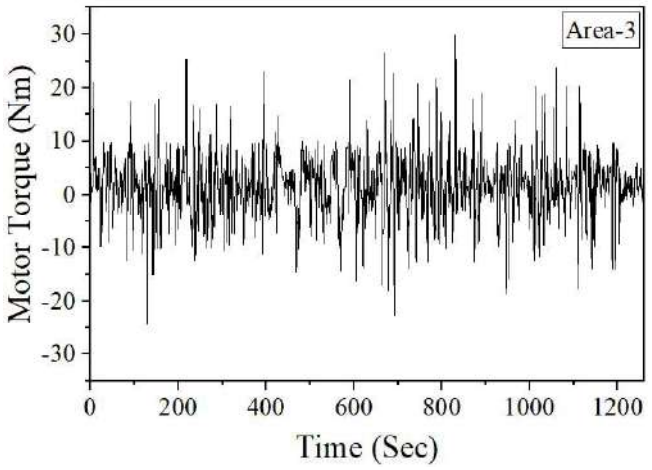

(c)

Figure 3.3: Motor Traction Torque over different driving profiles for (a) Area-1 (b) Area-2 and (c) Area-3

The C-E3Ws do not use regenerative braking features; hence the positive motor torque values are considered for analysis. The calculated motor traction torque and speed distribution along the three driving profiles are shown in Figure 3.4.

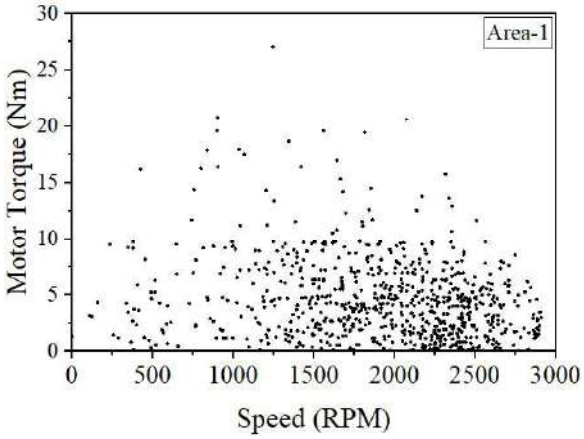

(a)

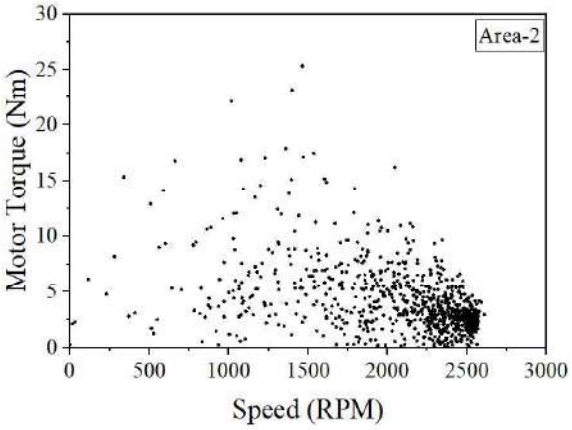

(b)

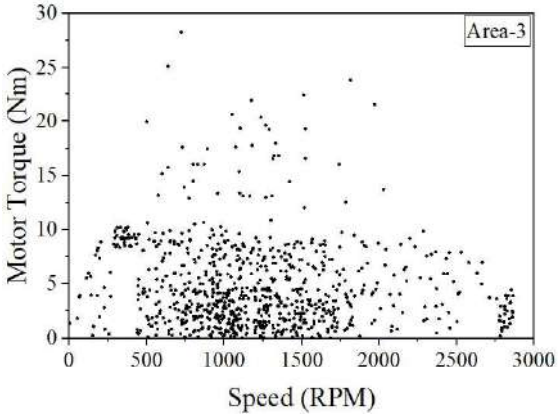

(c)

Figure 3.4: Motor torque speed distribution values over the driving profiles of (a) Area-1, (b) Area-2, and (c) Area-3.

During the start and acceleration, the traction motor is required to provide a higher torque value than its nominal or rated torque value. However, the torque values at some points over the drive cycles are very high or low. Most of these high torque values are primarily because of calculated high values of acceleration compared to suggested acceleration values in [21]. These values can be erroneous due to motor-rated power and unsophisticated cooling system. As the non-invasive method of data collection- the "GPS-Logger" mobile application depends on the accuracy of the GPS, the recorded data may be susceptible to error, especially at the vehicle's start condition, and the recorded velocity value may be recorded higher or lower than the actual value[13]. Also, during the traction torque calculation (T_{trac}), the average road gradient angle is considered zero. However, there can be mild to considerable uphill or downhill slope gradients along the path, increasing or decreasing the calculated torque value at different points of the driving profile. Despite errors, the distribution of motor torque over the driving profiles can provide enough insights into selecting motor peak torque value and continuous operation torque region. Therefore, the recorded time series data of motor traction torque is needed to be processed for filtering and grouping [13].

The positive motor torque values are considered for processing to determine the continuous operating torque range and peak torque value. The torque values over the three drive cycles are grouped into 0-5 Nm, 5-10 Nm, and > 10 Nm. The resultant motor torque value distribution is shown in Figure 3.5.

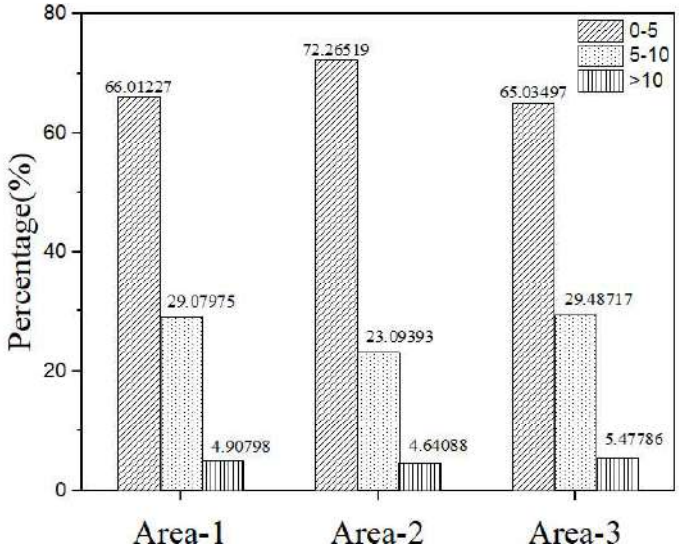

Figure 3.5: Motor torque value distribution over the three driving profiles

Figure 3.5 shows approximately 95% of motor torque values within 10 Nm, the 95th percentile among motor torque values. Considering 10 Nm as peak torque, the motor may go up to around 3.14 times its nominal value of 3.1831 Nm. Considering the maximum value of acceleration for the maximum speed range of E3Ws determined in [21], using the traction load calculation equations with C-E3W specifications mentioned in Table 3.2, the calculated maximum value of the peak torque is found to be 8.8 Nm. The road is also considered flat in this calculation since [34] suggested that E3Ws can run with maximum acceleration on a flat road. Therefore, the chosen value of peak torque for the C-E3W is valid. The ceiling torque value of the continuous operating region can be considered half of the peak torque value [16]. Therefore, the ceiling torque value of the continuous operating region is selected as 5 Nm, and Figure 3.5 shows that the C-E3Ws operated most of their driving time within 5 Nm torque which is approximately 1.57 times the rated value.

3.4 Summary

In this chapter, the driving profiles of C-E3Ws from three different regions of Dhaka City are presented. Standard C-E3W parameters are used to analyze the driving profiles to determine the motor design's rated motor speed, peak, and continuous torque. Motor rated speed has been chosen at 3000 rpm, which is higher than the maximum motor speed value calculated from the driving profiles considering the limited field weakening capability of the BLDC motor. For a 1 kW rated BLDC motor, with the determined rated speed, the calculated rated torque value is found to be 3.1831 Nm. The equation-based approach has been adopted to calculate the total traction force, including rolling resistance, aerodynamic drag, gradient, and acceleration. Road gradient has been considered null since the roads have been considered flat. Later, total traction torque over the driving profiles. The traction torque values have been analyzed and grouped. Considering data anomalies and possibilities of error from noninvasive GPS data application, the peak torque for the motor design is selected to be 10 Nm, about 95th percentile among the motor torque values from the driving profiles and 3.14 times the motor rated torque value. The motor's continuous torque is selected to be 5 Nm, which is half of the peak torque value and 1.57 times the rated torque value.

Chapter 4: Analytical Sizing Model for Motor

A permanent Magnet Brushless DC motor generally has trapezoidal back EMF, rectangular current waveform, rectangular distribution of magnet flux in the air gap, and concentrated stator windings [18, 81]. These motor fundamentals have been considered to develop an analytical sizing model for the PM-BLDC motor. The primary motor design goals are based on motor efficiency, torque, and speed. The considered motor-rated power is 1 KW. From the drive cycle analysis, the selected rated motor speed is 3000 rpm, and the corresponding rated torque is 3.1831 Nm. The efficiency target for the motor at rated conditions is set at 90%.

Finite element simulation is a computationally expensive method. Therefore, proper selection of motor design parameters can reduce the computation required in finite element analysis. Some parameters are selected depending on commercially available C-E3W BLDC motors, like the number of poles, slots, number of turns, approximate rotor diameter, winding configuration, and supplied DC voltage. They are shown in Table 4.1.

Table 4.1: Specification of a commercial C-E3W BLDC Motor taken for design

Parameter	Value
Number of slots (N_s)	12
Number of poles (N_p)	8
Rotor diameter (D_r)	70 mm
Shaft diameter (D_{sh})	20 mm
Winding configuration	Y-type
DC Voltage (V_{dc})	48 Volt

Other parameters are selected as design parameters as suggested by published literature. These parameters are discussed in this section.

4.1 Initial Electro-Magnetic Parameters

The input DC link current drawn from the battery and motor RMS phase current can be calculated using equations 12-14.

$$P_{in\_system} = \frac{P_{out\_motor}}{\eta_{motor} \times \eta_{inverter}} \quad (12)$$

$$I_{dc} = I_{ph} = \frac{P_{in\_system}}{V_{dc}} \quad (13)$$

$$I_{ph\_rms} = \sqrt{\frac{2}{3}} I_{ph} \quad (14)$$

Here, P_{out_motor} is the selected motor rated output power. The desired motor rated efficiency η_{motor} is chosen to be 90%. For inverter efficiency, $\eta_{inverter}$ is chosen at 95% at the rated condition for analytical sizing of the motor[83]. The detailed design, modeling, and analysis of the inverter model are out of the scope of this paper.

The RMS value of the motor phase current has been calculated using equation 14, considering that the motor operates in 120 degree conduction mode and the phase current is an ideal rectangular pulse current[18, 35]. The BLDC motor is considered to be run by the Hall-sensor based six step drive, and for initial motor sizing purposes, the peak value of phase current (I_{ph}) is equal to DC link current value(I_{dc}) [18, 81].

The rotor diameter to stack length ratio (ar) is chosen 2/3. The obtained initial value of stack length is $L_{stack} = 48$ mm. Considering the rotor as cylindrical geometry, the rotor volume (V_{rotor}) is found to be 1.84725×10^{-4}m^3.

The torque per rotor volume (TRV) in nominal conditions can be calculated using equation 15.

$$TRV = \frac{T_{rated}}{V_{rotor}} \quad (15)$$

The calculated TRV value is 17.2315 KNm/m^3. TRV can be expressed with respect to magnetic loading (B) and electrical loading (A) as shown in equation 16[39].

$$TRV = \frac{\pi}{\sqrt{2}} k_{w1} AB \quad (16)$$

Here, k_{w1} is the fundamental winding factor. For the 12 slot-8 pole combination, the value of k_{w1} is 0.866 [84]. For design purposes, the selected value of magnetic loading

in this work in 0.75 Tesla. The value of electrical loading (A) can be calculated from equation (17), and its value is found to be 11.68 KA/m.

In the considered BLDC motor, the phase current is rectangular and simultaneously, the current flows through 2 phases among the 3 phases. Therefore, the electrical loading (A) can be expressed as shown in equation (17)[39].

$$A = \frac{2mI_{ph}N_{tph}}{\pi D_r} \tag{17}$$

Here, m is the number of phases the current flows simultaneously, and for the BLDC motor, its value is 2. N_{tph} is the number of turns per phase which can be calculated from equation 17. The considered BLDC motor is a concentrated double-layer winding motor. Therefore, the number of coils is equal to the number of slots. The number of turns per coil (N_{tc}) is related to the number of turns per phase N_{tph} with equation (18).

$$N_{tph} = N_{tc} \times N_{spph} \times \frac{1}{N_p} \tag{18}$$

N_{spph} is the number of slots per phase, the value of which is 4. The winding configuration considered in this work has one parallel path. Hence, the value of N_p is 1. The value of N_{tc} calculated from equation 18 is 6.74. However, N_{tc} value must be an integer value; therefore, its rounded integer value is taken which is 7. Hence, following the calculations from equations 17-18, using the number of turns per coil (N_{tc}) to be 7, which is the same as the number of turns per coil used in commercial E3W BLDC motor, the number of turns per phase (N_{tph}) is calculated 28.

Magnet loading (B) is the average flux density over the rotor surface[85]. The total flux ($\emptyset_t$), flux under one pole ($\emptyset_p$), and flux flowing through each tooth ($\emptyset_s$) can be calculated with equations 19-21[18].

$$\emptyset_t = B\pi D_r L_{stack} \tag{19}$$

$$\emptyset_p = \frac{\emptyset_t}{N_p} \tag{20}$$

$$\emptyset_s = \frac{\emptyset_t}{N_s} \tag{21}$$

As the rectangular distribution of magnet flux in the air gap is considered, the average value of the fundamental flux density (B_1) and corresponding pole flux ($\emptyset_{p1}$) can be calculated using equations 22-23[35].

$$B_1 = \frac{8}{\pi^2} B \tag{22}$$

$$\emptyset_{p1} = \frac{B_f \pi D_r L_{stack}}{N_p} \tag{23}$$

The RMS fundamental phase back-emf can be calculated using equation 24.

$$E_{ph\_rms} = \sqrt{2}\pi k_{w1} \emptyset_{p1} f N_{tph} \tag{24}$$

Where, f is the fundamental frequency. The initial value of E_{ph_rms} is calculated as 17.2719 Volt.

4.2 Motor Initial Geometrical Parameters

4.2.1 Stator Geometry

The motor conductor current density of fan cooled motor is recommended to be between 5 to 10 A/mm^2 [39]. Considering the motor will also run over the nominal condition, the rated RMS current density (J_{rms}) value has been chosen as $5A/mm^2$. Copper is considered as the conductor's material, and stranded conductors are considered. The number of strands ($N_{strands}$) is selected as 16. The total copper area of a single coil ($cAsc$) and copper area of a single strand ($cAss$) is calculated using equation 25-26, respectively.

$$cAsc = \frac{I_{ph\_rms}}{J_{rms}} \tag{25}$$

$$cAss = \frac{cAsc}{N_{strands}} \tag{26}$$

The stranded conductor diameter and area is needed to be selected from commercially available conductors. Therefore, a conductor size is selected from the standard wire gauge table, which is the closest to the value calculated from equation 26. SWG 24 is selected as a stranded wire with a diameter 0.559mm and an area 0.2454 mm^2 [86].

The modified total coil copper area and RMS current density value can be calculated using equations 25 and 26, respectively. The modified RMS current density is 5.067 A/mm^2.

The value of bare slot fill factor (k_f) is selected as 0.5 which is generally achievable without incurring extreme cost[18]. The approximate slot area for a double layer BLDC motor can be calculated using equation (27).

$$A_{slot} = \frac{2 \times N_{tc} \times cAsc}{k_f} \tag{27}$$

The value of maximum stator tooth flux density (B_{st}) and stator yoke density (B_{sy}) is selected as 1.6 Tesla and 1.4 Tesla, respectively, which are within the ranges (1.6-2 Tesla & 1-1.5 Tesla) suggested in[87]. The stator tooth width and stator yoke width can be calculated using equations 28 and 29, respectively[18].

$$W_{st} = \frac{\emptyset_{st}}{B_{st} k_{st} L_{stack}} \tag{28}$$

$$W_{sy} = \frac{\emptyset_{p}}{2 B_{st} k_{st} L_{stack}} \tag{29}$$

Various slots configuration can be used to manufacture the BLDC motor. The trapezoidal type slots show better performance than round type slots in terms of output power and efficiency[40]. Hence a trapezoidal type slot is selected for the design.

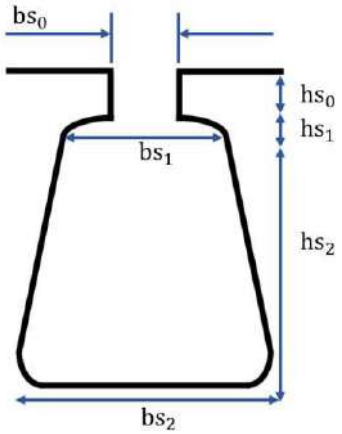

Figure 4.1: Selected Trapezoidal type slot parameters

The slot opening section, such as slot opening width (b_{s0}), slot opening height (h_{s0}), and height of tooth shoe(h_{s1}) are selected as design parameters. Other parameters are calculated by developing the geometry equations 30-32.

$$bs_1 = 2 \times (\tan\frac{\alpha_s}{2} \times \left(\frac{D}{2} + hs_0 + hs_1\right) - \frac{W_{st}}{2\cos\frac{\alpha_s}{2}}) \tag{30}$$

$$bs_2 = 2 \times (\tan\frac{\alpha_s}{2} \times \left(\frac{D}{2} + hs_0 + hs_1 + hs_2\right) - \frac{W_{st}}{2\cos\frac{\alpha_s}{2}}) \tag{31}$$

$$\frac{bs_1 + bs_2}{2} \times hs_2 = A_{slot} \tag{32}$$

Here, $\alpha_s = \frac{2\pi}{N_s}$ is the stator slot pitch angle; bs_1 is slot width at tail, bs_2 is slot width at tip and hs_2 is total slot height minus height of tooth shoe (h_{s1}). Lower value of The value of b_{s0} is preferrable for lower cogging torque but for conductor inserting into the slots, b_{s0} is needed to be chosen such that it is at least 2 times higher than a single winding strand diameter, and hs_0 has to be greater or equal to the lamination thickness[18]. The sharp edges of the trapezoidal slot have been blunted with the appropriate fillet. The slot dimensions are tabulated in table 4.

Table 4.1: Slot Sizing

Category	Notation	Value
Design Parameter	b_{s0}	1.5 mm
	h_{s0}	1.5 mm
	h_{s1}	0.75 mm
Parameter calculated from Geometry Equation	b_{s1}	10.616 mm
	b_{s2}	15.223 mm
	h_{s2}	8.595 mm

The slot opening is selected 1.5 mm which is 2.68 times the diameter of a single strand. The stator inner diameter (D), outside diameter (OSD), and motor split ratio (SR) can be calculated using equations 33-35, respectively.

$$D = D_r + 2a_g \tag{33}$$

$$OSD = D + 2\left(h_{s0} + h_{s1} + h_{s2} + w_{sy}\right) \quad (34)$$

$$SR = \frac{D_r}{OSD} \quad (35)$$

Where a_g is the air gap whose value is selected 1 mm because 1 mm air gap can make the field density value on the air gap higher when compared to the wider air gap under the same design conditions[8]. Moreover, considering mechanical and manufacturing concerns, it is suggested in [11] not to choose an air gap length below 1 mm. The value of D_r is 70 mm, OSD is 110 mm, and SR is 0.636, which is within the typical range of SR 0.55-0.65[30].

4.2.2 Rotor Geometry

Considering the TRV value of the designed motor, 17.232 KNm/m^3 ,which is in the range of 14-42 KNm/m^3 , the chosen permanent magnet is Neodymium-Iron-Boron (NdFeB) Magnets N42SH[39, 88]. Neodymium-Iron-Boron provides good performance and is cheaper than other rare earth-type magnets like samarium-cobalt[18].

A magnetic circuit model has been used to determine magnet thickness[18]. The magnet thickness (dm) can be calculated using equation 36.

$$dm = P_c * a_g * C_\emptyset \quad (36)$$

P_c is the permeance coefficient and $C_\emptyset$ is the flux concentration factor which is the ratio between the magnet cross-section area to the air gap cross-section area. $C_\emptyset$ can also be regarded as the pole embrace[51]. The initial value of $C_\emptyset$ is taken as 0.94. P_c can be calculated using equation 37.

$$P_c = \frac{K_r * \mu_r}{K_l C_\emptyset \frac{B_r}{B_g} - 1} \quad (37)$$

Here, K_l , K_r are the leakage factor and the reluctance factor, respectively. B_r is the remanence flux density. For the selected magnet grade N42-SH (at 60^oC), the value of B_r is 1.25 Tesla. μ_r is the relative magnetic permeance. The leakage factor K_l is defined as air gap flux to total magnet flux. Its value ranges from 0.9 to 1. The

reluctance factor can be referred to as the ratio of Magnetomotive force (MMF) generated by magnets to MMF over the air gap. K_r is used to simplify the magnetic circuit model by compensating for steel reluctance whose typical value ranges such that $1 < K_l \leq 1.2$. For initial magnet sizing, the value of K_l and K_r is chosen to be 0.95 and 1.1, respectively. The calculated initial thickness of the magnet is found to be 2.43 mm Using equation 39. For a selected magnet embrace ($C_\emptyset$), the optimum magnet thickness (dm) can be found through parametric simulation in finite element solver to receive desired magnetic loading (B) 0.75 Tesla.

The available length for the rotor yoke (W_{ry}) can be calculated using equation (38).

$$W_{ry} = D_r - D_{sh} - 2dm \tag{38}$$

The rotor in the designed BLDC motor is considered to have four ducts with 10 mm duct thickness, 75 degree angular arc and at a 5 mm distance from the shaft.

M19 24G electrical steel grade is chosen as the stator and rotor lamination material, and stainless steel has been chosen as the shaft material.

4.3 Excitation Circuit Parameters

The phase resistance (r_{ph}) and end inductance (L_{end}) are needed to be calculated as finite element solver cannot calculate them in 2D simulation.

To calculate the phase resistance, the total length of a single turn (L_{mt}) is needed to be calculated, which includes the stack length (L_{stack}), winding extension beyond stator lamination before bending into end winding (L_{xn}) and winding arc length or coil pitch (τ_{cp}). Using equations 39-40, the L_{mt} can be calculated.

$$\tau_{cp} = \frac{2\pi}{N_s} \times \left(\frac{D}{2} + hs_0 + hs_1 + \frac{hs_2}{2}\right) \tag{39}$$

$$L_{mt} = 2L_{stack} + 4L_{xn} + 2\tau_{cp} \tag{40}$$

The value of L_{xn} is considered 4.5 mm in the design.

The resistance of a single coil (r_c) and phase resistance (r_{ph}) can be calculated using equation 41-42.

$$r_c = k_{ar} \times N_{tc} \times \rho \times \frac{L_{mt}}{cAsc} \tag{41}$$

$$r_{ph} = r_c \times N_{spph} \tag{42}$$

Where ρ is the resistivity of the conductor at the considered 100°C temperature. N_{spph} is the number of slots per phase. k_{ar} is the ac resistance factor that considers the proximity effect and skin effect due to flow of ac current through the winding. [89]. As the phase current frequency is now high (200 Hz at 3000 rpm speed) and stranded conductors are considered, the value of K_{ac} can be considered 1. Following through equations 42-45, the calculated initial phase resistance value (r_{ph}) is 0.0257 Ω.

As in 2D simulation, FE solver cannot calculate the end winding inductance; therefore, an approximate value of the end winding inductance per phase can be calculated with equation (43)[18].

$$L_{end} = \frac{N_{spph}\,\mu_o \tau_{cp} N_{tc}^2}{2} \ln\left(\frac{\tau_{cp}\sqrt{\pi}}{\sqrt{2A_{slot}}}\right) \tag{43}$$

Using equation 43, the calculated value of end winding inductance is 2.673 μH.

4.4 Efficiency Calculation

The motor losses include winding copper loss(P_{cu}), core loss(P_{core}), magnet loss(P_{mag}), and mechanical loss(P_{mec}). For the motor output power P_{out} , the motor efficiency, η_{motor} can be calculated using equation (44).

$$\eta_{motor} = \frac{P_{out}}{P_{out}+P_{cu}+P_{core}+P_{mag}+P_{mec}} \tag{44}$$

The core loss and magnet loss can be calculated from the finite element solver. The mechanical loss is assumed as 1% of the output power, considering the complexity of determining the exact value of mechanical losses. The copper loss can be calculated using equation (45).

$$P_{cu} = 3I_{ph\_rms}^2 r_{ph} \tag{45}$$

4.5 Summary

In this chapter, the initial sizing of the motor is performed with corresponding motor sizing equations. Some parameters are selected similarly to commercial C-E3W PM-

BLDC motors such as, the number of slots, poles, supplied voltage, rotor diameter, shaft diameter, etc. Other parameters are chosen based on suggested values from literature and design considerations. Appropriate reasons for selecting these parameters have been described. The overall motor sizing covers electromagnetic parameters, including the number of turns per phase, phase back emf, magnet dimensions, etc. The sizing of stator and rotor geometry have also been performed which include slot dimensions, stator yoke width, rotor yoke width, rotor duct dimensions etc. Some parameters appropriately chosen for design are magnetic loading, rms current density, stranded wire diameter, some slot parameters, magnet embrace, etc. The goal of the initial sizing of the motor is to provide different parameters for the finite element-based electromagnetic modeling of the motor, to be presented in the next chapter. Since numerous parameters are involved in designing the motor, proper selection of some motor parameters reduces the computation time required for the FE solver to design the motor to meet the design targets. The geometry and electromagnetic parameters received in the analytical sizing provide the 1st step for FE modeling. These parameters can be updated over the iterative process in the FE solver. Proper initial sizing can significantly reduce the number of parameters to be examined and the number of iterations needed.

Chapter 5: Finite Element Analysis

In this chapter, the electromagnetic model of the designed PM-BLDC motor has been developed and optimized to attain the design goals.

5.1 Finite Element Method

Finite element analysis (FEA) is an important element in many sectors of engineering design and manufacture and is used by major established industries to simulate complex phenomena at different scales for the design and manufacture of high-technology products [90]. The finite element (FE) method is an advanced computational technique for solving differential and integral equations in engineering and applied sciences. The majority of real-world issues are specified on geometrically complex domains with varying boundary conditions along the boundary. The notion of finite element stems from the fact that a problem domain may be seen as an assembly of basic geometric objects called finite elements, for which approximation functions can be generated systematically. The finite element analysis of any problem involves basically four steps[91]. The 1st step is the discretization of the domain (Surface in 2D and volume in 3D) into a set of finite elements which is known as mesh generation[92]. The accuracy of the finite element analysis findings, as assessed by the precise solution of the mathematical model, is greatly dependent on the mesh used [93]. The second step is to derive governing equations for a typical element. A weighted-integral differential equation formulation is applied over a typical finite element (subdomain). The problem's weighted-integral form is used to create a finite element model. The finite element model is made up of a series of algebraic equations that represent the element's unknown parameters (degrees of freedom). The third step is to put all of the elements in the solution region together to get the global system of algebraic equations - for the unknown global degrees of freedom (GDF). The final step is to impose necessary boundary conditions, and the algebraic equations are solved to find the values in the global degree of freedom. By combining the equations for all the finite elements in a system, FEA can accurately simulate the overall behavior of GDF. Because the finite-element method (FEM) in the time domain can precisely model the operation of electric machines, it has been frequently utilized to compute the objective

functions in machine optimization [94]. FEM facilitates field analysis of electromagnetic problems with complex geometries [95]. FEM has become a commonly used tool in designing and optimizing electric motors because it can accurately simulate and analyze how motor parts work under different conditions. FEM models and studies the magnetic fields, electric currents, and mechanical forces created during operation in electric motors. FEM can forecast how a motor will perform and help identify areas for s to enhance the design of individual parts.

In this work, A 2-D finite element (FE) simulation has been performed in Ansys Maxwell software. A 2D parametric model motor has been developed using analytical motor sizing parameters. The total FE simulation process has been divided into two parts. At first, magnetostatics simulation will be performed to check if the value of selected magnetic loading is achieved and if magnetic flux density at different parts of the motor structure is within the designated flux density limit with the provided design parameters. If not, these parameters are updated with the software optimetrics feature, where the parameters are changed iteratively to observe the change in the output. A similar approach is followed for transient simulation, where the desired outputs are motor torque, phase currents, losses etc. The workflow is shown in Figure 5.1.

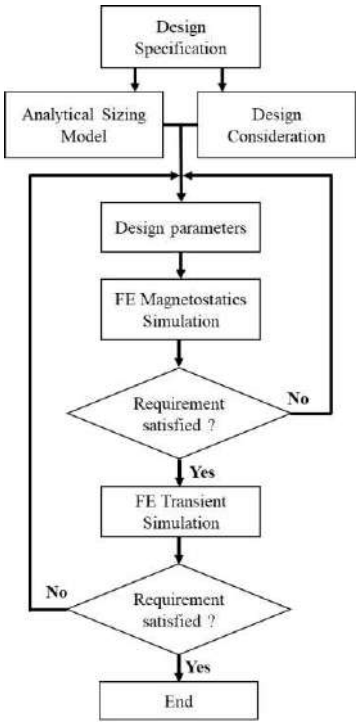

Figure 5.1: Flowchart of finite element motor design

5.2 Magnetostatic Analysis

Figure 5.2 shows a 2D structure of the designed PM-BLDC motor with the parameter received from motor analytical sizing.

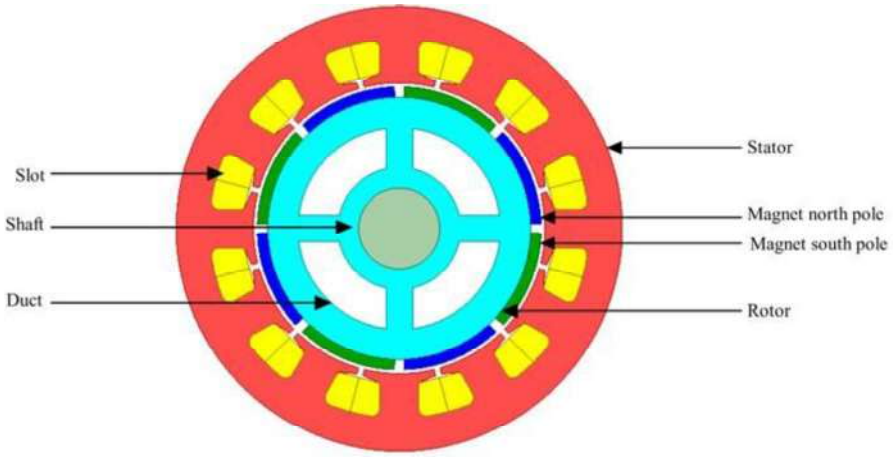

Figure 5.2: Two-dimensional diagram of the designed permanent magnet BLDC motor

In order to perform finite element analysis, numerous mesh is assigned over the motor geometry. The mesh size has taken 1 mm for magnets and 2 mm for other components of the motor. Figure 5.3 shows the mesh plot of the motor.

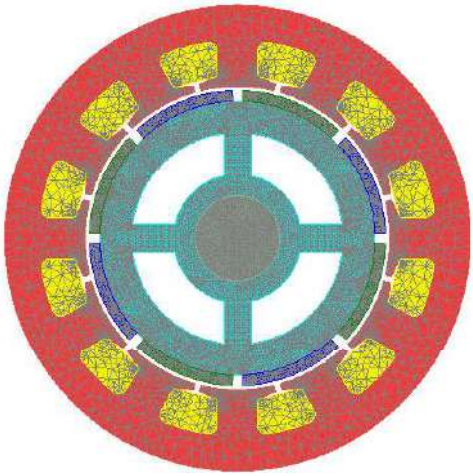

Figure 5.3: Motor mesh plot

Magnetic loading or average air gap flux density refers to the flux that goes to the stator through the air gap. Therefore, the radial component of the magnetic flux density is the main concern[96]. With the initial magnet dimension with a thickness of 2.43

mm and embrace 0.94, the obtained radial flux density value is 0.7467 Tesla, less than 0.75 Tesla selected as the design parameter. The magnet thickness has been varied from 2.43 mm to 2.85 mm, and the pole embrace value has been varied from 0.9 to 0.94 using the optimetrics feature of the finite element solver. Figure 5.4 shows the change of radial magnetic flux density or magnetic loading value with respect to the change of magnetic dimension for different pole embrace values.

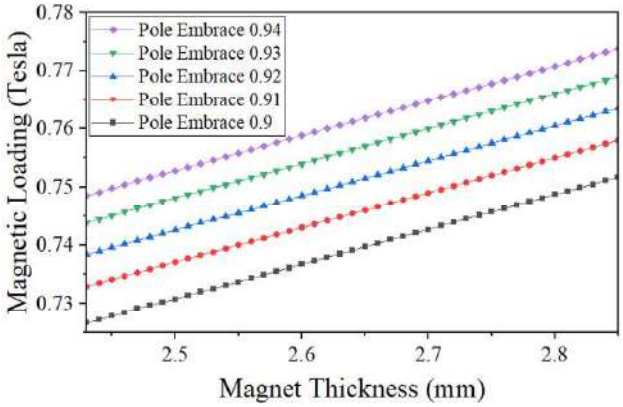

Figure 5.4: Magnetic loading variation with magnet thickness and pole embrace

At a magnet thickness of 2.46 mm, the magnetic loading value is 0.7504, close to the value chosen for the average air gap magnetic flux density. However, to facilitate manufacturing and proper dimensioning of the magnets, the chosen value of the magnet thickness is 2.5 mm. The corresponding magnetic loading for magnet thickness of 2.5 mm and embrace of 0.94 is 0.7527 Tesla. Figure 5.5 shows the radial component of air gap magnetic flux density aka, magnetic loading waveform.

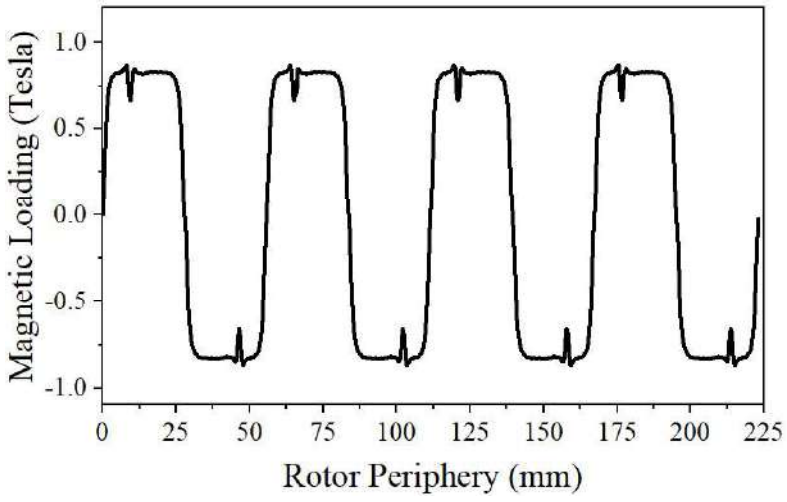

Figure 5.5: Radial magnetic flux density (Magnetic Loading)

Figure 5.6 shows the tangential component of air gap magnetic flux density, whose value is 0.0429 Tesla which is very lower compared to its radial component.

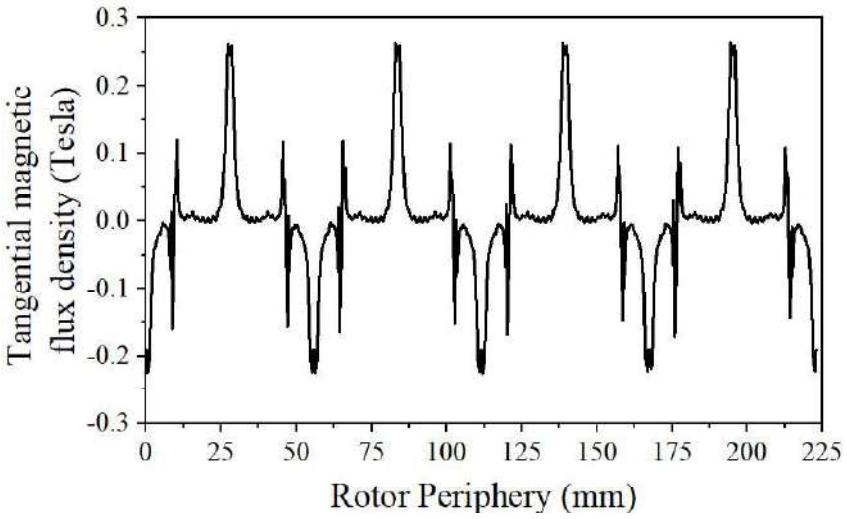

Figure 5.6: Tangential magnetic flux density

The value selected for the leakage factor and the reluctance factor were 0.95 and 1.1, respectively, which were used to initially predict the magnet thickness. However, for the optimum magnet thickness of 2.5 mm, these values can be determined via the FE solver post-processing operation using equations 46-47.

$$k_l = \frac{\emptyset_{g_{FE}}}{\sum_{i=1}^{Np} \emptyset_{pm_{FE}}} \tag{46}$$

$$k_r = \frac{\sum_{i=1}^{Np} MMF_{pm_{FE}}}{MMF_{g_{FE}}} \tag{47}$$

Where, $\emptyset_{g_{FE}}$, $\emptyset_{pm_{FE}}$, $MMF_{g_{FE}}$ and $MMF_{pm_{FE}}$ are flux and MMF for air gap and permanent magnets respectively. Performing the calculation in FE solver post-processing, the obtained values of k_l and k_r are 0.950176 and 1.1367, respectively. Using these values in equation (37), the obtained magnet thickness value from equation (36) is 2.507 mm, which is very close to the value of the selected magnet thickness of 2.5 mm.

Figure 5.7 shows the flux lines and magnetic field distribution over the motor rotor and stator structure under no load conditions.

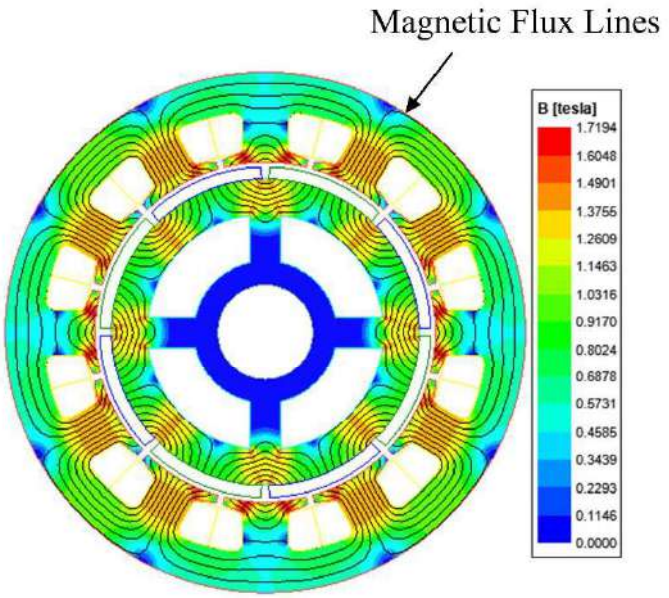

Figure 5.7: Magnetic flux lines and flux density over the rotor and stator periphery

From Figure 5.7, the maximum value of the magnetic flux density at the stator teeth ranges from 1.407 Tesla to 1.503 Tesla, which is below the maximum limit imposed for the design 1.6 Tesla. For the stator yoke, the maximum flux density at the stator yoke is around 1.321 Tesla near the teeth areas. This value is also lower than the considered maximum value of 1.4 Tesla. Although for the rotor, no such limit has been imposed in this work, the maximum value of magnetic flux density in the rotor yoke is around 1.354 Tesla which is below the limit of 1.5 Tesla for a salient pole motor suggested in [87]. Also, there are very small areas with higher values of magnetic flux densities. These paces can be regarded as hotspots, observed near the tooth shoe and the edge of the magnets. These hotspots typically change position with the rotor movement. The hotspot maximum flux density values for the rotor and the stator are 1.404 Tesla and 1.7194 Tesla, lower than the maximum permitted value of 1.5 Tesla and 2 Tesla, respectively, for salient pole machines[87]. With the rotation of the rotor, the flux density at different points changes. Flux densities higher than permissible limits increase the core loss of the machine and result in rapid heat in the machine[40]. Therefore, for design consideration, restrictions can be imposed on the upper and lower limit of magnetic flux densities on different parts of the motor[42]. Fig 5.8 shows the magnetic field vector from the magnets.

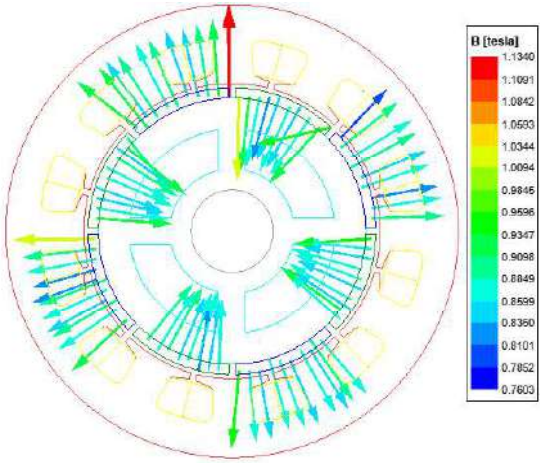

Figure 5.8: Magnetic flux density vectors of the permanent magnets

The Figure 5.8 shows that the magnetic flux density vectors are outwards for the north poles and inwards for south poles as, expected.

5.3 Transient Analysis

The electrical parameters, like torque, current, losses, etc., are determined in the transient simulation. One or more geometrical parameters are needed varied unless the target motor torque and efficiency at the rated speed are obtained. The first geometrical parameter chosen to be varied is the stack length. The initially chosen stack length was 48 mm. The shaft torque value obtained was 4.0228 Nm, higher than the value of the required rated torque, 3.1831 Nm. With the optimetrics features, the stack length has been varied from 48 mm to 50 mm. The near desired torque value has been obtained at the stack length of 49 mm. Other parameters are needed to be varied if the efficiency target of 90% is not met while keeping the rated torque value intact. The corresponding values of torque, power, and efficiency for different values of stack length are shown in Figure 5.31. The following results correspond to the stack length value of 49 mm.

5.3.1 Cogging Torque:

Due to slotting, permanent magnet mmf harmonics and the air gap permeance harmonics interact with each other, and cogging torque is produced. When a rotor tries to align in a number of stable positions, even when the machine is unexcited, cogging torque manifests itself. It results in a pulsating torque, which has no contribution to net effective torque. However, because it may generate speed ripples and induce

vibrations, especially at low speeds and under small loads, therefore, reducing it is typically a significant design priority [97]. As a rule of thumb, cogging torque in a permanent magnet motor should be no more than 5% of its rated torque for automotive applications. The considered motor has 12 slots and 8 poles. The cogging torque components expressed as the cycles per mechanical revolution (CPMR), depend on the number of slots and poles[56]. CPRM can be calculated with equation (48).

$$CPRM = LCM(N_p, N_s) \tag{48}$$

Here, LCM stands for least common multiple. N_p and N_s are number of poles and slots respectively. The number of cogging cycles per slot pitch (F) is defined as follows

$$F = \frac{CPRM}{N_s} \tag{49}$$

A higher value of F is preferable as the cogging torque with high CPMR exhibits low peak amplitude. For the considered 12 slot-8 pole motor the value of $CPRM$ and F are 24 and 2, which are comparatively lower than many slot-pole combinations used in electric motors. Therefore, the designed motor is likely to suffer from extensive cogging torque unless its minimizing methods are followed. Figure 5.9 shows the cogging torque in the designed motor without applying any reduction methods.

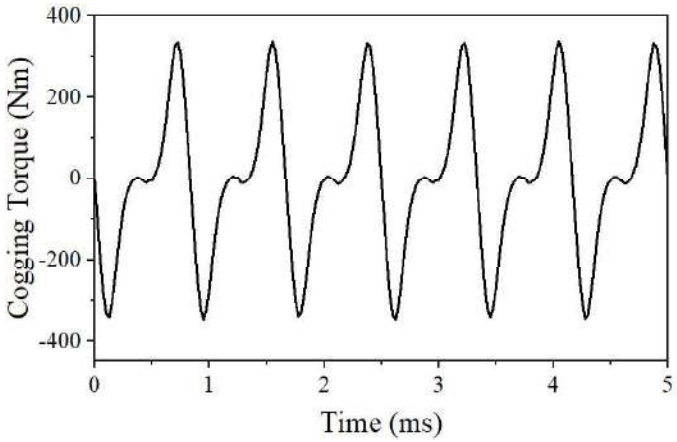

Fig 5.9: Cogging torque in the designed BLDC motor without its reduction methods

The peak-to-peak value of the cogging torque is 0.686 Nm, approximately 21.57% of the motor-rated torque. Therefore, it is necessary to adopt methods to reduce the

cogging torque. There are different ways to reduce the cogging torque in a permanent magnet motor[56]. In this work, rotor step skewing has been adopted[58]. In this process, the magnets are segmented along the stack length, and the segments are appropriately shifted to cancel the different CPMR components in the total cogging torque[56]. Considering the number of magnet slices (N_{slice}) 3 for the rotor magnets, the skew angle can be calculated using equation (50).

$$Skew\ Angle = \frac{360^o}{CPRM} \tag{50}$$

The obtained skew angle value is 15°, and the slice-to-slice angular distance is 5°. Figure 5.10 shows the cogging torque waveform after applying the rotor step skewing.

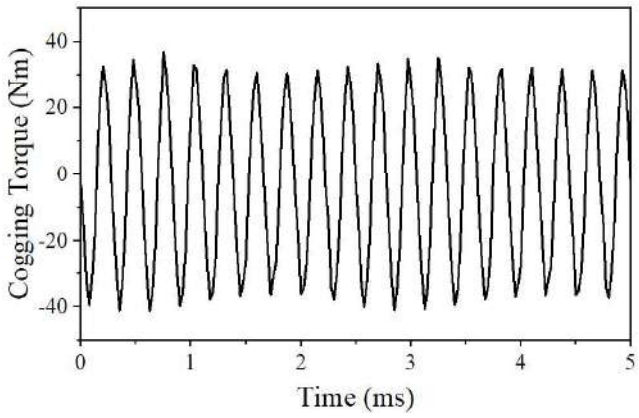

Fig 5.10: Cogging Torque after rotor step skewing

After the rotor step skewing, the peak-to-peak value of the cogging torque is 0.0781 Nm which is approximately 2.46% of the motor rated torque, which is acceptable. Figure 5.11 shows the skewed rotor of the designed PM-BLDC Motor.

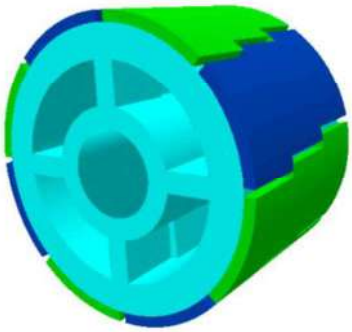

Figure 5.11: Rotor Step Skewing

5.3.2 Back EMF

The BLDC motor has been considered to be operated with the Hall sensor-based six-step drive. In this system, two phases out of three are excited with the phase currents, where one phase is with the highest value of induced voltage, and another is with the lowest induced voltage[18]. Six commutation instants are necessary per electrical cycle to perform to operate [81]. Figure 5.12 shows the phase back emf waveform.

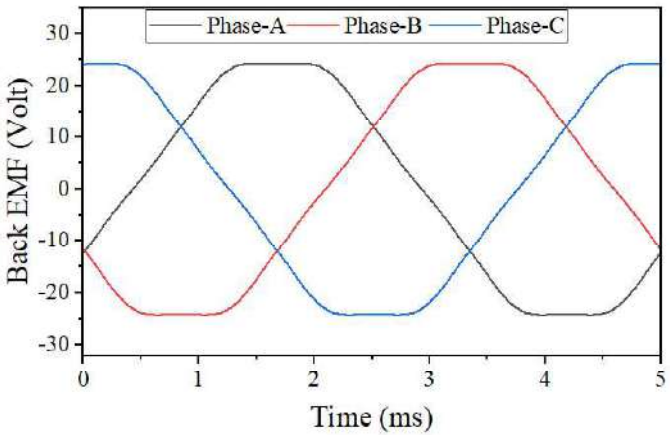

Figure 5.12: Induced phase back emf voltage at 3000 rpm speed

Figure 5.12 shows that the back emf waveform is trapezoidal, which is one of the fundamental characteristics of the BLDC motor. The RMS phase Back EMF value is found to be 17.9247 Volt. Using FFT, the fundamental value of the back emf seen from the source end is 42.11 Volt, as shown in the spectrum diagram of Figure 5.13.

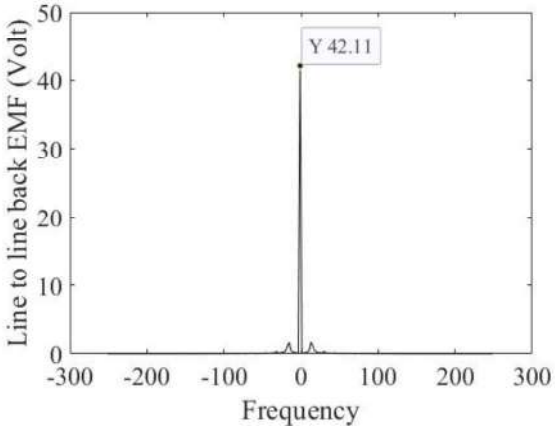

Figure 5.13: FFT of fundamental back emf spectrum seen from the DC voltage end

The flux linkage waveforms of the three phases are shown in Figure 5.14.

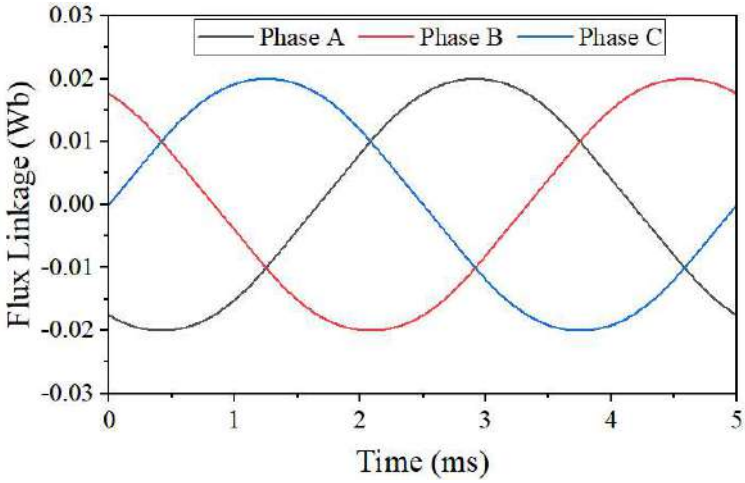

Figure 5.14: Flux linkage waveform

5.3.3 Winding Configuration

As the designed motor is of 12 slots double layered, there are 12 coils wounded across the stator teeth, and therefore, there are 4 coils per phase. The coil connectivity for a double layered 12 slot-8 pole motor is shown in Figure 5.15.

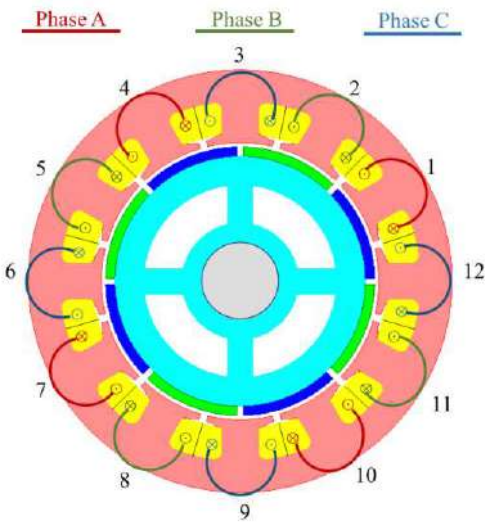

Figure 5.15: Winding connections according to different phases

5.3.4 External Circuit

The motor windings are excited with an external six-step drive-based motor driver. A simplified motor control circuit is shown in Figure 5.16.

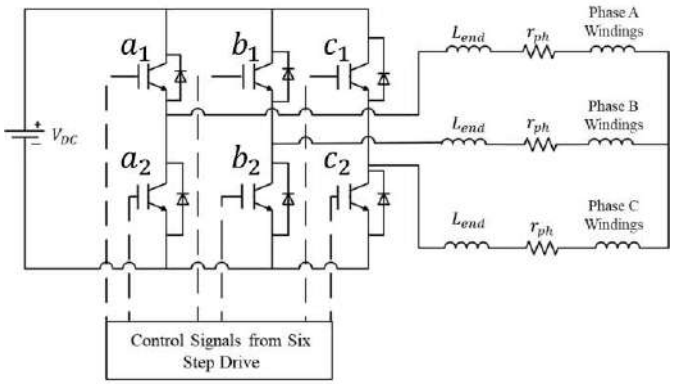

Figure 5.16: Six Step drive-based PM-BLDC motor controller Circuit

The circuit has been developed with Maxwell Circuit and coupled with Maxwell 2D FE solver. The switches are voltage controlled, and the control signal is generated using the six commutation points over an electric cycle. The voltage control switches' characteristics resemble the transistors (IGBT, MOSFET). The specified voltage drop across the switches and the diodes during the rated condition are measured at about 0.72 Volt. In each phase of the motor, there is an end winding inductance (L_{end}), phase resistance (r_{ph}) and motor phase coils. The updated values of r_{ph} and L_{end} are 2.67 μH and 0.026 Ω respectively. The switching control signals are generated based on the commutation points. In six step drive-based control system, at a time, two phases are energized; one phase with the highest positive back emf, and another is the highest negative back emf. Figure 5.17 shows the six-commutation points position with respect to the back EMFs of the three phases.

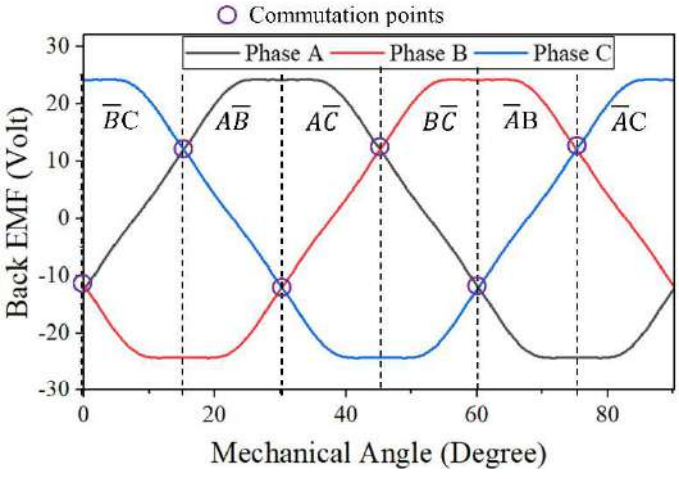

Figure 5.17: Commutation points and corresponding phases for six step control

The necessary settings for the control signals for the switches are shown in table 5.1 and corresponding wave shapes are shown in Figure 5.18.

Table 5.1: Controller switch control signals

Parameter	a1	a2	b1	b2	c1	c2
Initial Delay (deg)	15.222	60.223	45.220	0.2023	75.214	30.216
Rise Time(deg)	0.1	0.1	0.1	0.1	0.1	0.1
Fall Time(deg)	0.1	0.1	0.1	0.1	0.1	0.1
Pulse Width(deg)	30	30	30	30	30	30
Period(deg)	90	90	90	90	90	90

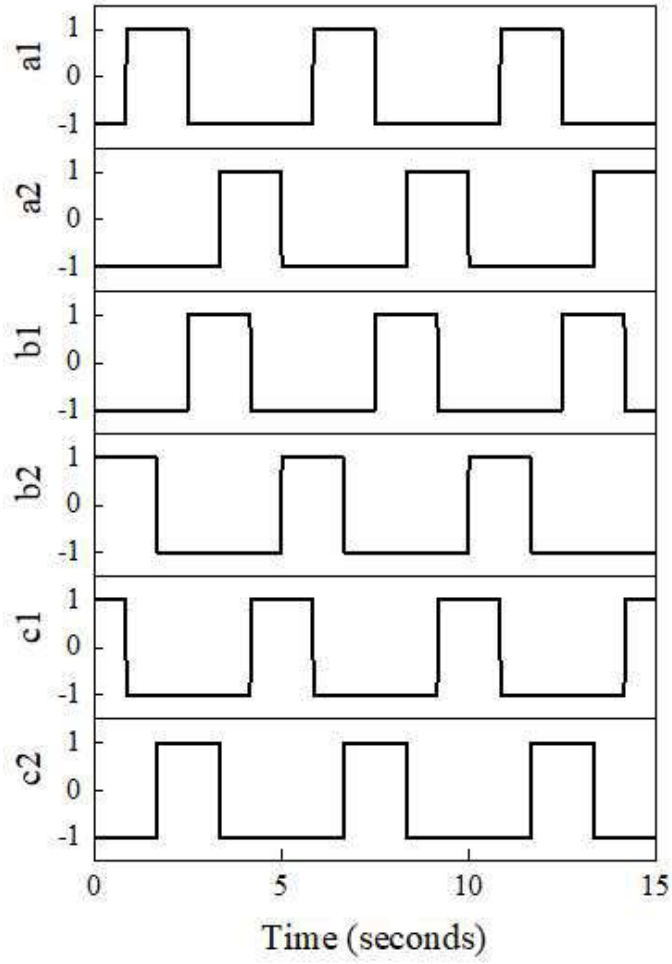

Figure 5.18: Switching signals for the six switches for six step control

5.3.5 Motor Torque Determination

From the finite element solver, the waveform of electromagnetic torque can be found as shown in Figure 5.19. The electromagnetic torque (T_{em}) can be found by averaging the values of the waveform over one electrical cycle or performing the Fast Fourier Transform (FFT). The calculated value of electromagnetic torque is 3.3697 Nm at 3000 rpm motor speed.

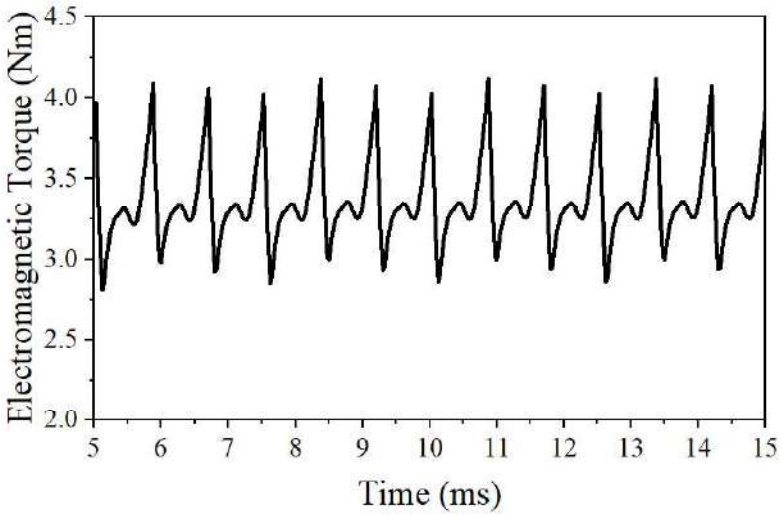

Figure 5.19: Electromagnetic Torque

The electromagnetic power can be calculated with equation 51.

$$P_{em} = \omega_m \times T_{em} \tag{51}$$

The value of P_{em} is found 1058.6224 Watt. To calculate the shaft power, the core loss (P_{core}), magnet loss (P_{mag}), and mechanical loss (P_{mech}), are subtracted from electromagnetic power as shown in equation 52.

$$P_{shaft} = P_{em} - P_{core} - P_{mag} - P_{mech} \tag{52}$$

The value of P_{core} and P_{mag} found from FE solver are 41.1272 Watt and 6.26 Watt respectively and the estimated value of P_{mech} is 10.1124 Watt. The calculated shaft torque is 1000.41 Watt. The determination of the loss values is discussed later in this chapter. The motor shaft torque (T_{shaft}) is calculated with equation (53).

$$T_{shaft} = \frac{P_{shaft}}{\omega_m} \tag{53}$$

The value of shaft torque is found 3.1844 Nm. The wave form of shaft torque is shown in Figure 5.20.

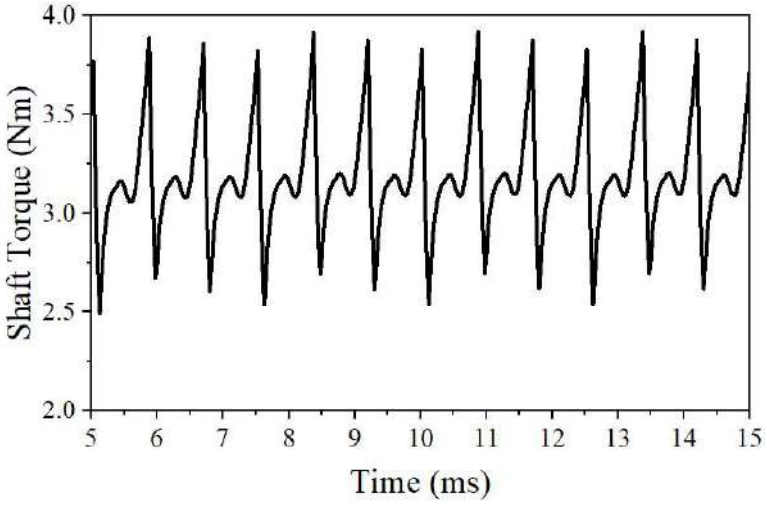

Figure 5.20: Shaft Torque

The FFT of the shaft torque waveform over an electric cycle is shown in Figure 5.21.

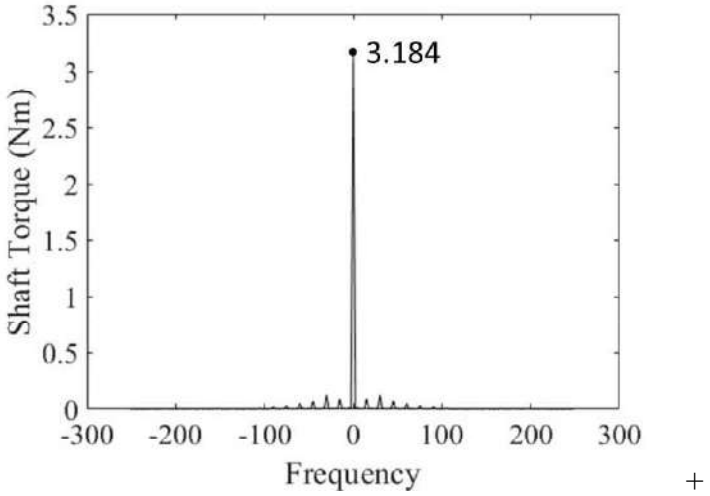

Figure 5.21: FFT waveform of shaft torque

The torque speed graph of the designed PM-BLDC motor is shown in Figure 5.22, where the peak torque is kept at 10 Nm as determined from section 3.3. The maximum phase rms current for the peak torque is determined to be 70 A.

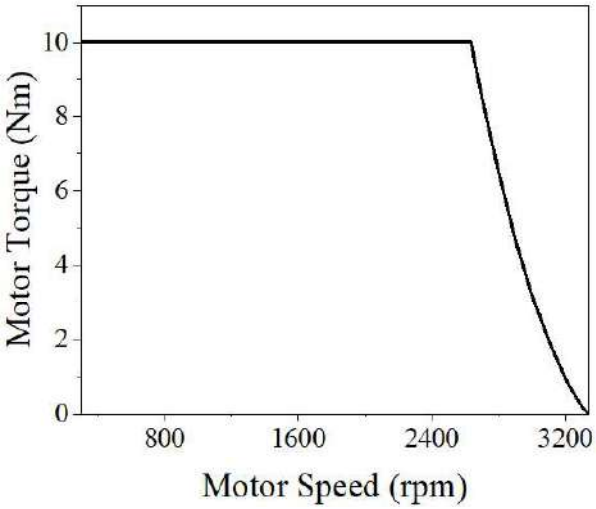

Figure 5.22: Designed PM-BLDC motor torque speed curve

From the torque speed curve of the designed PM-BLDC motor, maximum power at different motor speed can be found. The power vs motor speed curve is shown in Figure 5.23.

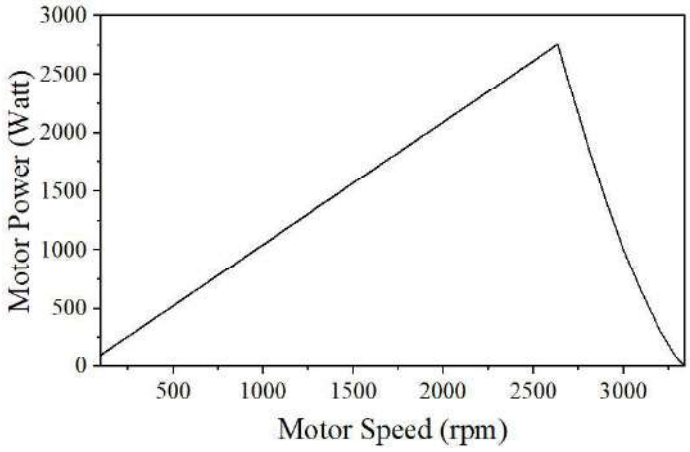

Fig 5.23: Designed PM-BLDC motor power speed curve

The maximum output power of motor is 2758 Watt.

5.3.6 Phase Current and Input DC current

The waveforms of phase currents and input DC current for the designed PM-BLDC motor is shown in Figure 5.24 and 5.25 respectively.

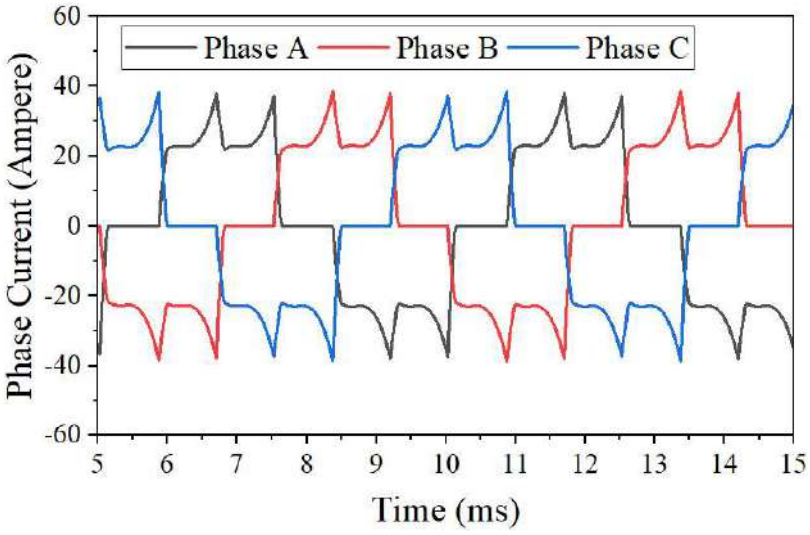

Figure 5.24: Designed PM-BLDC motor phase current

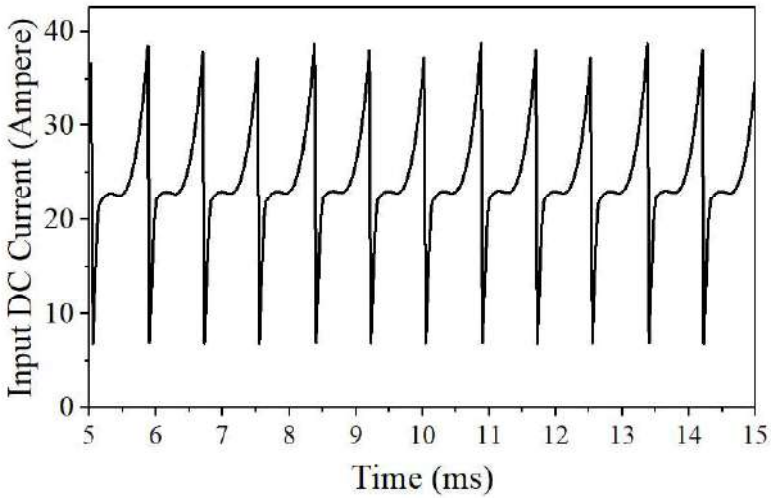

Figure 5.25: Input DC current to PM-BLDC current controller

The RMS value of the phase current is 21.194 Amp and the average input DC current is 24.243 Amp. Figure 5.21 shows that at an instance mostly two phases conduct currents and the current is zero at the other phase on that particular time. There are some instances where all three phases conduct for a small portion of time at which the switching takes place in six step drive control.

The phase voltage waveform is shown in Figure 5.26.

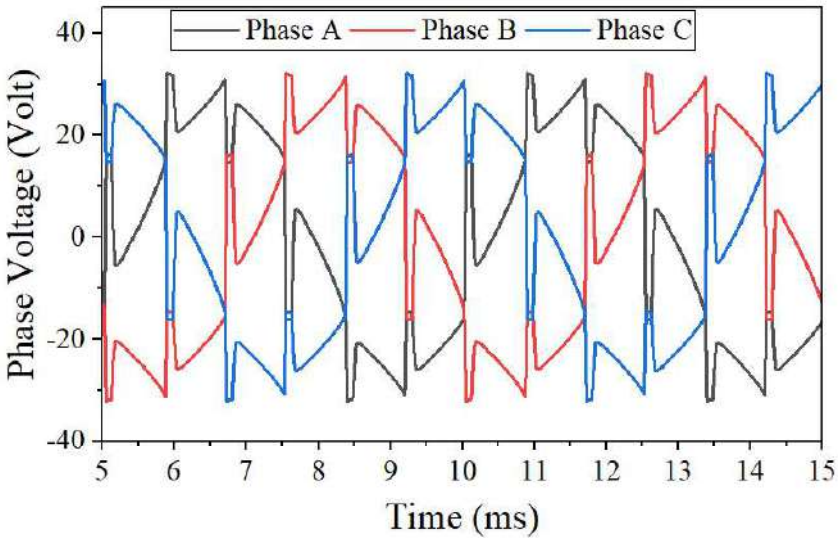

Figure 5.26: Three phase voltages of the motor drive

The rms value of phase voltage is 19.9517 Volt.

5.3.7 Motor Loss and Efficiency Determination

In a PM-BLDC motor, four types of losses are generally considered. They are core loss, magnet loss, copper loss, and mechanical loss. In this section, the losses in the rated condition of the motor are determined.

The core loss can be divided into three parts: the hysteresis losses, the eddy current losses, and the excess losses [98]. Hysteresis loss results from the magnetic reversal of the magnetic domains within the core material. Eddy current loss results from the induction of eddy currents within the core material[99]. Excess loss is an additional core loss component originating from the existing magnetic domains known as domain walls. The movement of the domain wall under the applied field produces an eddy current, and the corresponding loss is regarded as excess loss [100]. The magnetic flux density, frequency of the alternating magnetic field, shape and material of the core, and other parameters all influence core loss in a permanent magnet machine. The eddy current loss increases as the alternating magnetic field's magnetic flux density and frequency increase [35]. The core loss has a significant impact on operating temperature since it contributes to increasing motor temperature[101]. Figure 5.27 shows the waveform of core loss with its components.

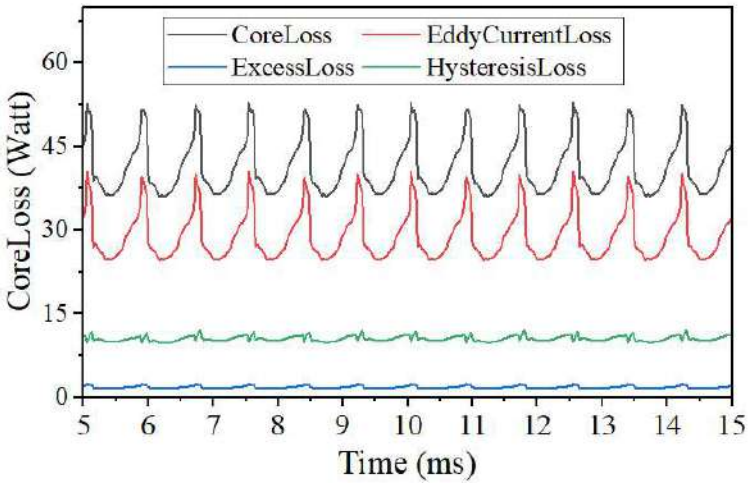

Figure 5.27: Designed PM-BLDC motor core loss

The average value of the core loss (P_{core}), is 41.1272 Watt. The eddy current loss, hysteresis loss and excess loss are 28.8086 Watt, 10.5397 Watt and 1.7789 Watt respectively. As can be seen that the eddy current loss component is the most dominant. In a PM-BLDC motor, , the permanent magnet field creates minimal core loss while the majority of the core loss takes place at stator tooth and stator yoke [18]. In a PM-BLDC motor, the magnet loss is due to eddy-current losses in the PM volume[81]. Figure 5.28 shows the figure of magnet loss in the designed PM-BLDC motor. The average value of magnet loss is 6.26 Watt.

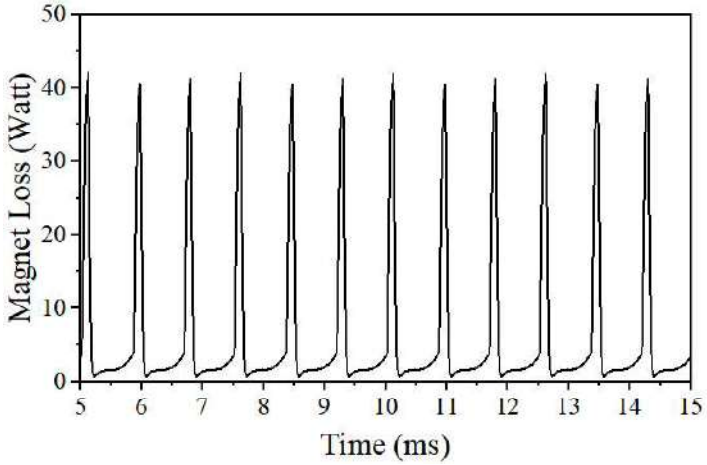

Figure 5.28: Designed PM-BLDC motor magnet loss

The copper loss has been calculated with post-processing from the FE solver. For the stack length value of 49 mm, the updated phase resistance 0.026 Ω. Using the equation 54, the waveform of copper loss is found which is shown in Figure 5.29

$$P_{cu} = (I_a^2 + I_b^2 + I_c^2) \times r_{ph}\big|_{avg} \tag{54}$$

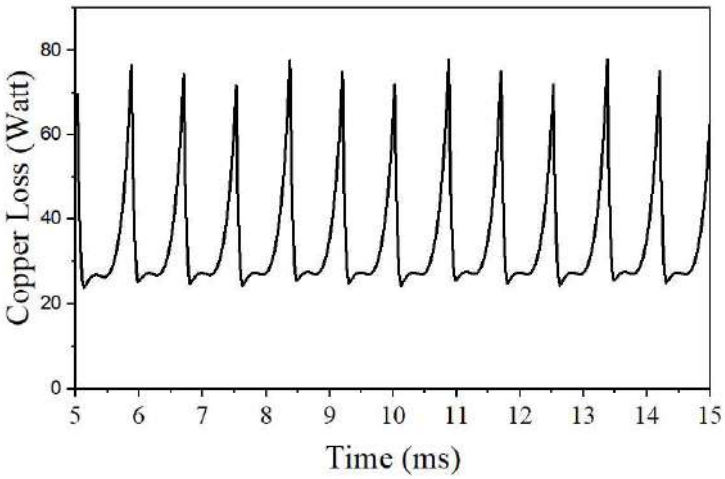

Figure 5.29: Designed PM-BLDC copper loss

The calculated average copper loss is 35.0408 Watt. The calculated copper loss with equation (45), for phase rms current value of 21.194 Amp, the calculated copper loss is 35.036 Watt which is identical to the value calculated through post-processing using equation (55).

The mechanical loss includes air friction, windage losses, and gear losses. Determining the mechanical losses is very difficult because fluid dynamic phenomena are associated with them[102]. As reported in [103], the mechanical loss is linked to the speed of the machine and the output power. Therefore, the value of the mechanical loss is approximated for efficiency calculation. It is assumed that the mechanical loss is 1% of the output power, which is resulted from subtracting core loss, and magnet loss from electromagnetic power, as shown in equation (55).

$$P_{mech} = 0.01 \times (P_{em} - P_{core} - P_{mag}) \tag{55}$$

The calculated value of P_{mech} is found 10.1124 Watt which is approximately 11% of the total losses (P_{loss}) which can be calculated from equation (56) which is comparable to 12% of the total losses suggested in [103] for 90% efficient permanent magnet motor.

$$P_{loss} = P_{core} + P_{cu} + P_{mag} + P_{mech} \tag{56}$$

The motor input power (P_{in}) and efficiency (η_{motor}) can be calculated using equation 57 and 58.

$$P_{in} = P_{out} + P_{loss} \tag{57}$$

$$\eta_{motor} = \frac{P_{out}}{P_{in}} \tag{58}$$

The calculated value of motor input power (P_{in}) is 1092.93 Watt and efficiency (η_{motor}) is 91.53 %.

The efficiency map refers to the efficiency value at different torque and speed values. Several steps have been followed to determine the efficiency map of the PM-BLDC motor with the FE solver. Firstly, the motor speed has been varied from 300 rpm to 3300 rpm. The maximum torque available with unrestricted current values is determined, and corresponding current values and waveforms are found. For a particular speed, the motor is energized with different current values with corresponding frequency, and the values of torque and losses are found for each current value. Using linear interpolation, the torque and values of the losses are found for torque values of 0.2 Nm to 10 Nm. The process is repeated for speed values of 300 rpm to 3300 rpm in steps of 300 rpm. Following the equations from 56 to 59, the efficiency at the torque-speed points can be determined. Following the equations from 56 to 59, the efficiency at the torque-speed points can be determined. Figure 5.30 shows the efficiency map for the PM-BLDC motor.

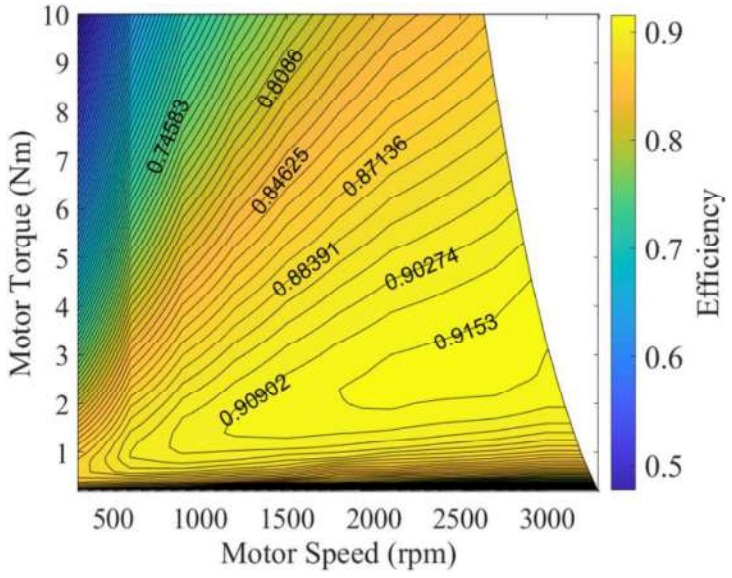

Figure 5.30: Efficiency map of the designed PM-BLDC motor

5.3.7 Other Parameters

The voltage and the current wave form for phase A are shown in Figure 5.29(a) and (b) respectively.

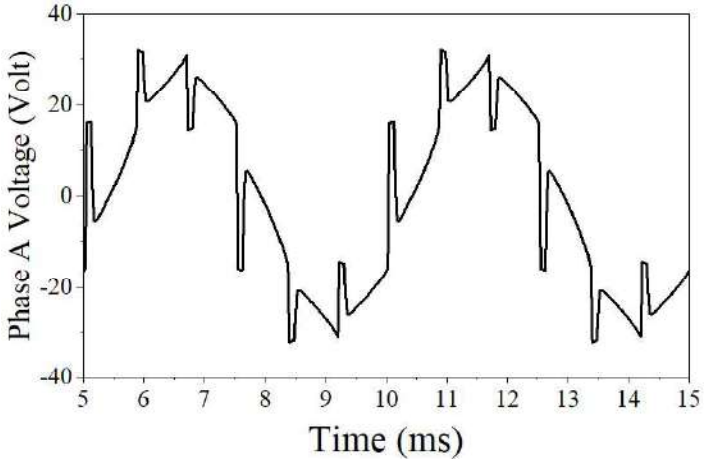

(a)

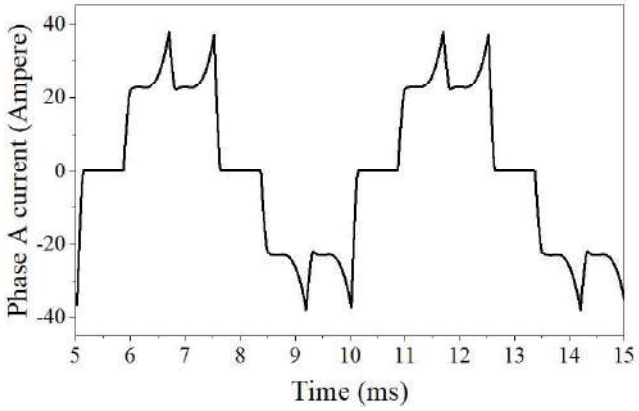

(b)

Figure 5.31: (a) Phase A voltage (b) Phase A current waveforms

The power factor (PF) of the PM-BLDC motor can be calculated using equation 59.

$$PF = \frac{P_{in}}{3V_{rms}I_{rms}} \tag{59}$$

The value of PF is found 0.8615.

From the FE simulation, the value of inductances: self-inductance, mutual inductance, d-axis inductance, and q-axis inductance can be found. Figure 5.32-5.33 shows the waveform of the inductances.

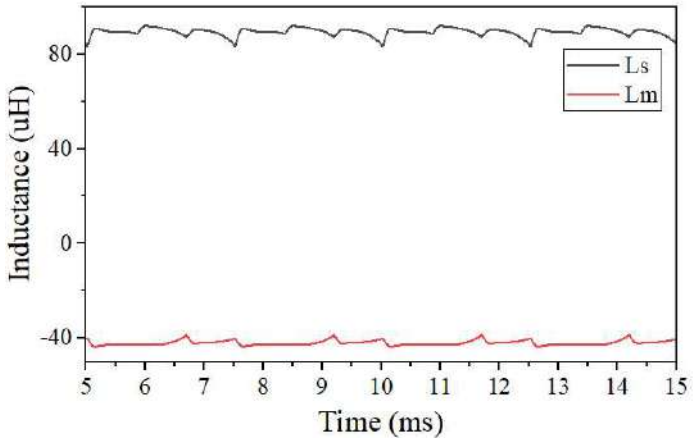

Figure 5.32: Self and mutual inductance waveform of the PM-BLDC motor

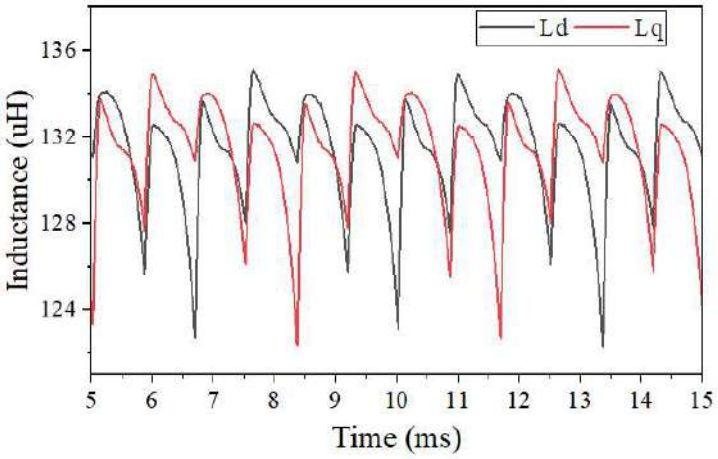

Figure 5.33: d-axis and q-axis inductance waveform of the PM-BLDC motor

The average values of self and mutual inductance are found 89.5024 μH and -42.0306 μH respectively. The negative sign of the inductance value refers to mutual. The d axis and q axis inductances value are found 131.6041 μH and 131.383 μH respectively. The values of L_d and L_q are identical which is a characteristics of a surface mounted permanent magnet motor [104].

5.3.8 Performance Analysis with Parameter Variation

The stack length has been varied from an initial value of 48 mm to 49 mm in 0.5 mm step. As can be seen from Figure 5.34, the desired rated power and torque have been achieved at the stack length of 49 mm. Also, the efficiency is 91.53% at a stack length value of 49 mm, the highest among efficiencies corresponding to other stack length values.

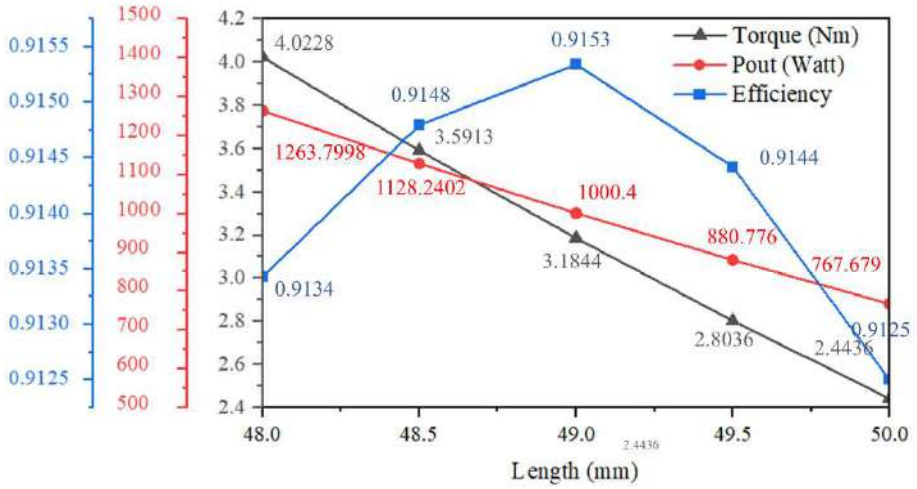

Figure 5.34: Torque, output power and efficiency variation for different stack length values

5.3.9 Final Motor Geometry

The final geometry of the designed PM-BLDC motor is listed in Table 5.2. These parameters are used to develop a 3D model for the lumped parameter based thermal model.

Table 5.2: Designed PM-BLDC motor geometrical parameter

Main object	Symbol	Value
Outer stator diameter (mm)	OSD	110
Stator inner diameter (mm)	D	72
Stator yoke width (mm)	W_{sy}	8.18
Stator tooth width (mm)	W_{st}	9.545
Slot opening width (mm)	b_{s0}	1.5
Slot opening height	h_{s0}	1.5
Height of tooth shoe	h_{s1}	0.75
Slot width at the bottom	bs_1	10.617
Slot width at the top	bs_2	15.223
Slot height tip to bottom	hs_1	0.75
Slot height bottom to tip	hs_2	8.595
Air gap (mm)	a_g	1

Main object	Symbol	Value
Rotor diameter (mm)	D_r	70
Magnet thickness (mm)	dm	2.5
Pole Embrace	$C_{\emptyset}$	0.94
Shaft Diameter (mm)	D_{sh}	20
Stack Length (mm)	L_{stack}	49
Duct thickness (mm)		10
Duct distance from shaft (mm)		5
Duct outer arc (deg)		75
Total Shaft length (mm)		180

Figure 5.35 shows the 3D visualization of designed PM-BLDC motor prepared in Motor-CAD.

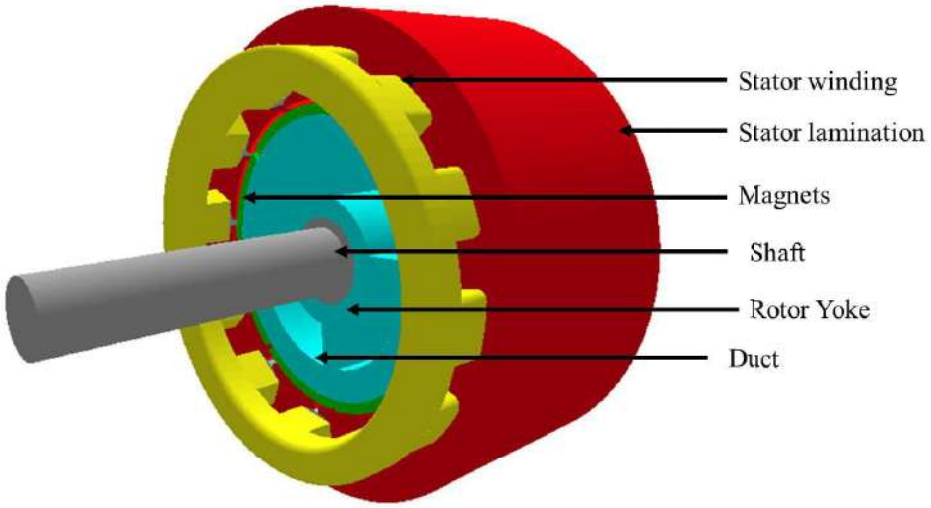

Figure 5.35: Designed PM-BLDC motor 3-D Design

5.3.10 Summary

In this chapter, a 2-D finite element model of a PM-BLDC motor has been developed using Ansys Maxwell Finite element solver. The initial motor parameters used are received from the analytical sizing model. The finite element simulation has been performed in two parts. In the first part, magnetostatics simulation is performed to determine the magnet thickness and embrace for the motor design based on the radial

magnetic flux density or magnetic loading value. In this simulation, the maximum magnetic flux density or magnetic field at different parts of the motor (Stator teeth, yoke, rotor yoke) have been observed to check if these values are within the suggested range. The results have been found satisfactory. The flux lines and vector lines found from the simulation validate the magnetic performance of the motor; the magnetic field lines and vectors are outwards for north pole magnets and inwards for south pole magnets. In the second part, transient simulation has been performed. The Motor Stack length has been varied, and an optimum value for the stack length is found. With the updated motor structure different motor parameters have been determined. To reduce the cogging torque of the motor, rotor step skewing has been adopted. The back emf waveform of the PM-BLDC motor isto be trapezoidal, a characteristic of the BLDC motor. An external controller circuit has been developed in the Maxwell circuit and coupled with the motor model to provide the excitation current to the motor phases. The waveforms of the motor shaft torque, phase currents, controller input currents, losses, and inductances have been observed. The phase current of the motor is a quasi-rectangular wave in nature. The motor efficiency and the power factor have been determined. The motor design goals in terms of motor speed, torque, power, and efficiency have been satisfied. The designed PM-BLDC motor torque and efficiency maps have been plotted to observe the maximum torque available at different motor speeds and efficiency at different torque and speed points.

Chapter 6: Thermal Analysis

In this Chapter, a lumped parameter model has been developed in Ansys Motor CAD to perform the thermal analysis of the designed PM-BLDC motor through analytical sizing and finite element analysis. During transient analysis, the thermal network is based on resistors, power (current) sources, and a capacitance network [62, 105]. Nodes are automatically placed at important points on the motor cross-section, such as the stator back iron, tooth, winding hotspot, etc. These are linked with conduction, convection, and radiation thermal resistances [105]. Resistances are used to represent the principal heat transfer paths within the machine, and their values are determined by the dimension and thermal conductivity of the material. The lumped parameter system requires the geometric dimensions of the motors, material properties, and the value of losses as input data [62]. Losses are input at the relevant nodes [105]. The geometric and physical properties can be parameterized[106].

A collection of geometric characteristics, such as housing Type (cylindrical, square, radial fins, axial fins, etc.), Tooth Width, Slot Depth, and so on, determine the geometry of the motor. A variety of cooling options are available. A thermal resistance network (including losses and thermal capacitances) is automatically generated based on the shape, cooling types, and materials chosen to perform steady-state and transient thermal computations. The model predicts the temperatures of significant nodes inside the machine shape (such as the housing, tooth, back iron, winding hotspot, and so on). All thermal resistances and capacitances in the network are estimated automatically using conventional analytical heat transfer theory based on the design, cooling method, and materials employed. Motor-CAD includes several specifically developed mathematical techniques that enable precise thermal calculations for the winding, and interface between different components, which are the most difficult to analyze [107]. By defining machine geometric dimensions and material composition, a network of thermal resistances, power sources, thermal capacitances, and nodal temperatures is generated [108]. Therefore, the convective and the radiation heat transfer parameters adopted are the default thermal model parameters provided by the software [62].

The losses calculated from the finite element analysis are used to determine the temperature of different motor components. The motor's housing and cooling system

is considered identical to the commercial C-E3W PM BLDC motor. Commercial PM BLDC motor housing parameters are measured, and these values are used for the simulation. The following parameters are calibrated in MotorCAD for thermal analysis.

- Motor Housing (Housing thickness, fin dimensions)
- Cooling system (cooling type, cooling fan speed characteristics)
- Winding arrangement (slot liner thickness, minimum conductor separation)
- Gaps at the specific interfaces (Housing-stator lamination, slot liner-stator lamination

6.1 Motor Housing and Cooling System

The designed BLDC motor is considered a totally enclosed fan cooled (TEFC) motor where a fan is lifted to the end of the shaft, and the fan blows air in an axial direction over the outside of the housing [64, 71]. The considered fan is a small radial centrifugal type [69]. Outside air is drawn into the fan cover through the inlet cowling as the fan rotates and then travels past the blades. Air is compressed and expanded within the fan cover at the inlet. The fan forces air over the motor frame fins, cooling the motor [71]. Figure 6.1 shows the overall configuration of the motor, including its housing and cooling.

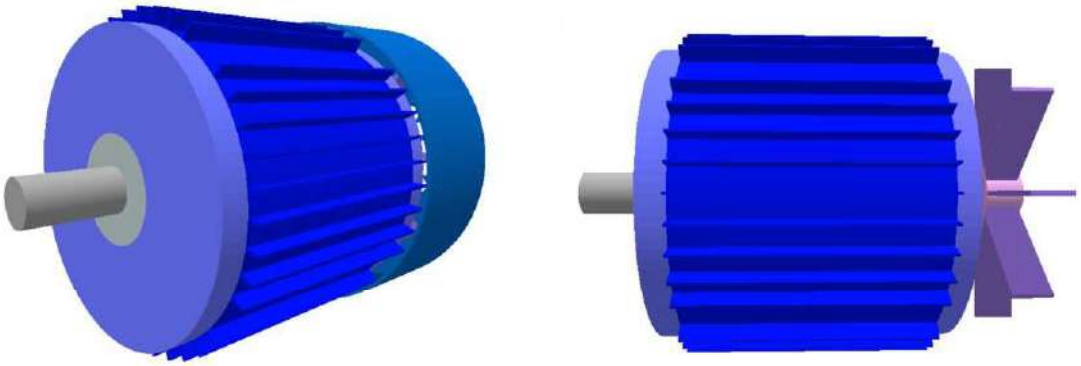

Figure 6.1: Designed BLDC motor housing and cooling configuration

The geometrical specification of the designed motor housing and fan is shown in Table 6.1.

Table 6.1: Geometrical Specification of motor housing and cooling fan

Parameter	Value
Housing Thickness (mm)	3
Fin Extension (mm)	6
Fin Thickness (mm)	1
Total number of Fins	36
Fan Diameter (mm)	105
Fan Backplate Diameter (mm)	65
Fan Hub Diameter (mm)	17
Number of Fan Blades	8
Fan Blade Thickness (mm)	2
Fan Blade length (mm)	44

The fan rotates at a speed equal to the speed of the rotor and provides a forced air flow that intensifies the heat transfer outside the housing [72]. However, the inlet air velocity to the fin channels must be estimated [109]. In a typical TEFC motor, the controller's bolt lugs and terminal wire connections block some fin channels. Furthermore, air leaks from open channels produce local air velocity at distances from the fan end. The exact estimation of velocity reduction is a complex function that includes fan, fin, cowling design, and rotational speed. In this work, computational Fluid Dynamics (CFD) estimates air velocity over the motor length. The simulation results are shown in Figure 6.2 shows the streamline resulting from the CFD simulation in Ansys Fluent at 3000 rpm speed.

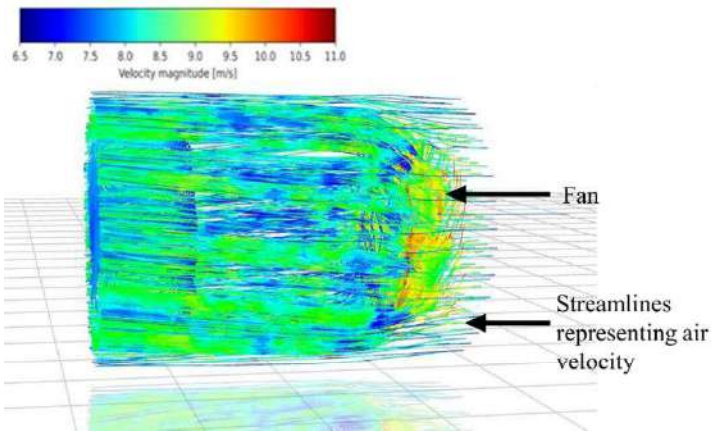

Figure 6.2: Stream line from air velocity from the fan

Figure 6.3 shows the fan air velocity variation over the motor's axial length where the ambient temperature is 40 degrees Celsius and the fan's rotational speed is 3000 rpm.

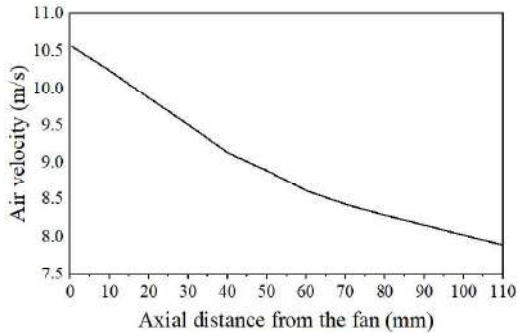

Figure 6.3: Fan air velocity variation over motor axial length

As can be seen, the maximum air velocity at the fan end is 10.54 m/s, while at the opposite end is 7.88 m/s. There have been approximately 25% decreases in fan air velocity over the motor's axial lengths. Another way to measure the air velocity at the fan end is considering that it is approximately 75% of the peripheral fan speed, as suggested in [75]. Following this assumption, the air velocity (V_{fa}) at the motor fan end can be calculated with equation 60.

$$V_{fa} = 0.75\omega_f R_{fb} \tag{60}$$

Where ω_f is fan speed and R_{fb} is the length of the fan blade. The calculated air velocity is 10.367 m/s at 3000 rpm motor shaft speed which is very close to the value received from the CFD simulation. As can be seen from equation 60, the air velocity changes with the shaft speed since the fan rotates at the same velocity as the shaft. The air velocities at the fan end for different motor speeds are shown in Figure 6.4.

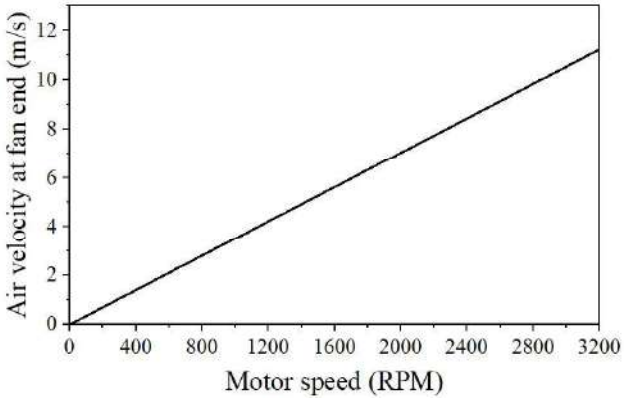

Figure 6.4: Relation between motor shaft speed and fan end air velocity

6.2 Winding Arrangement and Interfaces

The heat is mainly transferred by conduction from the stator/winding assembly [72]. The accuracy of a motor's thermal performance prediction depends upon estimating the many thermal contact resistances within the machine. Among them two most important are gaps between stator lamination to housing and slot-liner to lamination [60]. The distance between stator lamination and housing is determined by how effectively the stator's rough laminated outer surface is prepared prior to housing installation. The motor housing is made typically made from aluminium. The suggested average interface gap between lamination and housing is 0.037 mm in [109], which is chosen in this work. Because of the flexibility of the liner, determining the gap between the slot liner and laminate is more complex and difficult than determining other interface gaps in the machine. The contact between the liner and the laminate at the interface can be improved during the design and production stages [61]. In this work, the interface gap between the slot liner and the stator lamination is considered as 0.03 mm, and the slot liner thickness is selected 0.3 mm, as used in [61]. Since there are 7 turns and each turn has 16 strands, for the designed double-layer winding motor, there are 224 conductors. The conductor arrangement is considered stacked, and the minimum separation distance between conductors is considered 0.015 mm. Figure 6.5 shows the winding configuration considered for thermal simulation.

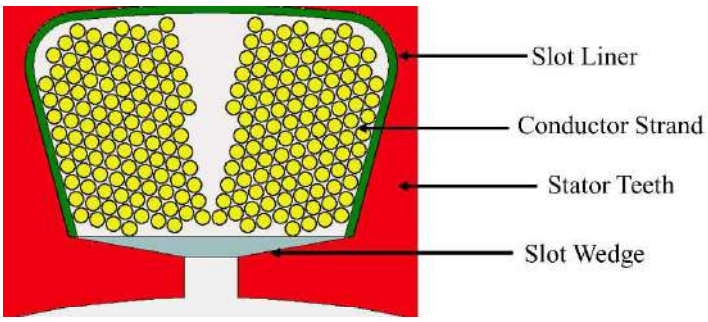

Figure 6.5: Motor Slot winding conductor arrangement

6.3 Thermal Analysis at the Rated Condition

To perform the thermal simulation at the rated condition, the losses at the rated speed and torque are added as input. From Ansys Maxwell, the total core loss can be found. However, for thermal analysis, it is required to specify the core loss distribution among

stator teeth, stator yoke, and rotor yoke. With the motor parameters determined after finite element simulation, the electromagnetic simulation is performed in MotorCAD. Table 6.2 shows the core loss distribution among different motor components.

Table 6.2: Core loss distribution among different motor components.

Motor Components	Core Loss Components (Watt)	Percentage (%)
Stator yoke	14.95	36.33
Stator teeth	25.34	61.59
Rotor yoke	0.8552	2.08
Total	41.1452	100

The core loss calculated from Ansys Maxwell is 41.1272 Watt which is very close to the value calculated from MotorCAD. Therefore, this core loss distribution percentage is considered for the thermal analysis of the PM-BLDC motor. The mechanical loss has been estimated based on 1% of motor output power. The FE solvers cannot calculate the mechanical losses, and so external input is required. The mechanical losses in MotorCAD are divided into two types. They are bearing loss and windage loss. It is assumed that 70% of total mechanical loss is due to both bearings (front and rear) and 20% is due to windage because of air friction, and 10% is external fan loss. Table 6.3 shows the loss distribution among different motor components.

Table 6.3: Total loss distribution among different motor components.

Loss Components	Value (Watt)
Stator Copper loss	35.03
Stator yoke loss	14.95
Stator tooth loss	25.34
Magnet loss	6.26
Rotor yoke loss	0.8552
Friction- front bearing	3.54
Friction- rare bearing	3.54
Windage loss	2.023
Fan loss	1.011
Total loss	92.55

Transient simulation is performed at the rated speed (3000 rpm) and with the losses in the rated condition in motor CAD with a duration of 20000 seconds. The ambient temperature is considered 40ºC in all the simulations. From Transient thermal simulation, different motor component temperatures can be determined. Figure 6.6 shows motor winding temperatures (hotspot, average and cool spot) resulting from the transient thermal simulation.

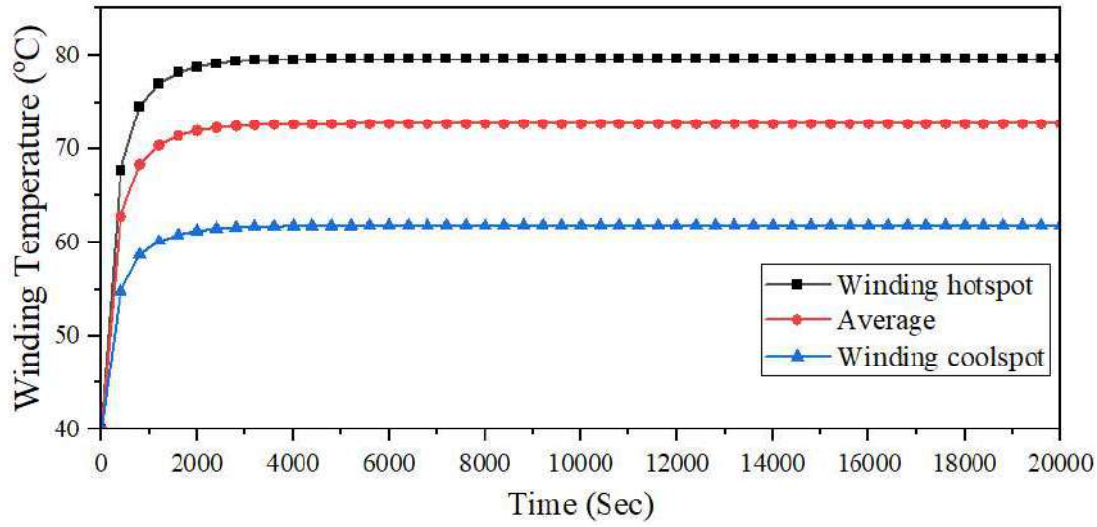

Figure 6.6: Winding Temperature at the rated condition

Other important motor components such as motor housing, shaft and magnet temperature are shown in Figure 6.7.

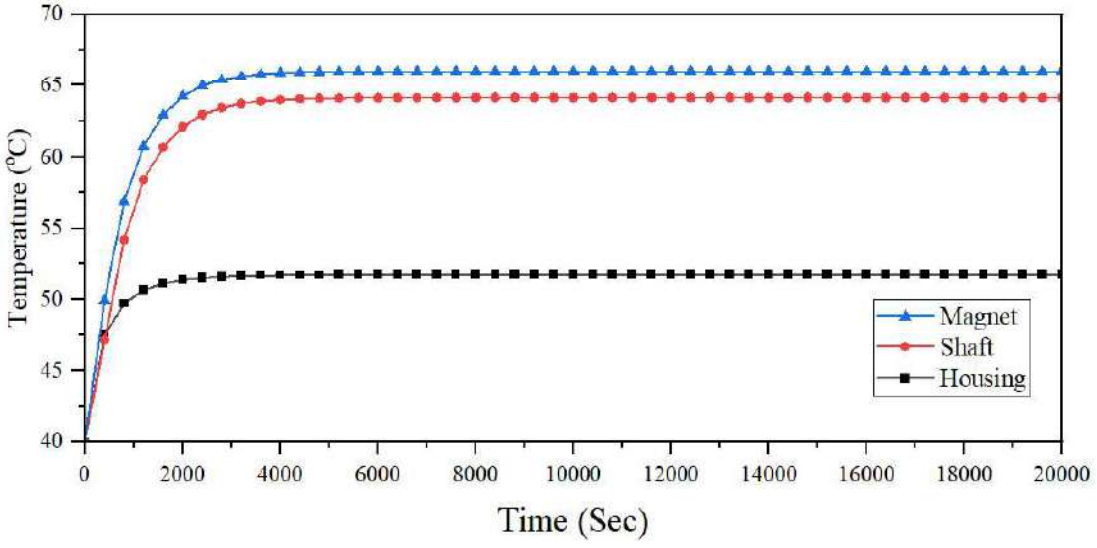

Figure 6.7: Motor Housing, shaft and magnet temperature

The steady state temperature of different motor components is listed in table 6.4.

Table 6.4: Steady state temperature of motor components at rated condition

Motor Component	Temperature (Degree Celsius)
Winding hotspot	79.64
Winding cool spot	61.86
Winding average	72.68
Stator tooth	59.12
Magnet	66.04
Rotor yoke	65.50
Bearing	56.81
Shaft	64.10
Stator yoke	57.91
Housing	51.73

Figures 6.8 and 6.9 show the radial and the axial view of the motor temperature distribution after the transient simulation duration at the rated condition, respectively, and Figure 6.10 shows the equivalent thermal network of the designed motor.

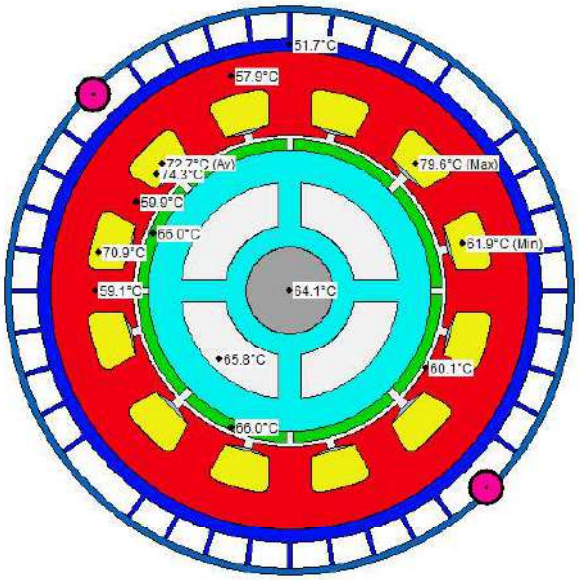

Figure 6.8: Radial view of motor temperature distribution at rated condition

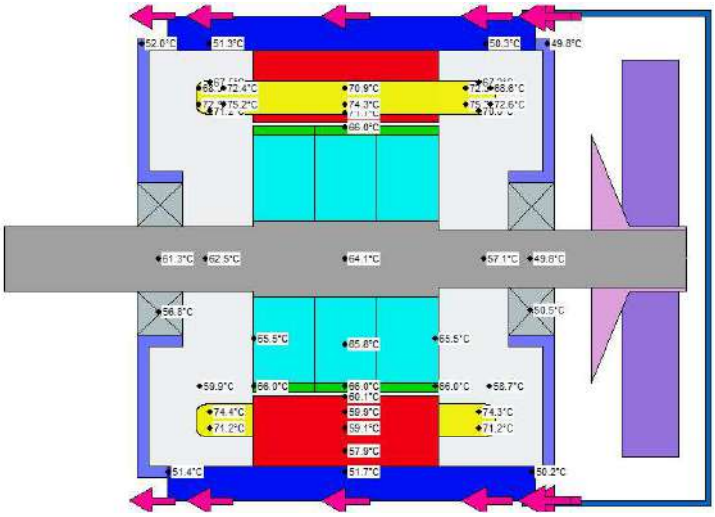

Figure 6.9: Axial view of motor temperature distribution at rated condition

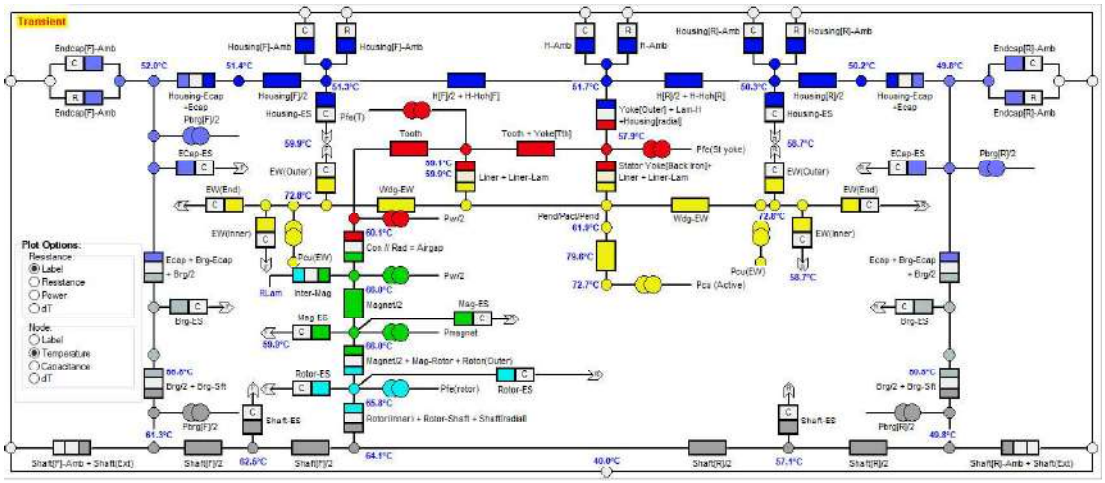

Figure 6.10: Equivalent thermal network of the designed motor at rated condition

6.4 Temperature over Different Torque-Speed Points

The transient thermal simulation is repeated for various torque and speeds to assess the thermal feasibility of the motor. The major motor parameters selected are winding hotspot, winding average, magnet, and housing temperature. The selected torque values are 4.5Nm, 5Nm, and 5.5Nm. As mentioned in section 3.3, the peak torque selected is 10 Nm, and its half value of 5 Nm is considered as continuous torque. Motor winding insulation is a significant design factor, and its insulation class can be selected based on continuous motor operational region. Therefore, selecting 4.5Nm, 5Nm, and 5.5Nm for the thermal simulation is a way to measure the thermal feasibility for the

selection of peak torque 9 Nm, 10Nm, and 11 Nm, respectively. Figure 6.11 and 6.12 shows the maximum temperature of the winding hotspot and average winding temperature, respectively, for different motor torque and speed level considering the continual operation for 20,000 seconds (5.56 hrs).

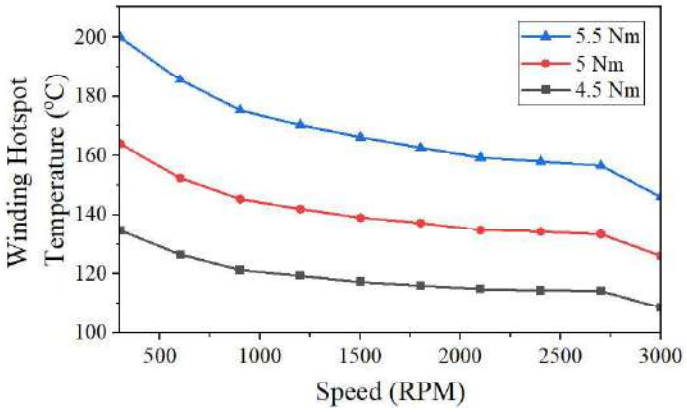

Figure 6.11: Winding hotspot temperature for different torque and speed values

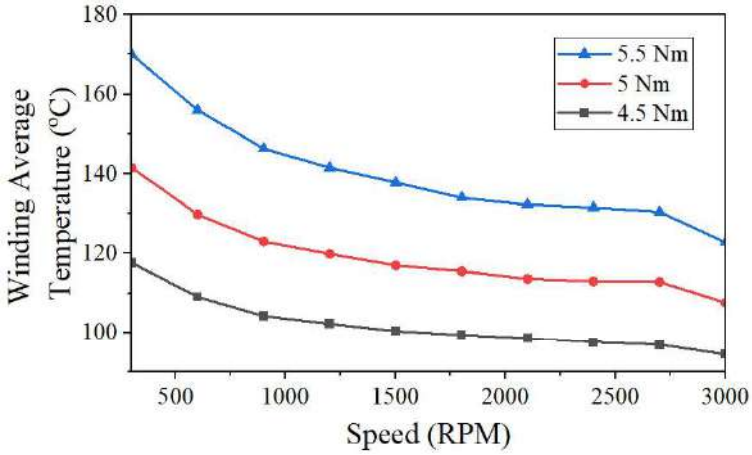

Figure 6.12: Winding average temperature for different torque and speed values

In the case of winding hotspot temperature for a higher torque value, the temperature decreases with increasing motor speed, indicating that motor cooling performance improves with increasing motor speed due to the shaft-mounted fan despite the increase of motor power output. Such characteristics are not observable in lower values of torque. In the case of average winding temperature, this parameter at first decreases with increasing motor speed and later increases, highlighting the increase of motor power with increasing speed and corresponding winding copper loss.

The motor operates with higher torque values for a few seconds, mainly for acceleration or during vehicle travels over high up-hill paths. For such durations, the temperature increase is not abrupt. Therefore, the selection of winding insulation is made considering the continuous torque operating region [63]. Class F insulation can be adopted for continuous torque region peak torque of 5 Nm, which has a temperature limit of around 155°C [110]. Although at a lower motor speed below 600 rpm, for continual running at those speeds, the hotspot temperature may be higher than the insulation temperature limit; however, in practical operation, the motor runs over such small speed most of the time, and winding insulation can sustain over its thermal limit to some extent. The motor moves towards a higher speed before the hotspot temperature crosses the insulation limit. Higher class insulation is required to go over the peak value and continuous operation. For the selection of the ceiling torque 5.5 Nm for continuous operation, the motor operates mainly over 155°C, and therefore, class H insulation should be chosen whose limit is 180°C. For 4.5 Nm continuous motor torque operation, the motor operates below 135°C; hence for the selection of peak torque of 9 Nm, class B insulation can be selected whose limit is 135°C. In this work, insulation class F is considered for the designed motor since 5 Nm torque is selected as the limit of continuous motor operation. Figure 6.13 shows the temperature of the magnet for different motor torque values over different motor speed.

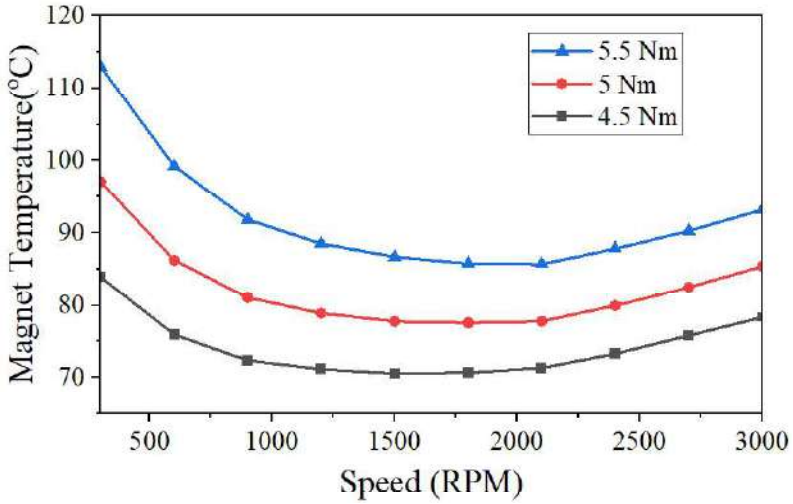

Figure 6.13: Magnet temperature for different motor torque-speed values

In this work, the chosen magnet is Magnets N42SH. The temperature limit is 150°C[111]. The magnet temperature at high torque values at low speed displays

higher temperature, which decreases with increasing speed at first due to motor cooling improvement. However, with a further increase of speed for high torque and an increase of speed for lower torque value, the magnet temperature increases since the eddy effect is dominant at higher motor speed; as can be seen, the permanent magnet temperature remains lower than the temperature limit of 150°C. Therefore, the permanent magnet is safe from demagnetization during continuous stable motor operation, even for higher torque values. Figure 6.14 shows the steady state temperature of motor housing for different motor torque values over different motor speeds.

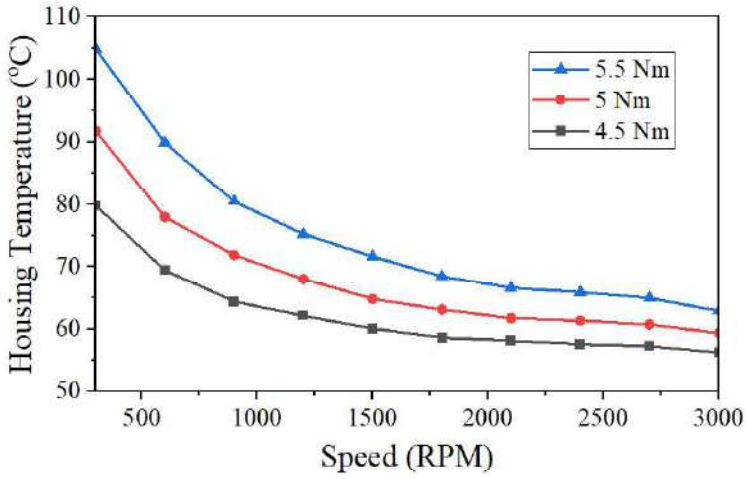

Figure 6.14: Motor housing temperature for different motor torque-speed values

Figures 6.11 to 6.14 show that the motor's thermal characteristics improve with motor speed since the shaft-mounted cooling fan speed increases with increasing motor speed.

6.5 Thermal Analysis over Recorded Driving Profiles

The winding hotspot and average motor winding temperature can be observed from the transient duty cycle analysis. Here the duty cycles include the torque and speed data over the driving profiles presented in Chapter 3. For the simulation, the peak torque for motor action (positive torque) and braking action (negative torque) is kept at 10 Nm and -10 Nm, respectively. The winding temperatures for the three driving profiles are shown in Figure 6.15.

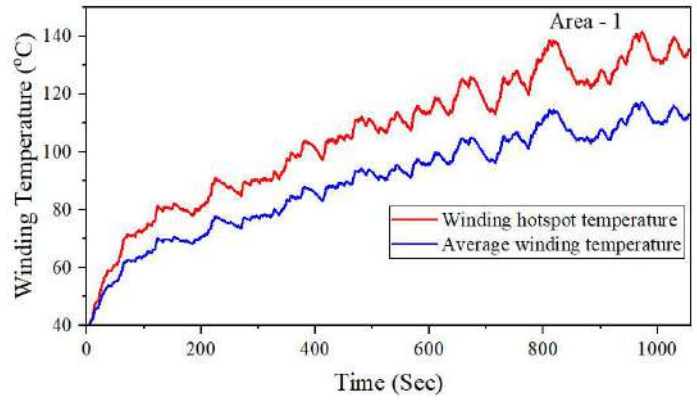

(a)

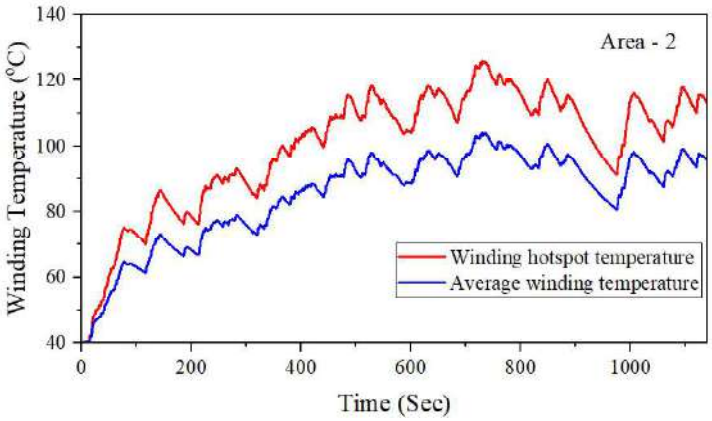

(b)

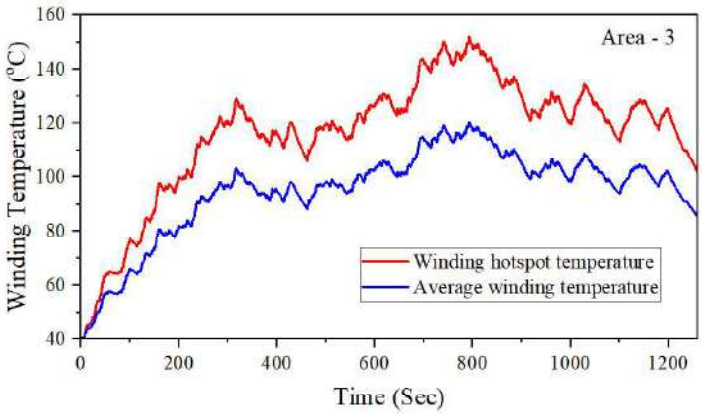

(c)

Figure 6.15: Transient Duty Cycle Simulation for driving profiles (a) Area-1 (b) Area-2 (c) Area-3

The observed maximum winding hotspot temperature for the areas 1, 2 and 3 are found 139°C,125°C and 152°C respectively. Therefore, class F insulation is appropriate for the designed PM-BLDC motor.

6.6 Summary

In this chapter, thermal analysis has been performed on the designed PM-BLDC motor based on lumped parameter model. The motor housing and cooling system has been designed based on commercially available PM-BLDC motors. Since the motor is a totally enclosed fan cooled motor with a fan mounted on the motor shaft, the motor's air velocity and flow characteristics have been determined using CFD analysis. The interface between stator lamination and housing has been appropriately defined. For winding setup, appropriate values are taken for slot liner- lamination gap, slot liner thickness, and minimum conductor distance. Other parameters used are standard parameters provided by the Motor-CAD model. At first, the thermal analysis is performed at the motor-rated condition. The temperatures of various motor components have been determined. A particular focus has been given to winding hotspots, average, magnet, and housing temperature. The process is repeated for different motor torque and speed values. It has been concluded that class F insulation is preferable for the motor with a continuous torque of 5 Nm and peak torque of 10 Nm. The magnets are observed to be within their thermal limit for high-torque operation. The thermal performance improves with higher motor speed since the shaft-mounted fan only performs the cooling. Transient duty cycle based thermal analysis is performed for the recorded driving profiles to observe the winding temperature. It has been found that the temperatures are within the class F insulation thermal limit.

Chapter 7: Comparison with commercial PM-BLDC motor

The rated speed, torque, current, voltage, and power factor of a commercial PM-BLDC motor must be known to compare the performance of the designed PM-BLDC motor. However, no published literature provided this information. Therefore, an experimental setup is needed to determine these parameters.

7.1: Experimental Setup

An experimental setup to measure different parameters of a commercial PM-BLDC motor is shown in Figure 7.1.

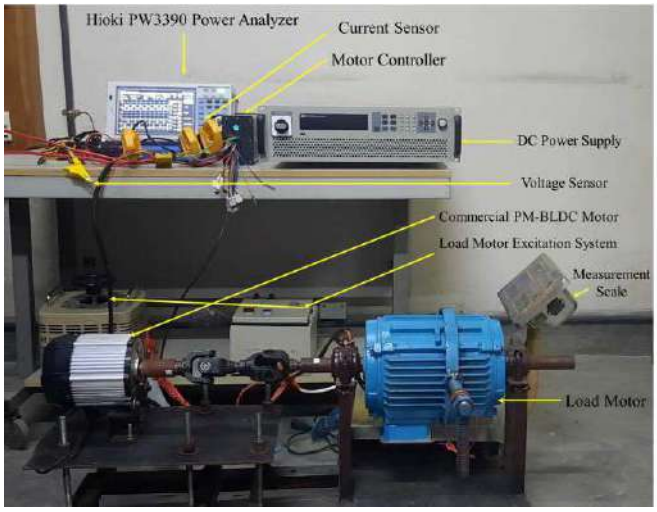

Figure 7.1: Experimental Setup

The experimental setup consists of following components.

- Hioki PW3390 Power Analyzer
- DC Power Supply
- Commercial PM-BLDC motor
- Load Motor with excitation system
- Measurement Scale

Hioki 3390 Power Analyzer is a powerful tool that enables accurate measurement, analysis, and evaluation of electrical power parameters. It provides precise

measurements for both single-phase and three-phase systems covering voltage, current, power (active, reactive, and apparent), energy consumption, power factor, and frequency[112, 113]. A Hioki 3390 Power Analyzer is shown in Figure 7.2.

(a) (b)

Figure 7.2: Hioki Power Analyzer (a) Front view (b) rear view

The DC power supply used in this work is ITECH IT 6000B Series Regenerative Power System. It offers a wide range of power ratings, from a few kilowatts to megawatts, making it suitable for various applications. It can provide voltages up to 2 kilovolts and 100 Ampere. Figure 7.3 shows the ITECH IT 6000B Series Regenerative Power System.

Fig 7.3: ITECH IT 6000B Series Regenerative Power System

To measure the torque of the commercial PM-BLDC motor, a cost-effective dynamometer system has been developed. A wound rotor induction motor has been used as the load motor. The motor is provided with DC excitation to increase the load, which works as the braking torque. Figure 7.4 shows the motor torque measurement arrangements.

Figure 7.4: Motor torque measuring arrangements

At no excitation, the PM-BLDC motor does not face any load, but by increasing the excitation, the motor load increases. An arm is attached to the motor housing. The load faced by the PM-BLDC motor is recorded in the measurement scale in mass. To determine the torque, the mass is multiplied by gravitational acceleration and length from the load motor shaft center to the arm end, as shown in equation (61).

$$T_{motor} = m_l g(l_a + r) \tag{61}$$

Where, m_l recorded load mass, l_a is the arm length and r is load motor radius from centre to housing surface. The total length from centre to arm end is measure 0.28 meter.

7.2: Result Analysis

The commercial C-E3W's PM-BLDC motor is a rated 1 KW motor. To measure the corresponding rated speed and rated torque, the motor speed and load motor excitation are increased sequentially until the maximum output power is 1 KW. The motor base speed, measured with a tachometer, is 3222 rpm. The recorded mass on the measurement scale is found to be 1.0804 kg. Using equation 55, the calculated motor torque is 2.9645 Nm. Therefore, the output power is calculated as 1000.24 watts, identical to motor-rated power. Figure 7.5 shows the experimental data of motor input power, phase current, phase voltage and power factor.

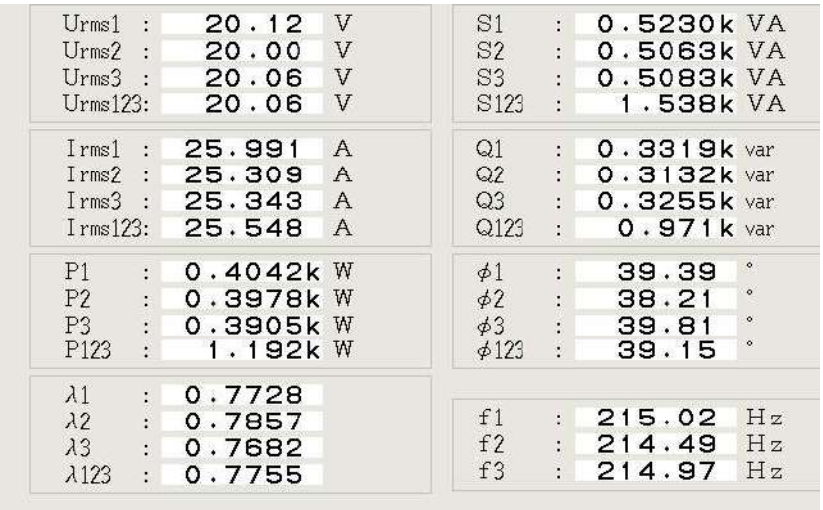

Figure 7.5: Commercial PM-BLDC motor rated input voltage, current, power and power factor.

The rated efficiency (η_c) of the commercial PM-BLDC motor can be calculated using equation 62.

$$\eta_c = \frac{P_{out,c}}{P_{in,c}} \tag{62}$$

The motor input power $P_{in,c}$ is 1192 Watt and $P_{out,c}$ is 1000.24 Watt. Following equation 56, the calculated motor efficiency is 83.9 %. Figure 7.6 shows the three-phase voltage and current waveforms of the commercial PM BLDC motor.

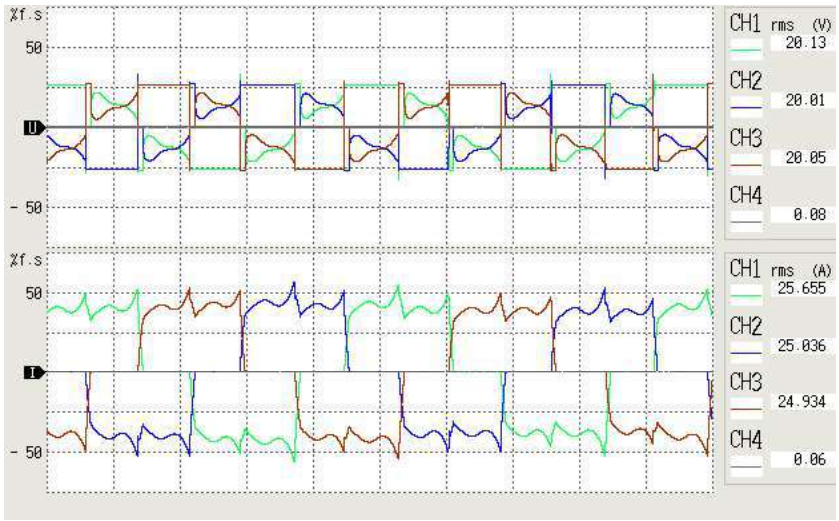

Figure 7.6: Three phase voltage and current waveform of a commercial PM-BLDC motor

7.3: Comparison

A comparison of the designed PM-BLDC motor and the commercial PM-BLDC motor is presented in Table 7.1.

Table 7.1: Electrical parameter comparison

Parameter	Commercial motor	Designed motor
RMS phase Voltage (Volt)	20.06	19.9517
RMS phase Current (Ampere)	25.548	21.194
Power Factor	0.7755	0.8615
Rated Speed (rpm)	3222	3000
Rated Torque (Nm)	2.9645	3.184
Input Power (Watt)	1192	1092.93
Loss (Watt)	191.8	92.53
Efficiency (%)	83.9	91.53

From Table 7.1, it can be seen that the designed PM-BLDC motor has higher efficiency and higher power factor compared to the commercial motor. The commercial motor has a higher rated speed, but the designed motor has a higher-rated torque. Although the prototype manufacturing of the designed PM-BLDC motor may result in lower efficiency than the simulation model, the high difference in efficiency between the designed and commercial motor indicates that the prototype manufactured designed PM-BLDC motor should perform better than the commercial motor.

Table 7.2: Physical parameter comparison

Parameter	Commercial motor	Designed motor
Weight (Kg)	4.7	4
Motor total diameter (mm)	125	116
Motor Length (including cowling) (mm)	150	130

From Table 7.2, it can be seen that the designed PM-BLDC motor is smaller in size and lighter than the commercial PM-BLDC motor.

7.4: Summary

This chapter presents an experimental setup for a commercial PM-BLDC motor parameter measurement. The different components of the experimental setup, such as the Hioki 3390 power analyser, load motor, torque measurement system, and DC power supply, have been briefly described. The torque measurement process has been explored. The tested, rated parameters of the commercial PM-BLDC motor are measured and presented. Finally, these values are compared with the designed PM-BLDC motor. The analysis shows that the PM-BLDC motor performs better than the commercial motor in terms of efficiency and power factor.

Chapter 8: Conclusion and Recommendation for Future Research

In this chapter, the key findings of the thesis are summarized, and some insights on future research are presented.

8.1 Conclusion

The electric traction motor requires special attention to integrate the C-E3Ws into public transportation properly. A thorough systematic analysis is required for its most used permanent magnet brushless DC motor, which is missing in the published literature. This work has intended to cover the research gap by including driving profile analysis, electromagnetic design, and thermal analysis of a 1 KW PM-BLDC motor. From the driving profile analysis, it can be seen that the traction motor's maximum speed is below 3000 RPM, and 95% of the required motor torque value is within 10 Nm. Therefore, the motor's peak torque is chosen as 10 Nm, and continuous torque is chosen as 5 Nm. An analytical equation-based sizing has been implemented to provide an initial motor structure for finite element analysis for specific design goals, including output power, torque, speed, and minimum efficiency. A 2D finite element-based electromagnetic model of the motor has been developed with a rated speed of 3000 rpm and rated torque of 3.184 Nm. The magnet dimensions and motor stack length have been optimized to achieve design goals. The designed motor has an efficiency of 91.53% and a power factor of 0.8615, higher than the commercial C-E3W PM BLDC motor. From the lumped parameter-based thermal model analysis, it is concluded that the stator winding insulation should be class F for continuous torque of 5 Nm and peak torque of 10 Nm. For higher continuous torque and peak torque higher insulation level is required. The temperature chosen magnet Neodymium Ferrus Boron (NdFeB) remains lower than its thermal limit for chosen continuous torque of 5Nm. Though the prototype manufacturing of the designed PM-BLDC motor may result in lower efficiency than the simulation model, the high difference in efficiency between the designed and commercial motor indicates that the prototype manufactured designed motor should perform better than the commercial motor.

8.2 Recommendations for Future Works

Here, some scopes to expand this research have been recommended for fellow researchers and engineers. PM-BLDC motors with different power and voltage levels can be explored for the C-E3Ws. Moreover, the choice of different lamination materials and magnets, magnets orientation and slot designs, and their comparative analysis can be suitable scopes for research. Different types of motors can be studied to find their feasibility and suitability for the C-E3Ws vehicles. The analysis process presented in this work can be fully or partially applied to different types of motors, such as permanent magnet synchronous motors, switched reluctance motors, etc. The research methodology in this thesis can be extended to large E3Ws such as Easy Bikes. Since the Easy Bikes operate in the village and sub-urban sides, their driving profiles are more diverse than that of C-E3Ws. Developing a standard E3W drive cycle can be a suitable scope for research. Different optimization algorithms can be explored for C-E3W's motor sizing, where a wide range of geometric and electromagnetic design variables can be considered. Genetic algorithm, particle swarm algorithm, etc., are some well-known optimization algorithms. A PM-BLDC motor controller can be designed and developed, and a co-simulation can be performed with the finite element solver. Different control strategies can be adopted to study their impact on motor performance. For the six-step drive motor controller, the optimum firing angle of the switches can be determined for better motor performance. A techno-economic analysis can also be performed for different motor controllers for the traction motor of the C-E3Ws. Different types of cooling methods can be explored for the PM-BLDC motor. The proper housing design, manufacturing methods to ensure effective interface gap, etc., can be a scope for research for the C-E3W's motors.

References

[1] A. M. Saleque, A. M. A. Khan, S. H. Khan, and S. Hoque, "Drivetrain Design and Feasibility Analysis of Electric Three-Wheeler Powered by Renewable Energy Sources," *4th International Conference on Advances in Electrical Engineering (ICAEE),* pp. 432-438, 2017.

[2] S. N. Saxena, "Two- and Three-Wheeler Electric Vehicles in India – Outlook 2019," *International Journal of Electrical Engineering and Technology,* vol. 9, pp. 1-13, 2019.

[3] B. Hanke *et al.*, "Interdependence of charging infrastructure and battery demand of light electric 3-wheel motor taxis," presented at the Fifteenth International Conference on Ecological Vehicles and Renewable Energies (EVER), Monte-Carlo, Monaco, 10-12 September 2020, 2020

[4] Z. Y. Huong Le, "Market analysis of two- and three-wheeler vehicles in key ASEAN member states," International Council On Clean Transportation2022 Available: https://theicct.org/publication/asia-pacific-lvs-ndc-tia-23w-market-asean-countries-jun22/.

[5] M. J. A. Hossain, M. Z. Hasan, M. Hasanuzzaman, M. Z. R. Khan, and M. Ahsan Habib, "Affordable Electric Three-Wheeler in Bangladesh: Prospects, Challenges, and Sustainable Solutions," *Sustainability,* vol. 15, no. 1, 2022.

[6] S. R and K. R. Rajagopa, "An Insight into Motor and Battery Selections for Three-Wheeler Electric Vehicle," *1s IEEE International Conference on Power Electronics. Intelligent Control and Energy Systems (ICPEICES-2016),* pp. pp 1-6, 2016.

[7] M. R. Wahid, B. A. Budiman, E. Joelianto, and M. Aziz, "A Review on Drive Train Technologies for Passenger Electric Vehicles," *Energies,* vol. 14, no. 20, 2021.

[8] M. N. Y. Yoga Uta Nugraha, Herviyandi Herizal,Dimas Anton Asfani,Dedet Candra Riawan,Mochammad Wahyudi, "Design Analysis of Axial Flux Permanent Magnet BLDC Motor 5 kW for Electric Scooter Application," presented at the International Seminar on Intelligent Technology and Its Applications (ISITIA), Bali, Indonesia, 2018

[9] C. K. C. Sandeep Kumar Chawrasia, Sumit Banerjee, "Design and Analysis of In-Wheel Motor for an Electric Vehicle," in *IEEE Calcutta Conference (CALCON)*, Kolkata, India, 2020.

[10] M. E. Mehmet Akar, Fazilet Akin, , "BLDC Motor Design and Application for Light Electric Vehicle," *Afyon Kocatepe University Journal of Sciences and Engineering,* 2021.

[11] G. T. O. Ustun, O.C. Kivanc, G. Tosun, "In Pursuit of Proper BLDC Motor Design for Electric Bicycles," presented at the XXII International Conference on Electrical Machines (ICEM), Lausanne, Switzerland, 04-07 September 2016, 2016.

[12] S. K. Tummala, V. Sandeep, S. Shastri, and P. B. Bobba, "Analysis and Design of PMBLDC Motor for Three Wheeler Electric Vehicle Application," *E3S Web of Conferences,* vol. 87, 2019.

[13] L. Berzi, M. Delogu, and M. Pierini, "Development of driving cycles for electric vehicles in the context of the city of Florence," *Transportation Research Part D: Transport and Environment,* vol. 47, pp. 299-322, 2016.

[14] Z. Sun, Z. Wen, X. Zhao, Y. Yang, and S. Li, "Real-World Driving Cycles Adaptability of Electric Vehicles," *World Electric Vehicle Journal,* vol. 11, no. 1, 2020.
[15] P. K. Prathibha and E. R. Samuel, "Performance Analysis of Electric Car Based on Drag Coefficients and Road Angles," presented at the 2022 2nd International Conference on Power Electronics & IoT Applications in Renewable Energy and its Control (PARC), 2022.
[16] L. Chen, W. Jiabin, P. Lazari, and X. Chen, "Optimizations of a Permanent Magnet Machine Targeting Different Driving Cycles for Electric Vehicles," presented at the International Electric Machines & Drives Conference, Chicago, IL, USA, 2013 Available: 10.1109/IEMDC.2013.6556198
[17] S. D. Vidhya and M. Balaji, "Modelling, design and control of a light electric vehicle with hybrid energy storage system for Indian driving cycle," *Measurement and Control,* vol. 52, no. 9-10, pp. 1420-1433, 2019.
[18] D. C. Hanselman, *Brushless Permanent Magnet Motor Design*, 2nd ed. 2003.
[19] V. Madonna, P. Giangrande, L. Lusuardi, A. Cavallini, C. Gerada, and M. Galea, "Thermal Overload and Insulation Aging of Short Duty Cycle, Aerospace Motors," *IEEE Transactions on Industrial Electronics,* vol. 67, no. 4, pp. 2618-2629, 2020.
[20] J. Fan *et al.*, "Thermal Analysis of Permanent Magnet Motor for the Electric Vehicle Application Considering Driving Duty Cycle," *IEEE Transactions on Magnetics,* vol. 46, no. 6, pp. 2493-2496, 2010.
[21] P. S. Bokare and A. K. Maurya, "Study of Acceleration Behaviour of Motorized Three Wheeler in India," *Transportation Research Procedia,* vol. 17, pp. 244-252, 2016.
[22] M. R. Awal, M. M. Rahman, A. K. M. N. Islam, J. Al-Hossain, and M. Z. R. Khan, "Energy Consumption Analysis of Electric Three Wheelers in Bangladesh," presented at the IEEE International Conference on Power, Electrical, and Electronics and Industrial Applications (PEEIACON) Dhaka, Bangladesh., 29 November - 01 December, 2019
[23] M. R. Awal, A. K. M. N. Islam , and M. Z. R. Khan, "Bangladesh Power System Peak Demand Shaving through Demand Side Management of the Battery Operated Easy Bike Load," *4th International Conference on Electrical Information and Communication Technology (EICT),* pp. pp. 1-6, 2019.
[24] M. M. Rahman and M. Z. R. Khan, "Solar Energy based Net Metered Easy-Bike Charging Station in Bangladesh," *International Conference on Information and Communication Technology for Sustainable Development (ICICT4SD),* pp. pp. 220-224, 2021
[25] P. Mulhall, S. M. Lukic, S. G. Wirasingha, L. Young-Joo, and A. Emadi, "Solar-Assisted Electric Auto Rickshaw Three-Wheeler," *IEEE Transactions on Vehicular Technology,* vol. 59, no. 5, pp. 2298-2307, 2010.
[26] P. Mulhall and A. Emadi, "Comprehensive Simulations and Comparative Analysis of the Electric Propulsion Motor for a Solar/Battery Electric Auto Rickshaw Three-Wheeler," *35th Annual Conference of the IEEE Industrial Electronics Society,* pp. pp. 3785-3790, 2009.
[27] F. Arifurrahman, I. Indrawanto, B. A. Budiman, P. L. Sambegoro, and S. P. Santosa, "Frame modal analysis for an electric three-wheel vehicle," *MATEC Web of Conferences,* vol. 197, pp. pp. 08001-08006, 2018.

[28] G. T. O. Ustun, O.C. Kivanc and G. Tosun, "In Pursuit of Proper BLDC Motor Design for Electric Bicycles," *2016 XXII International Conference on Electrical Machines (ICEM),* 2016.

[29] D. I. Azira Adnan, "Finite Element Modeling and Analysis of External Rotor Brushless DC Motor for Electric Bicycle," presented at the JFFF Student Conference on Research and Development, UPM Serdang, Malaysia, 16-18 Nov, 2009

[30] C. K. C. Sandeep Kumar Chawrasia, Sumit Banerjee, "Design and Analysis of In-Wheel Motor for an Electric Vehicle," in *IEEE Calcutta Conference (CALCON)*, Kolkata, India, 2020.

[31] A. B. Nishtha Shrivastava, "Design of 3-Phase BLDC Motor for Electric Vehicle Application by Using Finite Element Simulation," *International Journal of Emerging Technology and Advanced Engineering,* vol. 4, no. 1, January 2014.

[32] S. A. E Elakkia , R Girish Ganesan, S Saikiran, "Design And Modelling of Bldc Motor For Automotive applications," *International Journal of Electrical and Electronic Engineering and Telecommunication,* vol. 1, no. 1, pp. 42-48, March 2015.

[33] P. S. M. Mr. Vipin Kumar Singh, Mr. Ashish Kumar Singh, "Design and Analysis of Permanent Magnet Brushless DC Motor for Solar Vehicle using Ansys Software," *International Journal of Engineering Research & Technology (IJERT),* vol. 6, no. 4, April 2017.

[34] N. Murali, S. Ushakumari, M. V.P, and A. T. Varghesee, "Sizing and Performance Analysis of an Electric Motor in an E-rickshaw," presented at the IEEE International Conference on Power Systems Technology (POWERCON), Bangalore, India, 2020.

[35] P. Mukherjee and M. Sengupta, "Design, analysis and fabrication of a brush-less DC motor," presented at the 2014 IEEE International Conference on Power Electronics, Drives and Energy Systems (PEDES), 2014.

[36] P. Mukherjee, S. Paitandi, and M. Sengupta, "Comparative analytical and experimental study of fabricated identical surface and interior permanent magnet BLDC motor prototypes," *Sadhana,* vol. 45, no. 1, pp. 1-24, 2020, Art. no. 26.

[37] S. Shastri, U. Sharma, and B. Singh, "Design and Analysis of Brushless DC Motors for Ceiling Fan Application," presented at the 2020 IEEE International Conference on Power Electronics, Drives and Energy Systems (PEDES), 2020.

[38] "Guidelines for Designing Concentrated Winding Fractional Slot Permanent Magnet Machines."

[39] R. R. Patrick Xie, Gaurang Vakil, Chris Gerada, "Simplified Analytical Machine Sizing for Surface Mounted Permanent Magnet Machines," presented at the IEEE International Electric Machines & Drives Conference (IEMDC), San Diego, CA, USA, 12-15 May 2019, 2019

[40] A. Kumar, R. Gandhi, R. Wilson, and R. Roy, "Analysis of Permanent Magnet BLDC Motor Design with Different Slot Type," presented at the IEEE International Conference on Power Electronics, Smart Grid and Renewable Energy (PESGRE), Cochin, India, 2020.

[41] Y. K. Tomonobu Senjyu, Naomitsu Urasaki, Katsumi Uezato, "Accurate Parameter Measurement for High Speed Permanent Magnet Synchronous

Motors," presented at the IEEE 32nd Annual Power Electronics Specialists Conference, Vancouver, BC, Canada, 17-21 June, 2001
[42] J. D. Uldis Brakanskis, Ludmila Kukjane, Viesturs Drava, "Analysis of a Permanent - Magnet Brushless DC Motor with Fixed Dimensions," *Scientific Journal of Riga Technical University,* vol. 27, 2010.
[43] J. Chen, Y. Guo, and J. Zhu, "Development of a High-Speed Permanent-Magnet Brushless DC Motor for Driving Embroidery Machines," *IEEE Transactions on Magnetics,* vol. 43, no. 11, pp. 4004-4009, 2007.
[44] S. Cho, J. Hwang, and C.-W. Kim, "A Study on Vibration Characteristics of Brushless DC Motor by Electromagnetic-Structural Coupled Analysis Using Entire Finite Element Model," *IEEE Transactions on Energy Conversion,* vol. 33, no. 4, pp. 1712-1718, 2018.
[45] M. I. Ansari and H. Misra, "Power Management Strategy Considering the Mountainous Terrain Driving Pattern for Three Wheeler Electric Vehicle," presented at the 2022 IEEE International Conference on Power Electronics, Smart Grid, and Renewable Energy (PESGRE), 2022.
[46] S.-H. R. Young-kyoun Kim, In-Soung Jung, "Parameter Determination of the BLDC Motor considering the Dynamic Equation of Vehicle," *XIX International Conference on Electrical Machines - ICEM,* 2010.
[47] M. J. A. H. Hossain, Md. Zakir; Khan, Md. Ziaur Rahman, "Analysis of Traction Power of Electric Three Wheelers in Bangladesh," presented at the 12th International Conference on Electrical and Computer Engineering (ICECE), Dhaka, Bangladesh, 2022
[48] K.-Y. Yoon and S.-W. Baek, "Robust Design Optimization with Penalty Function for Electric Oil Pumps with BLDC Motors," *Energies,* vol. 12, no. 1, 2019.
[49] C.-L. Chiu, Y.-T. Chen, Y.-L. Liang, and R.-H. Liang, "Optimal Driving Efficiency Design for the Single-Phase Brushless DC Fan Motor," *IEEE Transactions on Magnetics,* vol. 46, no. 4, pp. 1123-1130, 2010.
[50] D. C. S. S. S.Rajkumar, Dr.K.Sedhuraman, D.Muruganandhan, "Performance Analysis Of Hub Bldc Motor Using Finite Element Analysis," presented at the International Conference on Systems Computation Automation and Networking, Pondicherry, India, 29-30 March 2019, 2019.
[51] C. O. Ali Saygın, Adem Dalcalı, Emre Çelik, "Optimum Rotor Design Of Small PM Bldc Motor Based On High Efficiency Criteria," *ARPN Journal of Engineering and Applied Sciences,* vol. 10, no. 19, October 2015.
[52] S. Bentouati, Z. Q. Zhu, and D. Howe, "Influence of Design Parameters on the Starting Torque of a Single-Phase PM Brushless DC Motor," *IEEE Transactions On Magnetics,* vol. 36, no. 5, pp. 3533 - 3536, September 2000.
[53] G. H. Jang, J. H. Chang, D. P. Hong, and K. S. Kim, "Finite-Element Analysis of an Electromechanical Field of a BLDC Motor Considering Speed Control and Mechanical Flexibility," *IEEE Transactions On Magnetics,* vol. 38, no. 2, March 2002.
[54] M. Khelifa, M. Mordjaoui, and A. Medoued, "An inverse problem methodology for design and optimization of an interior permanent magnetic BLDC motor," *International Journal of Hydrogen Energy,* vol. 42, no. 28, pp. 17733-17740, 2017.

[55] A. K. Min Dai, Tomy Sebastian, "Torque Ripple Analysis of A Permanent Magnet Brushless DC Motor Using Finite Element Method," presented at the IEEE International Electric Machines and Drives Conference (IEMDC), Cambridge, MA, USA, 17-20 June, 2001.

[56] M. S. Islam, S. Mir, and T. Sebastian, "Issues in Reducing the Cogging Torque of Mass-Produced Permanent-Magnet Brushless DC Motor," *IEEE Transactions on Industry Applications,* vol. 40, no. 3, pp. 813-820, 2004.

[57] M. K. Teeradej Srisiriwanna, "A Study of Cogging Torque Reduction Methods in Brushless DC Motor," presented at the 9th International Conference on Electrical Engineering/Electronics, Computer, Telecommunications and Information Technology, Phetchaburi, Thailand, 16-18 May, 2012

[58] O. Ocak and M. Aydin, "An Innovative Semi-FEA Based, Variable Magnet-Step-Skew to Minimize Cogging Torque and Torque Pulsations in Permanent Magnet Synchronous Motors," *IEEE Access,* vol. 8, pp. 210775-210783, 2020.

[59] D. A. Staton, "Thermal computer aided design-advancing the revolution in compact motors " presented at the IEEE International Electric Machines and Drives Conference (IEMDC), Cambridge, MA, USA, 2001.

[60] D. Š. Staton, L., "Induction Motors Thermal Analysis," vol. 51, no. 6, pp. 623-631, 2009.

[61] S. Y. W. Goh, J; Greenwood, D., "Thermal analysis for stator slot of permanent magnet machine," presented at the XII International Conference on Electrical Machines (ICEM), Lausanne, Switzerland, 2016.

[62] A. C. Boglietti, A;, Staton, D.A., "Thermal Analysis of TEFC Induction Motors," presented at the 38th IAS Annual Meeting on Conference Record of the Industry Applications Conference, Salt Lake City, UT, USA, 2003.

[63] M. D. Andrea, G. D. Domenico, D. Macera, L. D. Leonardo, and M. Villani, "Brushless DC Motor for Primary Flight Surface Actuator," presented at the International Conference on Electrical Machines (ICEM), Gothenburg, Sweden, 2020.

[64] D. A. Staton and A. Cavagnino, "Convection Heat Transfer and Flow Calculations Suitable for Electric Machines Thermal Models," *IEEE Transactions on Industrial Electronics,* vol. 55, no. 10, pp. 3509-3516, 2008.

[65] T. Abdullah, A. Afrah, and A. Mejbel, "Thermal analysis of a three-phase induction motor based on motor-CAD, flux2D, and matlab," *Indonesian Journal of Electrical Engineering and Computer Science,* vol. 15, no. 1, pp. 46-53, 2019.

[66] N. Zhao, Z. Q. Zhu, and W. Liu, "Rotor Eddy Current Loss Calculation and Thermal Analysis of Permanent Magnet Motor and Generator," *IEEE Transactions on Magnetics,* vol. 47, no. 10, pp. 4199-4202, 2011.

[67] A. Shukla and S. Payami, "Design and Thermal Network Modeling of BLDC Motor for Submersible Pump Application," presented at the 2020 IEEE International Conference on Power Electronics, Drives and Energy Systems (PEDES), 2020.

[68] B. Groschup, M. Nell, F. Pauli, and K. Hameyer, "Characteristic Thermal Parameters in Electric Motors: Comparison Between Induction- and Permanent Magnet Excited Machine," *IEEE Transactions on Energy Conversion,* vol. 36, no. 3, pp. 2239-2248, 2021.

[69] M. Roffi, F. J. T. E. Ferreira, and A. T. De Almeida, "Comparison of different cooling fan designs for electric motors," presented at the IEEE International Electric Machines and Drives Conference (IEMDC), Miami, FL, USA, 2017.
[70] A. Tikadar, N. Kumar, Y. Joshi, and S. Kumar, "Coupled Electro-Thermal Analysis of Permanent Magnet Synchronous Motor for Electric Vehicles," presented at the 19th IEEE Intersociety Conference on Thermal and Thermomechanical Phenomena in Electronic Systems (ITherm), Orlando, FL, USA, 2020.
[71] S. Mizuno, S. Noda, M. Matsushita, T. Koyama, and S. Shiraishi, "Development of a Totally Enclosed Fan-Cooled Traction Motor," *IEEE Transactions on Industry Applications,* vol. 49, no. 4, pp. 1508-1514, 2013.
[72] J. Wernik, "Investigation of Heat Loss from the Finned Housing of the Electric Motor of a Vacuum Pump," *Applied Sciences,* vol. 7, no. 12, 2017.
[73] S. Ulbrich, J. Kopte, and J. Proske, "Cooling Fin Optimization on a TEFC Electrical Machine Housing Using a 2-D Conjugate Heat Transfer Model," *IEEE Transactions on Industrial Electronics,* vol. 65, no. 2, pp. 1711-1718, 2018.
[74] P. Shams Ghahfarokhi *et al.*, "Determination of Heat Transfer Coefficient from Housing Surface of a Totally Enclosed Fan-Cooled Machine during Passive Cooling," *Machines,* vol. 9, no. 6, 2021.
[75] J. L. Romo and M. B. Adrián, "Prediction of internal temperature in three-phase induction motors with electronic speed control," *Electric Power Systems Research* vol. 45, no. 2, pp. 91-99, 1998.
[76] D. I. Deaconu, C. Ghiţă, A. I. Chirilă, V. Năvrăpescu, and M. Popescu, "Thermal study of induction machine using Motor-CAD," presented at the 3rd International Symposium on Electrical and Electronics Engineering (ISEEE), Galati, Romania, 2010.
[77] (January 1). *GPSLogger for Android*. Available: https://gpslogger.app/
[78] Y.-k. Kim, S.-H. Rhyu, and I.-S. Jung, "Parameter Determination of the BLDC Motor considering the Dynamic Equation of Vehicle," presented at the XIX International Conference on Electrical Machines - ICEM, Rome, Italy, 2010.
[79] A. L. Saleem, Nain ; Junjie, Hu "Modelling of an Electric Vehicle for Tractive Force Calculation Along With Factors Affecting the Total Tractive Power and Energy Demand," presented at the 3rd International Conference on Computing, Mathematics and Engineering Technologies (iCoMET), Sukkur, Pakistan, 2020.
[80] K. Sayed, A. Kassem, H. Saleeb, A. S. Alghamdi, and A. G. Abo-Khalil, "Energy-Saving of Battery Electric Vehicle Powertrain and Efficiency Improvement during Different Standard Driving Cycles," *Sustainability,* vol. 12, no. 24, 2020.
[81] M. Ehsani, Y. Gao, L. Stefano, and K. M. Ebrahimi, *Modern Electric, Hybrid Electric, and Fuel Cell Vehicles*, 3rd ed. Taylor and Francis Group, 2018.
[82] B. Noll, S. del Val, T. S. Schmidt, and B. Steffen, "Analyzing the competitiveness of low-carbon drive-technologies in road-freight: A total cost of ownership analysis in Europe," *Applied Energy,* vol. 306, 2022.
[83] Y. Lee and J. Kim, "Analysis of the Three-Phase Inverter Power Efficiency of a BLDC Motor Drive Using Conventional Six-Step and Inverted Pulsewidth

Modulation Driving Schemes," *Canadian Journal of Electrical and Computer Engineering,* vol. 42, no. 1, pp. 34-40, 2019.
[84] P. S. H. Jussila, M. Niemelä, J.Pyrhönen, "Guidelines for Designing Concentrated Winding Fractional Slot Permanent Magnet Machines," presented at the POWERENG, Setúbal, Portugal, April 12-14, 2007.
[85] A. Sawhney, *A Course In Electrical Machine Design*, Sixth ed. DhanpatRai and Co., 2006.
[86] I. HSM WIRE INTERNATIONAL, "Wire Gauge Chart," 2013, Available: https://www.scribd.com/document/365044303/SWG-AWG-TABLE.
[87] T. J. Juha Pyrhonen, Valeria Hrabovcova, *Design Of Rotating Electrical Machines*. John Wiley & Sons, Ltd, 2008.
[88] A. M. Technologies. (2021). *Sintered Neodymium-Iron-Boron Magnets*. Available: https://www.arnoldmagnetics.com/wp-content/uploads/2017/11/N42SH-151021.pdf
[89] Jordi-RogerRiba, "Analysis of formulas to calculate the AC resistance of different conductors' configurations," *Electric Power Systems Research,* vol. 127, pp. 93-100, 2015.
[90] J. N. Reddy, *Introduction to the finite element method*. McGraw-Hill Education, 2019.
[91] M. N. O. Sadiku, "A simple introduction to finite element analysis of electromagnetic problems," *IEEE Transactions on Education,* vol. 32, pp. 85-93, May 1989.
[92] S. J. Salon and J. D. Angelo, "Applications of the hybrid finite element-boundary element method in electromagnetics," *IEEE Transactions on Magnetics,* vol. 24, no. 1, pp. 80-85, Jan 1988.
[93] K.-J. Bathe, "Finite Element Method. Wiley Encyclopedia of Computer Science and Engineering " 2008.
[94] X. Liu and W. N. Fu, "A Dynamic Dual-Response-Surface Methodology for Optimal Design of a Permanent-Magnet Motor Using Finite-Element Method," *IEEE Transactions on Magnetics,* vol. 52, no. 3, pp. 1-4, 2016.
[95] A. M. N. A. R. H. W. Ping, "Axial-Flux Permanent-Magnet Motor Design for Electric Vehicle Direct Drive Using Sizing Equation and Finite Element Analysis," *Progress In Electromagnetics Research,* vol. 122, 2012.
[96] Y.-J. Z. Hang Zhang, "Preliminary Electromagnetic Design Expert System for Surface-mounted Permanent Magnet Brushless Machine," *Applied Mechanics and Materials,* vol. Vol. 742 pp. pp 464-469, 16-03-2015 2015.
[97] Z. Q. Zhu and D. Howe, "Influence of design parameters on cogging torque in permanent magnet machines," *IEEE Transactions on Energy Conversion,* vol. 15, no. 4, pp. 407-412, 2000.
[98] D. Binesti and J. P. Ducreux, "Core Losses and Efficiency of Electrical Motors Using New Magnetic Materials," *IEEE Transactions On Magnetics,* vol. 32, no. 5, 1996.
[99] S. J Chapman, *Electric machinery fundamentals*. McGraw-hill, 2004.
[100] Y. Huang, J. Dong, J. Zhu, and Y. Guo, "Core Loss Modeling for Permanent-Magnet Motor Based on Flux Variation Locus and Finite-Element Method," *IEEE Transactions on Magnetics,* vol. 48, no. 2, pp. 1023-1026, 2012.

[101] S. B. W. K. J. Tseng, "Analysis of flux distribution and core losses in interior permanent magnet motor," *IEEE Transactions on Energy Conversion,* vol. 14, no. 4, pp. 969-975, 1999.
[102] G. Burnand, D. M. Araujo, C. Koechli, and Y. Perriard, "Validation by measurements of a windage losses model for very-high-speed machines," presented at the 20th International Conference on Electrical Machines and Systems (ICEMS), Sydney, NSW, Australia, 2017.
[103] E. Roshandel, A. Mahmoudi, S. Kahourzade, A. Yazdani, and G. M. Shafiullah, "Losses in Efficiency Maps of Electric Vehicles: An Overview," *Energies,* vol. 14, no. 22, 2021.
[104] P. C. K. O. W. S. D. Sudhoff, *Analysis of Electric Machinery and Drive Systems*, Third ed. Wiley-IEEE Press, 2002, p. 632.
[105] D. Staton, Douglas Hawkins, and Mircea Popescu, "Motor-CAD software for thermal analysis of electrical motors–Links to electromagnetic and drive simulation models," presented at the CWIEME, Berlin 2010.
[106] D. Jie, "Thermal performance analysis of motor based on motor-CAD," 2019.
[107] C. Cossar, M. McGilp, S. Omori, "Analytical thermal models for small induction motors," presented at the 18th Int. Conf. on Electrical Machines, Vilamoura, 2008.
[108] C. Mejuto, Mueller, M., Staton, D., Mebarki, S., & Al-Khayat, N., "Thermal modelling of TEFC alternators," 2006.
[109] D. Staton, A. Boglietti, and A. Cavagnino, "Solving the More Difficult Aspects of Electric Motor Thermal Analysis in Small and Medium Size Industrial Induction Motors," *IEEE Transactions on Energy Conversion,* vol. 20, no. 3, pp. 620-628, 2005.
[110] W. H. McDermid, Manitoba "Insulation systems and monitoring for stator windings of large rotating machines," *IEEE Electrical Insulation Magazine,* vol. 9, no. 4, pp. 7-15, 1993.
[111] K. I. Laskaris and A. G. Kladas, "Permanent-Magnet Shape Optimization Effects on Synchronous Motor Performance," *IEEE Transactions on Industrial Electronics,* vol. 58, no. 9, pp. 3776-3783, 2011.
[112] Hioki. (2022). *Brochure: POWER ANALYZER PW3390*. Available: https://www.hioki.com/download/37473
[113] Hioki. (2022). *PW3390: User Manual*. Available: https://www.hioki.com/download/37465

Appendix

A. Material Specifications

Stator and rotor lamination material: M19_24G Steel

Parameter	Value
Bulk Conductivity (Siemens/m)	1960000
Core loss model coefficients	
kh	164.2
kc	1.3
ke	1.72
Mass Density (Kg/m^3)	7650

Magnet material: Arnold_Magnetics_N42SH (NdFeB-N42UH Magnet)

Parameter	Value
Bulk Conductivity (Siemens/m)	555555.55
Thermal Conductivity (W/m.C)	7.6
Mass Density (kg/m^3)	7500
Specific Heat (J/Kg.C)	460

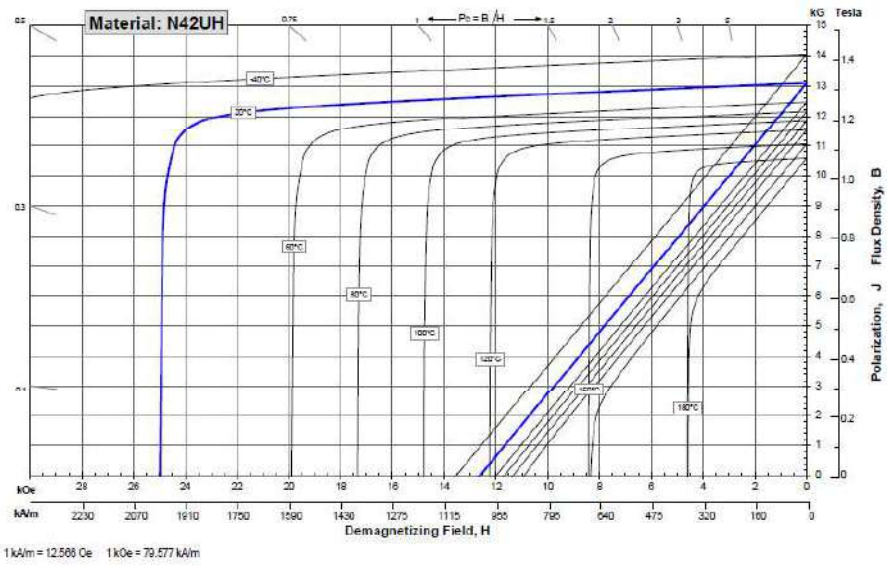

Fig A.1: B-H curve of NdFeB-N42UH Magnet

Shaft material: Stainless Steel

Parameter	Value
Bulk Conductivity (Siemens/m)	1100000
Thermal Conductivity (W/m.C)	13.8
Mass Density (kg/m^3)	8055
Specific Heat (J/Kg.C)	480

B. List of Publications

1. **Md Junaed Al Hossain**, Md Sariful Islam, Md Asaduzzaman, Md Akib Khan, Md Ziaur Rahman Khan "Design of a Permanent Magnet Brushless DC Motor for The Electric Three-Wheeler in Bangladesh"; Submitted in **IET Electrical Systems in Transportation**

2. **Md Junaed Al Hossain**, Md. Zakir Hasan, M. Hasanuzzaman, Md Ziaur Rahman Khan, and M. Ahsan Habib, "Affordable Electric Three-Wheeler in Bangladesh: Prospects, Challenges, and Sustainable Solutions," ***Sustainability,* vol. 15, no. 1, 2022.** (Q2, Impact Factor 3.9)

3. **Md Junaed Al Hossain**, Md. Zakir Hasan, and Md Ziaur Rahman Khan, "Analysis of Traction Power of Electric Three Wheelers in Bangladesh," *2022 12th International Conference on Electrical and Computer Engineering (ICECE)*, Dhaka, Bangladesh, 2022, pp. 352-355

C. Computer Codes

C.1. MATLAB Code for Analytical Motor Sizing

```
%% Reference Motor
D = 72;% Reference Motor bore diameter (or stator inside diameter)in mm
L = 48; % Reference Motor Stack Length in mm
g=1; % Air gap
Drotor=D-2*g; % Rotor Diameter
Volume_ref_rotor_m3 = pi*((Drotor/2)^2)*L*10^-9 % Reference Motor Volume in
m3
Volume_ref_rotor_mm3 = pi*((Drotor/2)^2)*L % Reference Motor Volume in mm3
ar = (L/Drotor); %Aspect ratio L/D
pout = 1000; %Designed Motor output power
rpm = 3000;  % Designed Motor RPM speed
radpsec=rpm*2*pi/60 % Designed Motor radian per second speed
rpmpsec = rpm/60 % Designed Motor revolution per second speed
tout=pout/radpsec% Designed Motor avg output power
Nm = 8; % No of poles
Ns = 12; % No of slots
Np=1; %No of parallel paths
Ncpph=Ns/3;
vdc = 48; %Supplied DC Voltage
d_eff = 0.9; % Desired Efficiency
inv_eff = 0.95; %Inverter Efiiciency
pin = pout / (inv_eff*d_eff) %Input Power
Iph_peak = pin/vdc; %Peak Current
Iph_rms = sqrt(2/3)*Iph_peak; %RMS Current
kw=0.866;
kf = 0.5; % Fill factor
ki = 0.9; %stacking factor or Iron insulation factor
Bg = 0.75;% Air gap magnetic flux density
Bst = 1.6;% Maximum flux density in stator tooth
```

```
Bsy = 1.4; % Maximum flux density in stator yoke
Bry = 1.15; %Maximum flux density in rotor yoke

TRV = tout/Volume_ref_rotor_m3 %Torque per volume in Nm/m^3
A=TRV*(sqrt(2)/pi)/(kw*Bg)
Ntph_ig=A*pi*Drotor*(10^-3)/(2*Iph_peak*2);
Ntc_ig= Ntph_ig/4
Ntc=ceil(Ntph_ig/4)
Ntph = 4*Ntc;
phi_t = Bg*pi*Drotor*L*(10^-6); %Total flux in Wb
phi_p = phi_t/Nm; %Flux under one pole
phi_st = phi_t/Ns; %Flux flowing in each tooth
Bg_fun = (8/pi^2)*Bg %the average value of the fundamental flux-density
phi_t_fun = Bg_fun*pi*Drotor*L*(10^-6);
phi_p_fun = Bg_fun*pi*Drotor*L*(10^-6)/Nm;
f=rpm*Nm/120;
E_phrms= 4.44*kw*phi_p_fun*f*Ntph
cphi = 0.94; % %stator tooth arc ratio, g_m=alpha_m/(2*pi/Nm),gm<1
alpha_s = 2*pi/Ns; %Stator slot pitch angle
alpha_p = 2*pi/Nm; %Rotor pole pitch angle
alpha_m = cphi*alpha_p;%Magnet arc angle
alpha_s_deg = alpha_s*180/pi; %Stator slot pitch angle
alpha_p_deg = alpha_p*180/pi; %Rotor pole pitch angle
alpha_m_deg = alpha_m*180/pi;%Magnet arc angle

Jsw = 5.0; %Stator current density A/mm^2
Ic = Iph_rms/Np; %Coil current
cAsc_ig = Ic/Jsw; %Copper Area of a single Coil
DcAsc_ig = 2*sqrt(cAsc_ig/pi()); % Diameter of a single Coil
Nstrand = 16;
cAss_ig = cAsc_ig/Nstrand;
%%Wire Choosing
```

```
X=csvread('wire.csv',2,0);
SWG_Area = X(:,7);
SWG_Diameter = X(:,6);
SWG_Number = X(:,5);
index=0;
n=1;
for i=1:length(SWG_Area)-1
   if cAss_ig<=SWG_Area(i) && cAss_ig>=SWG_Area(i+1)
      index=n;
      break;
   end
   n=n+1;
end
swg_no = SWG_Number(index);
Dswg_sc = SWG_Diameter(index); %Wire Diameter of a single strand
Aswg_sc = SWG_Area(index); %Wire Area of a single strand
cAsc_updated = Nstrand*Aswg_sc;
cAca = round(Ntc)*cAsc_updated;
Jsw_updated = Ic/cAsc_updated
gAca_updated = cAca/kf;
%%Geometry
bs0 = 2;%slot opening width in mm
hs0 = 1.5;%slot opening heigth in mm
hs1 = 0.75; %Height of tooth shoe
 g_wst =1; % Ratio of width of tooth upper tip and lower tip
wst1 = phi_st*1000/(Bst*ki*L*(10^-3)) %Width of stator tooth at tip
wst2 = g_wst*wst1;%Width of stator tooth at tail
bs1 = 2*((tan(pi/Ns))*((D/2)+hs0+hs1)-(wst1/2)/(cos(pi/Ns)));
wsy =(phi_p*1000/2)/(Bsy*ki*L*(10^-3))%width of stator yoke in mm
wry=(phi_p*1000/2)/(Bry*L*(10^-3)*ki)%width of rotor yoke in mm
a=2*tan(alpha_s/2);
b=bs1+(2*tan(alpha_s/2))*((D/2)+hs0+hs1)-(wst2/cos(alpha_s/2));
```

```
c=-4*gAca_updated;
delta = sqrt(b^2 - 4*c*a);
hs2 = (-b+delta)/(2*a);%Depth of the coil
bs2 = (4*gAca_updated/hs2)-bs1; %Width of Stator tooth
gamma_s = 2*asind((wst2/2)/(D/2 + hs0+hs1+hs2));%Angle created by the stator
teeth
 %% Magnet dimension
magnet_grade='Arnold_Magnetics_N42UH_80C';
kl =0.95017;%Leakage Factor
kr = 1.1369;%Reluctance factor
Hc = -934000;% cocitivity force for Arnold_Magnetics_N42UH_60C in A_m
Br = 1.25;% Remanence Flux density of magnets in Tesla
Hc = -925650% cocitivity force for Arnold_Magnetics_N42UH_60C in A_m
Br = 1.213;% Remanence Flux density of magnets in Tesla
mu_o =4*pi*10^-7; % air permeability
mu_M = -Br/Hc;%Permeability of magnet
mu_r = mu_M/(mu_o);%Relative Permeability of magnet
mmd = 7600; %Magnet Mass Density in Kg/(m^3)
pc = kr*mu_r /( (kl*cphi*Br/Bg)-1 );%flux concentration factor
dm = pc*g*cphi%Magnet thickness
dm1=dm;
%Resistance calculation
winding_material= 'Copper';
rho_sw_20C = 1.7241E-08; %Resistivity of stator winding 20C (for copper) in
ohm.m
alpha_t_sw = 4*10^-3; %Temperature coefficient for stator winding resistance
Tamb = 60;% ambient temperature in C
Tr = 60; % Temperature rise in C
rho_sw_tw = rho_sw_20C*(1+alpha_t_sw*(Tr+Tamb-20))%resistivity of stator
winding at working temperature
kar = 1.0;
Lend = 4.5;
```

```
Larc = ((D/2)+hs0+hs1+(hs2/2))*(2*pi/Ns);
lmt =2*L+4*Lend+2*Larc;
rc = kar* (Ntc*lmt*1000*rho_sw_tw)/cAsc_updated; %Coil Resistance in ohm
rph = rc*Ncpph*((1/Np)^2) %Phase resistance
Pcu = 3*rph*(Iph_rms)^2 %Total Copper Loss(Ideal Current)
OSD = D+2*(hs0+hs1+hs2+wsy);
Dsh = D-2*(g+wry+dm);
span = max(floor(Ns/Nm),1);
split_ratio = D/OSD
%Error Check
Jsw_calculated = Ic/cAsc_updated;
Jsw_error = (Jsw_calculated - Jsw)*100/Jsw;

Ncpph=4;
tcp=((D/2)+hs0+hs1+(hs2/2))*(2*pi/Ns);
As=2*gAca_updated;
Leb=(10^6)*(mu_o*tcp*(10^-3)*(Ntc^2)/4)*log(tcp*sqrt(pi)/sqrt(2*As))
Ldend = 2*Ncpph*Leb
```

C.2. Fast Fourier Transform of Time Domain Signal

```
X=csvread('shaftTorque.csv',1,0);
time=X(:,1);
torque=X(:,2);
 dt=2e-3;
fs=1/dt;
t_f=fft(torque);
m=length(t_f);
freq=(-m/2:(m/2 - 1))*(fs/(m-1))
plot(freq,fftshift(abs(t_f)*(1/m)),'k')
xlabel('Frequency', 'FontName', 'Times')
ylabel('Shaft Torque', 'FontName', 'Times')
set(gca,'fontsize', 14)
```

C.3. Efficiency Map

C. 3.1 Phase Current Waveform Processed

```
format long
speed=1000;
period=120*1000/(speed*8)
endtime=10+3*period

X=csvread('coilcurrent1000.csv',1,0);
time=X(:,1);
Ia=X(:,2);
Ib=X(:,3);
Ic=X(:,4);
Iaa=[time , Ia];
Ibb=[time , Ib];
Icc=[time , Ic];

plot(time,Ia)
hold on
plot(time,Ib)
hold on
plot(time,Ic)
hold on

writematrix(Iaa,'coil_a_1000.csv')
writematrix(Ibb,'coil_b_1000.csv')
writematrix(Icc,'coil_c_1000.csv')
```

C. 3.2 Parameter Value Determination with Interpolation

```
X=csvread('lkup3000.csv',1,0);
torque=X(:,4);
```

```
Pcu=X(:,7);
Pcore=X(:,9);
Psolid=X(:,10);
Pmec=X();
eff=X(:,13);
mec=X(:,11);
curr=X(:,5);
tq=0.2:0.1:10;
rpm=speed.*ones(length(tq),1);
for i=1:length(tq);
    Ir(i)= interp1(torque,curr,tq(i),'linear');
    pcu(i)=interp1(torque,Pcu,tq(i),'linear');
    pcr(i)=interp1(torque,Pcore,tq(i),'linear');
    pmech(i)=interp1(torque,mec,tq(i),'linear');
    sl(i)=interp1(torque,Psolid,tq(i),'linear');
    efi(i)=interp1(torque,eff,tq(i),'linear');
    pout(i)=speed*(pi/30)*tq(i);
    pin(i)= pout(i)+pcu(i)+sl(i)+pcr(i)+pmech(i);
    efff(i)=pout(i)/pin(i);

end
Y=[rpm tq' Ir' pcu' , pcr', sl', pmech' efi' pout' pin' efff'];
writematrix(Y,'mapnew3000new.csv')
%rpm   torque Ir copper core   solid  mech   effv1  pout     pin effv2
```

C. 3.3 Efficiency Map

```
clc
clear all
close all
X3=csvread('mapnew300.csv',1,0);
X6=csvread('mapnew600.csv',1,0);
X9=csvread('mapnew900.csv',1,0);
```

```
X12=csvread('mapnew1200.csv',1,0);
X15=csvread('mapnew1500.csv',1,0);
X18=csvread('mapnew1800.csv',1,0);
X21=csvread('mapnew2100.csv',1,0);
X24=csvread('mapnew2400.csv',1,0);
X27=csvread('mapnew2700.csv',1,0);
X30=csvread('mapnew3000new.csv',1,0);
X32=csvread('mapnew3200.csv',1,0);
X33=csvread('mapnew3300.csv',1,0);

Xall=[X3;X6;X9;X12;X15;X18;X21;X24;X27;X30;X32;X33];

EFF=Xall(:,8).*(0.9153/0.91557);
EffmapT=reshape(EFF,99,12);

rpmx=300:300:2700;
rpm=[rpmx,3000,3200,3300]
Torque=0.2:0.1:10;

figure(1)
[C1,h1] = contourf(rpm,Torque,EffmapT,70);
c = colorbar;
c.Label.String = 'Efficiency';
c.FontSize=14
clabel(C1,h1,'manual','color','k','FontSize',12);

Tqmap=csvread('peaktorque-map.csv',1,0);
Speed=Tqmap(:,1);
torque=Tqmap(:,2);

hold on
x=[Speed;rpm(end)];
```

```
y=[torque;Torque(end)];
patch(x,y,'white')

xlabel("Motor Speed (rpm)",'FontSize', 14)
ylabel("Motor Torque (Nm)",'FontSize', 14)
set(gca, 'FontName', 'Times New Roman')
 xlim([300,3300])
```